

**Multi-objective Algorithms for Coupled Optimization of Mechanical and  
Electromagnetic Systems**

Submitted in partial fulfillment of the requirements for

the degree of

Doctor of Philosophy

in

Electrical and Computer Engineering

Irina Brinster

B.S., Electrical Engineering, The University of Texas at Dallas

M.S., Electrical and Computer Engineering, Carnegie Mellon University

Carnegie Mellon University  
Pittsburgh, PA

December 2014



## Abstract

Modern mobile devices incorporate several transmit and receive antennas in highly constrained volumes. As miniaturized antennas impinge upon fundamental physical limits on efficiency, new design approaches are required to support ever-smaller devices with more varied and robust communication performance. We take an unconventional design approach in which an arbitrary metallic structure and its components can be modified to act as efficient radiators. Using eigenmode analysis and the theory of characteristic modes (TCM), we develop algorithms that allow for effective integration of antennas with mechanical structures and enable structure reuse, helping meet stringent space and weight constraints without sacrificing electromagnetic performance.

We derive TCM-based objectives for effective exploration of the design space in the electromagnetic (EM) domain. The procedure includes a feed placement technique that identifies viable excitation points on the structure without running full EM analysis. In addition to computational advantages, this provides a point of comparison among a variety of antenna shapes. Empirical evaluation shows that the estimates of radiated power from TCM can effectively guide optimization toward structures with improved radiating properties. Automated feed placement increases the proportion of good-quality designs among the explored candidates by consistently selecting the most promising feed positions. The ability of the TCM-based algorithm to direct the search is further validated on two real-world applications: integration of a GPS antenna with the frame of a mobile phone and integration of an S-band antenna with the frame of a small spacecraft. To the best of our knowledge, this is the first work that applies TCM to automated optimization of antennas.

We investigate how to leverage domain-specific methods and solution representations in the coupled optimization of antennas. We develop a novel multi-objective optimization framework based on local search in each domain. In this procedure, the local optima in each objective are obtained and modified to create a new population of candidate designs. On a number of benchmark problems, the proposed technique is competitive with leading multi-objective algorithms: while it finds a less uniform distribution along the Pareto front, it shows better performance in locating solutions at the boundaries of the tradeoff curve. The local search algorithm is successfully applied to topology optimization of an antenna for a CubeSat, a small low-cost satellite platform.



## Acknowledgments

This research was supported by NASA Space Technology Research Fellowship NNX11AN23H. The research funds for the work on TCM were partly provided by Google's Advanced Technology Projects (ATAP) group as part of Project Ara.

Thesis committee:

Professor Jason Lohn, Committee Chair, ECE, CMU

Professor Ole Mengshoel, ECE, CMU

Professor Patrick Tague, ECE, CMU

Dr. Julie Bellerose, Outer Planet Navigation Group, JPL

I would like to thank my parents, whose material and emotional contribution to project "Irina" cannot be overestimated. Over the years they invested their nerves, time, and money in my education. By their own example, they instilled in me the interest in engineering and sciences and the ambition to aim high. My husband is yet another big contributor: he supported me in so many different ways, I can hardly hope to ever match it. His levelheadedness and clear view of things helped me set my priorities and keep focused on my goals. His professional advice and encouragement were huge factors in my getting to this point in the PhD career.

Professionally, I have benefited greatly from taking classes with Dr. Ianucci, Dr. Mengshoel, Dr. Zhang, and Dr. Lohn. I would also like to acknowledge the students, William Chan, Aniruddha Basak, Abhinav Jauhri, Priya Sundararajan, and Philippe De Wagter, with whom I worked on a number of class projects and whose knowledge, creativity and fun personalities were a source of inspiration and motivation. I greatly appreciate collaboration with Shakib Ghassemieh and Chad Frost, my mentors at NASA Ames Research Center, who helped me understand space mission requirements and tradeoffs. I thank Dr. Derek Linden for teaching me the techniques of antenna and circuit measurements and advising me on the theory of characteristics modes. It was a great learning experience and a pleasure to work with Dr. Ole Mengshoel on stochastic algorithms and Bayesian networks. My progress in the PhD program often depended on Dr. Mengshoel and Dr. Tague, who served on the committees in my qualification exam, proposal and defense, and I thank them for their valuable suggestions on extending my research and their confidence in my abilities. I would like to express my sincere gratitude to Dr. Julie Bellerose for her active involvement in my proposal and defense. Being a great mentor, she taught me a lot about space environments and mission design.

I would like to thank my advisor Dr. Jason Lohn for giving me the opportunity to be part of CMU and meet all these people. I would like to thank him for introducing me to the field of antenna design and optimization in which I wish to continue after graduation. I am grateful for my advisor's guidance in

the key moments of my PhD, his professional support, and his prompt actions in response to my requests for additional resources. But above all, I appreciate the freedom that Dr. Lohn gave me in determining the focus of my research and the opportunity to work at my own pace.

I was lucky to be surrounded by the most supportive and knowledgeable people who helped me grow professionally and personally and who helped me succeed in my PhD. The difference they made is reflected in this work and is also marked in my heart.

# Contents

<b>Abstract</b>	<b>iii</b>
<b>Acknowledgments</b>	<b>v</b>
<b>List of Figures</b>	<b>ix</b>
<b>List of Tables</b>	<b>xi</b>
<b>List of Abbreviations</b>	<b>xiii</b>
<b>1 Introduction</b>	<b>1</b>
1.1 Contributions . . . . .	2
1.2 Motivation . . . . .	3
1.2.1 Coupled Design of Antennas . . . . .	3
1.2.2 Mechanical Optimization . . . . .	8
1.2.3 Antenna Optimization . . . . .	10
1.2.4 Multi-physics CAD optimization . . . . .	11
1.3 Summary . . . . .	13
<b>2 Related Research</b>	<b>14</b>
2.1 Background: Theory of Characteristic Modes . . . . .	14
2.2 Evolutionary Algorithms . . . . .	18
2.3 Multi-objective Optimization Algorithms . . . . .	21
2.3.1 Classical Approach to Multi-objective Optimization . . . . .	22
2.3.2 Evolutionary Approach to Multi-objective Optimization . . . . .	24
2.3.3 Multio-bjective Optimization with Local Search . . . . .	26
2.3.4 Challenges for MOEAs . . . . .	27
2.3.5 Performance Metrics . . . . .	28
2.4 Summary . . . . .	30
<b>3 Automated Antenna Design using the Theory of Characteristics Modes</b>	<b>31</b>
3.1 Introduction . . . . .	31
3.2 Power Analysis Based on TCM . . . . .	32
3.2.1 Relation between the Radiated Power and Matching . . . . .	37
3.2.2 Feed Placement for Dipole, Yagi-Uda, Wire Loop and PIFA Antennas	39

3.2.3	Feed Placement for an Arbitrary Wire Structure . . . . .	42
3.3	Using TCM in an Optimization Procedure . . . . .	44
3.3.1	Computational Challenges . . . . .	45
3.3.2	Validation of the Algorithm on Small Test Problems . . . . .	46
3.3.3	Generation of New Designs . . . . .	57
3.3.4	Computational Time . . . . .	58
3.3.5	Optimization of the Endoskeleton . . . . .	60
3.3.6	Feed Placement and Optimization of the Cubic Structure . . . . .	63
3.4	Summary . . . . .	65
<b>4</b>	<b>Multi-objective Algorithms for Coupled Optimization</b>	<b>66</b>
4.1	Coupled Electromagnetic and Mechanical Optimization . . . . .	66
4.2	Benchmark Problems and Their Solutions . . . . .	68
4.2.1	Load-bearing Dipole Antenna . . . . .	68
4.2.2	Benchmark B1: Cantilever Beam Optimization . . . . .	71
4.2.3	Benchmark B2: Geometry Optimization of a Two-bar Truss . . . . .	73
4.2.4	Benchmark B3: Sizing Optimization of a Two-bar Truss . . . . .	76
4.2.5	Benchmark B4: Topology Optimization of a Ten-bar Truss . . . . .	79
4.3	Multi-objective Optimization with Local Search . . . . .	83
4.3.1	Implementation of MOLS . . . . .	87
4.4	Comparison of the Algorithms on Benchmark Problems . . . . .	89
4.4.1	Experimental Set-up . . . . .	89
4.4.2	Experimental Results . . . . .	91
4.5	Summary . . . . .	108
<b>5</b>	<b>Multi-objective Optimization of a CubeSat</b>	<b>110</b>
5.1	Problem Definition . . . . .	111
5.2	Implementation . . . . .	115
5.3	Results . . . . .	118
5.4	Summary . . . . .	122
<b>6</b>	<b>Conclusions and Future Work</b>	<b>124</b>
6.1	Multi-objective optimization with Local Search . . . . .	124
6.2	Local search in the EM domain . . . . .	127
6.3	TCM . . . . .	128
6.4	Conclusion . . . . .	130
	<b>Bibliography</b>	<b>131</b>

# List of Figures

2.1	Flowchart of an evolutionary algorithm for antenna optimization. . . . .	20
3.1	VSWR as a function of radiated power. . . . .	38
3.2	Power contribution calculated from TCM for different antenna types. . . .	41
3.3	Feed placement for an arbitrary wire structure. . . . .	43
3.4	Unmodified structures used for testing the TCM objectives. . . . .	50
3.5	TP1: Correlation and its significance for the observations in the order of increasing reactance. . . . .	54
3.6	TP1: Correlation for the observations in the order of increasing ratio of imaginary and real parts of the impedance. . . . .	55
3.7	TP2: Correlation between the inverse of the real power and VSWR. . . . .	56
3.8	Execution time of full EM and TCM-based procedures. . . . .	59
3.9	Grid model and characteristic modes of the endoskeleton. . . . .	61
3.10	Optimized endoskeleton 1: Geometry and Electromagnetic performance. . .	63
3.11	Optimized endoskeleton 2: Geometry and Electromagnetic performance. . .	64
3.12	Cube structure modified to radiate at 2.45 GHz. . . . .	65
4.1	Monopole antenna under load. . . . .	69
4.2	Change in the monopole's performance due to the uniform loading. . . . .	70
4.3	B1: Illustration of the Pareto-optimal solutions for the cantilever beam problem. . . . .	72
4.4	B2: Problem definition in the mechanical and EM domains. . . . .	74
4.5	B2: The search space and the Pareto optimal designs for the various truss topologies. . . . .	75
4.6	B3: Problem definition in the mechanical and EM domains. . . . .	77
4.7	B3: Pareto solutions for the two-bar truss. . . . .	78
4.8	B4: Problem definition in the mechanical and EM domains. . . . .	80
4.9	B4: Pareto solutions for the ten-bar truss problem. . . . .	82
4.10	Local search step in MOLS algorithm as used in B4. . . . .	88
4.11	Performance on B1: Distribution of solutions along the Pareto front found by each algorithm and the global Pareto-optimal front. . . . .	94
4.12	Performance on B2: distribution of solutions in the design space. . . . .	97
4.13	Performance on B2: Pareto front for the highest performing runs. . . . .	98
4.14	Performance on B2: Pareto front for the lower performing runs. . . . .	99
4.15	Performance on B3: Pareto front for the runs with the best set coverage. .	102

4.16	Performance on B3: Pareto front for the runs with the worst set coverage. .	103
4.17	Performance on B4: Pareto surface for the runs with the lowest spread. . .	104
4.18	Performance on B4: Pareto surface for the runs with the worst spread. . .	104
4.19	Performance on B4: Pareto-optimal topologies found by the algorithms. . .	106
4.20	Comparison of algorithms' performance on the benchmarks $B1-B4$ : pairwise set coverage. . . . .	107
4.21	Comparison of algorithms' performance on the benchmarks $B1-B4$ : metrics statistics. . . . .	109
5.1	CubeSat examples. . . . .	111
5.2	FEM representation of a CubeSat in the mechanical and EM domains. . .	116
5.3	CubeSat Problem: Non-dominated solutions found by MOLS. . . . .	119
5.4	Radiation patterns of CubeSat antennas found by MOLS. . . . .	121

# List of Tables

3.1	Standard antenna shapes used to verify TCM-based algorithm for feed placement. . . . .	39
3.2	Spearman rank coefficients for the six test problems. . . . .	52
56table.caption.16		
4.1	Characteristics for four benchmarks B1 - B4. . . . .	68
4.2	Multi-objective algorithms' and random search parameters. . . . .	91
4.3	B1: summary of performance metrics. . . . .	93
4.4	B2: percentage of runs in which the disjoint Pareto-optimal regions were found. . . . .	95
4.5	B2: Summary of performance metrics for the runs with the best and worst set coverage. . . . .	96
4.6	B3: summary of performance metrics for the runs with the best and worst set coverage. . . . .	100
4.7	B4: summary of performance metrics for the runs with the best and worst spread. . . . .	105
5.1	CubeSat structures representative of the search space in the mechanical domain. . . . .	117
5.2	Performance scores of the CubeSat antennas found by MOLS. . . . .	122



# List of Abbreviations

**B** Benchmark.

**CAD** Computer - Aided Design.

**CLAS** Conformal Load-bearing Antenna Structures.

**EA** Evolutionary Algorithm.

**EM** Electromagnetic.

**EMO** Evolutionary Multi-objective Optimization.

**FE** Finite Element.

**FEM** Finite Element Method.

**GA** Genetic Algorithm.

**GD** Generational Distance.

**GHS** Greedy Hill Climber.

**IC** Integrated Circuit.

**MIMO** Multiple Input Multiple Output.

**MOA** Multi-objective Optimization Algorithm.

**MOLS** Multi-objective Optimization with Local Search.

**MoM** Method of Moments.

**MOO** Multi-objective Optimization.

**MOP** Multi-objective Optimization Problem.

**NEC** Numerical Electromagnetics Code.

**NSGA** Non-dominated Sorting Genetic Algorithm.

**NVIS** Near Vertical Incidence Skywave.

**PF** Pareto Front.

**PIFA** Printed Inverted F Antenna.

**PS** Pareto Set.

**RG** Realized Gain.

**RHS** Randomized Hill Climber.

**SIMP** Solid Isotropic Material with Penalization.

**SMA** Shape Memory Alloys.

**SOP** Single-objective Optimization Problem.

**SPEA** Strength Pareto Evolutionary Algorithm.

**SQP** Sequential Quadratic Programming.

**SSA** Stochastic Search Algorithm.

**TCM** Theory of Characteristic Modes.

**TP** Test Problem.

**UAV** Unmanned Aerial Vehicle.

**UHF** Ultra High Frequency.

**VHF** Very High Frequency.

**VSWR** Voltage Standing Wave Ratio.

# Chapter 1

## Introduction

The advent of computer-aided design (CAD) has allowed engineers to replace physical testing of systems with computer simulations. This has enabled them to quickly explore and compare a multitude of design choices before settling on a technically and economically viable solution. Modern technology enables highly complex designs in which interaction between multiple components cannot always be thoroughly understood or anticipated. In such cases, trade space exploration and search for an optimal solution requires taking into consideration constraints across multiple physical domains (e.g., mechanical, electronic, thermal, optical, etc.), making conventional trial-error methods infeasible. This highlights the need for a flexible automated optimization tool that can explore vast multidimensional search spaces efficiently and come up with complex real-world designs. Such an optimization tool should be able to take into account multiple objectives (such as size, weight, power consumption, and RF emissions) across multiple components and provide a range of feasible engineering solutions, reducing the costs of system engineering. Moreover, such a tool should effectively assist engineers in trade-space exploration by providing sensitivity information and identifying marginal designs in each of the domains.

## 1.1 Contributions

This work extends the current state-of-the-art simulation tools, most of which can take into account only a single phenomenon during optimization. It investigates new stochastic optimization algorithms to be used in a multi-physics design automation tool and is the first to develop efficient techniques for coupled optimization of integrated electromagnetic and mechanical systems. The main contributions of this thesis are: 1) A new TCM-based algorithm for optimization of metallic structures in the EM domain; 2) A new algorithm for coaxial feed placement; 3) Definition of benchmark problems for coupled EM and mechanical optimization; 4) New multi-objective algorithm with local search (MOLS) for coupled optimization; and 5) Comprehensive evaluation of the algorithmic performance on benchmark problems.

Optimization in the EM domain is guided by eigenmode analysis of the structure. The theory of characteristic modes (TCM) is used for computing electromagnetic resonant frequencies at which the structure can radiate efficiently and calculating the feed configuration for exciting the resonant modes. To the best of our knowledge, this is the first work that applies TCM to automated optimization of antennas. We derive TCM-based objectives and neighborhood relations for effective exploration of the design space. We develop a feed placement technique that allows us to identify good excitation points on the structure without running full EM analysis. In addition to computational advantages, this provides a fair point of comparison of the various antenna shapes. We conduct thorough empirical evaluation of the proposed algorithm and show that it performs effective search on a number of test problems.

We characterize the interactions in the mechanical and EM domains and illustrate the challenges of two-disciplinary optimization using small benchmark problems: design of a two-bar truss antenna, design of a uniformly loaded cantilever beam or a monopole, and design of a ten-bar truss antenna. We plot the Pareto trade-offs and evaluate the perfor-

mance of existing multi-objective evolutionary algorithms. We define multi-objective fitness functions and determine candidate solution representations suitable for both domains. Because mechanical evaluations are fast compared to the EM analysis, we investigate how the multi-objective optimizer can utilize the fitness information from a single domain in its search for Pareto-optimal solutions.

Finally, we validate the algorithms on a large-scale real-world application: integration of an antenna with the frame of a small spacecraft. For topology optimization of the CubeSat antenna, the TCM-based algorithm is combined with the gradient-based Solid Isotropic Material with Penalization (SIMP) method for 3D structures.

The thesis is structured as follows: in Chapter 1 we motivate the study of the coupled optimization of antennas and introduce the fields of mechanical and EM optimization. Chapter 2 reviews the literature on TCM and multi-objective algorithms, and also covers the essential background material to build on in Chapters 3 and 4. The TCM-based algorithm for automated antenna design is presented in Chapter 3, while Chapter 4 looks at coupled optimization across mechanical and EM domains. In Chapter 5, the proposed multi-objective algorithm to optimization of a CubeSat antenna. Chapter 6 concludes with the summary of results and an outlook to future extensions of this research.

## **1.2 Motivation**

### **1.2.1 Coupled Design of Antennas**

The focus on antenna optimization across mechanical and EM domains is driven by aerospace and mobile applications. On one hand, coupled design and optimization is necessary to ensure that antenna’s performance is not sensitive to deformations experienced under load. For example, antennas mounted on the aircraft are subjected to significant loads during flight. Embedding antennas into the aircraft skin improves its aerodynamical properties

and reduces the size and weight of the system. Reflector antennas are large mechanical structures that should be designed to bear self-weight, winds, temperature gradients, ice and snow. On the other hand, modern mobile device incorporates several transmit and receive antennas in highly constrained volumes. As minituarized antennas impinge upon fundamental physical limits on efficiency, integrating an antenna with the metallic phone chassis could enhance its EM performance and help meet the tight space and weight constraints.

Interactions of the antennas' mechanical and EM properties has been the subject of interest in various application domains.

*Reflector antennas.* Large satellite dishes and reflector antennas are massive structures that must be able to withstand significant loads, like self-weight, winds, thermal gradients, etc. Mechanical deformation of the reflector surface affects its gain and causes aberrations in the antenna pattern. Mechanical and EM properties of large reflector antennas (parabolic dishes) are well studied. The reflector performance is characterized in terms of how well the surface of the reflector matches that of a paraboloid: Ruze's approximation formula characterizes the dependence between the antenna's efficiency and the RMS error in the distance between the focus of the ideal parabolic and the deformed reflector surface [67]. Liu and Hollaway present a systematic method and implementation details for Pareto optimization of a reflector antenna with the truss backup structure [46]. They incorporate structural (mass, structural fundamental frequency, maximum stress and displacement) and EM objectives (EM efficiency, mainlobe and sidelobe levels) for many loading cases. The optimization variables include member sizes, structural geometric and material design variables. They conclude that there is a benefit in including EM performance calculations into the procedure for optimization of large antenna structures [46].

Wang and Duan discuss the electromechanical coupling for a variety of antenna applications [24], [79]. They list the coupling variables and equations for the reflector antenna,

planar slotted antenna, active phased array, and high-density packaging system. They compare the simulation and measurement to verify the proposed models for describing the interaction between the deformation, temperature and EM performance. They conclude that the deformation and thermal fields can distort electrical performance of the antenna, resulting in smaller gain, higher sidelobe level, and broader width of the main beam. The impact becomes more detrimental at higher frequencies so that a more in-depth study is needed to characterize inter-domain coupling [24].

*Mechanically reconfigurable antennas.* Large reflector antennas can be replaced with a mesh of metallic elements that approximate the curvature of the parabolic surface. The density of the mesh is chosen as a trade-off between the mass of the antenna and its EM performance. While denser meshes have higher mass, they can provide better radiation efficiency at higher frequencies, as they better approximate the parabolic surface. Mechanically reconfigurable antennas have been designed to compensate for the deflections of the main reflector surface under load. The reconfigurable mesh antenna was introduced in 1988 by Clarricoats and Zhou [17], and the ability to synthesize arbitrary radiation patterns by controlling the position of the nodes in the mesh was demonstrated in subsequent years [56]. Mesh antennas have been successfully deployed in space: replacing full metallic dish with a mesh allows for compact stowage during antenna’s transport into orbit; coupled with mass reduction this can significantly reduce the deployment costs.

Smart materials such as shape memory alloys (SMAs) have been used to mechanically reconfigure antennas and achieve the desired change in the radiation pattern. The radiating helix antenna is connected in parallel with the spring made of SMA. When the DC current is passed through the SMA spring, it contracts, forcing the helix antenna to contract as well [35]. The same research group developed a pattern reconfigurable monopole antenna: a parasitic element constructed of a deformable polymer-metallic composite was placed close to a monopole antenna. By varying the DC voltage, the added strip could be deflected to

different angles, changing the radiation pattern of the monopole [51].

*Conformal load-bearing antenna structures.* Conformal load-bearing antenna structures (CLAS) have been studied as a low-cost replacement for conventional antennas mounted on the aircraft surface, e.g., blades, wires and dishes. Conforming the antenna to the fuselage or embedding it into the aircraft skin decreases the drag, weight, and signature of the aircraft and might enhance the aircraft's damage resistance and structural efficiency [11]. The CLAS must be optimized for EM and mechanical performance. Recently, multiple companies have successfully demonstrated CLAS technology: American Semiconductor in cooperation with the Air Force Research Laboratory has developed conformal antenna and interconnects printed on a flexible substrate for an UAV. Mechanical testing, however, demonstrated poor mounting of the packaged ICs on the flexible substrates. The company now plans to optimize the antenna design and the substrate for conformally mounted applications [14]. Boeing and ManTech demonstrated the CLAS by replacing a VHF blade antenna on a 737 wing-to-body fairing with a conformal design [9].

In the academic community, optimization of structurally and electrically efficient antennas was researched [81]. The group applies design of experiments and response surface modeling to optimize a stacked patch antenna. The antenna is integrated in a sandwich structure whose topology is representative of the composite skin of an aircraft. The responses for the surface models are the gain of the antenna and the mechanical deflection at the patch center [81].

The idea of a structural antenna has also been applied on a different scale - for VHF/UHF communications in marine and aerospace applications. As an example, Chen et al. convert a ship's structure into an antenna for the near vertical incidence skywave (NVIS) communication [16]. They introduce large feed slots and validate the design by building a scaled model of the ship-antenna. For this design, no mechanical analysis of the structure is performed to ensure structural integrity of the resulting ship.

*Mobile antennas.* In the era of mobile handheld devices, the push for more diverse and robust wireless communication components squeezed into a tighter volume motivates the need for new approach to antenna design. As the performance of electrically small antennas (i.e., antennas whose largest dimension is smaller than  $1/20$  of the wavelength of operation) reaches physical limitations, reuse of the phone structure could help meet the stringent weight and size constraints and the LTE advanced standards for high-speed data transfer. Miniaturization of antennas will also play a vital part in shaping the Internet of Things (IoT), in which myriads of sensor nodes will be connected with wireless links to provide services ubiquitously and unobtrusively to the user. Integrating the nodes' antennas with the existing structures will be beneficial for both functional and aesthetic reasons.

A number of research groups have looked into utilizing phone chassis as a radiating structure. The antenna is viewed as a coupling element that can excite mode currents on the frame of the phone, which are obtained from the theory of characteristic modes (TCM). A detailed review of the theory and related research is given in chapter 2 of this thesis; in chapter 3 we describe a TCM-based algorithm for automated antenna optimization.

*Wearable antennas.* The design of wearable and flexible antennas requires minimization of weight and size as well as maximization of durability of the antenna. Wearable antennas are primarily designed for military applications and extreme and climatically challenging environments; depending on the application, they must be resistant to mechanical shock, temperature, and material fatigue [64], [53], [68].

*Sensing applications.* There is a variety of sensing applications in which mechanical properties of the antennas are used to monitor the mechanical integrity of a structure. For example, the sensitivity of antenna's EM performance to mechanical stress has been utilized to monitor the structural strain in bridges and rails. A patch antenna is attached to the rail. If the crack develops along the structure, antenna experiences deformation which causes a shift in its resonance frequency. This change results in the degradation of

the signal transmitted by the antenna which can be detected wirelessly by an RFID reader [42].

The above applications highlight the necessity to study and provide systematic approach to coupled optimization of antennas across mechanical and EM domains. In many areas, understanding the trade-offs between EM performance and mechanical properties is required to prevent communication failure. In other areas, the structural properties of the antenna can be exploited to achieve diversity and enhance communication performance.

### 1.2.2 Mechanical Optimization

The proposed research is closely related to the field of structural optimization. Robust methods for structural optimization have been developed over the past 100 years. The topological and geometric optimization of truss structures is well established and provides mathematical programming techniques for structural problems with large number of design and state variables and non-linear constraints. With the cheap computational power and accurate mechanical modeling tools, the application of currently available global search techniques has become possible for real-world structural designs.

**Sizing, Shape and Topology Optimization.** Structural optimization is divided into three main categories - sizing, shape, and topology optimization. *Sizing optimization* is concerned with finding the optimal values of design parameters for a structure with predefined shape and geometry. For example, in a truss optimization problem, the nodes and connectivity between the nodes might be fixed, while the cross sectional areas are modified to maximize the stiffness of the structure. In *shape optimization*, the boundary of the structure is optimized, while the topology is fixed. Thus, in optimization of a truss shape, design variables might include the nodes' coordinates and node-member incidence.

*Topology optimization* seeks to find the optimal distribution of material in the reference domain for known load and support conditions and a desired volume. This type of opti-

mization has been a central research topic in the structural optimization community over the past three decades, giving rise to a number of robust solution techniques for a variety of structural design problems and constraints. Bendsoe was the first to formulate structural design as a material redistribution problem [5]. In the simple formulation, the structure is optimized for minimum compliance (equivalently maximal stiffness) under volume constraints. Every point is viewed as a material point or a void [6]; the optimization goal is then to determine the optimal assignment of material/void to the points within the domain so that the potential energy of the loaded structure is maximized and the equilibrium constraints are satisfied. Bendsoe removed the discrete nature of the problem by expressing the objectives and constraints in terms of a continuous design variable, which can be interpreted as a density of material in a given point [5]. The intermediate density points were penalized to steer the optimization procedure toward 0-1 designs. In this continuous form, the problem could be solved efficiently by mathematical programming.

There exist alternative approaches to topological optimization that do not use mathematical programming. Most of them are based on growing or degenerating the initial structure or introducing holes to achieve the desired structural response. Evolutionary structural optimization (ESO) uses a very intuitive approach: starting with a dense finite element mesh of the structure, it removes regions of material with the lowest stress. After each small change, the structure is re-analyzed, and the procedure is repeated until a fully stressed design is obtained [80]. A so-called Bubble Method iterates between hole positioning (called a bubble) and structural shape optimization of the new design. The hole is inserted based on some positioning criterion that depends on the objective function and constraints as well as the type of load [26].

Genetic algorithms have successfully been applied to small- scale structural problems. However, they have not gained much popularity in real-world designs because of the slow convergence and large number of fitness evaluations that involve computationally costly

finite element analysis. Various types of new operators and representations of mechanical structures have been investigated to alleviate this problem - yet, they are still far from reaching the performance of classical optimization techniques, that remain standard in industrial applications.

### 1.2.3 Antenna Optimization

Antenna optimization relies on methods similar to the ones developed in mechanical optimization: sizing, shape and topology optimization have been applied to various antenna problems.

Antenna engineers commonly use a parametric approach - similar to mechanical sizing - to antenna optimization. The designer chooses the shape of the antenna based on the a-priori knowledge of its radiating properties and frequency range, parametrizes and optimizes its geometric dimensions. Examples include optimization of the width and length of a microstrip patch, the extent of the slots in the ground plane of a printed inverted F antenna (PIFA), or size of corrugations in the horn antenna.

The non-parametric approach is widespread for the optimization of planar antennas. Antenna's surface is discretized into small elements (much smaller than the wavelength) and represented as a 0/1 design - with ones denoting metallic areas and zeros assigned to the areas without metal. Removal and addition of metal is the primary mechanism for creating new designs. The design variables are binary, and the dimension of the optimization problem is equal to the number of the mesh elements. This problem formulation lends itself well to integration with the numerical solutions of Maxwell's equations such as the Method of Moments [38] or approximations using the transmission line theory [27]. In these methods, current distribution on the structure is calculated by solving a matrix equation of the form  $[I] = [Z]^{-1}[V]$ , where  $I$  is an  $n \times 1$  vector of current values on each element ( $n$  is the total number of mesh elements),  $Z$  is an  $n \times n$  interaction/impedance matrix and

$V$  is the voltage excitation vector. Mathematically, removing a "mesh" element from the structure requires removing the corresponding row and column of the impedance matrix and corresponding rows in the current and voltage vectors.

Shape optimization through parametrization of the surface using Bezier functions has been demonstrated for reflector antennas [77]. A similar approach was applied to ultra-wideband antenna synthesis [48], in which the shape of the patch antenna was parametrized using B-spline representation, and the contours of the patch were defined using a set of control points, whose positions were optimized.

Stochastic search algorithms prevail in EM optimization as they can effectively handle complex, discontinuous, non-differentiable and discrete landscapes. In electromagnetics, the search landscapes are vast and difficult to characterize analytically; sensitivity information is not available or expensive to obtain. Therefore, unlike mechanical optimization, stochastic methods are preferred over the deterministic gradient-based techniques. Because of the inherent complexity and non-linearity of EM landscapes, the research in the field of antenna optimization has focused on defining suitable algorithm parameters and representations rather than rigorous mathematical formulations of the optimization problems.

#### 1.2.4 Multi-physics CAD optimization

Multiple commercial packages include the capability to perform coupled optimization across several physical domains. However, due to the complexity of the models and intensity of computation, rarely more than two domains are considered at a time.

In general-purpose tools, the coupling between domains can be expressed in a variety of ways: in COMSOL, for example, the coupling can be defined explicitly through solving the system of PDEs. The interface to MATLAB allows users to define the optimization loop, objectives and constraints, exchanging the design and control variables between the models. The general optimization procedure can be also defined through the COMSOL's

optimization package that can use outputs from any domain simulation to define the objective function and update the designs. For some multiphysics problems, modules are developed for easy modeling of the domain interactions. Thus, a MEMS module integrates "solid mechanics with electrostatics and moving mesh to model the deformation of electrostatically actuated structures" [19]. In case of EM and structural coupling, the ALE or computational fluid modules can be used to define how the structural changes affect EM performance. The deformations of the shape appear as changes in the mesh of the structure which is then used for simulation in the EM domain.

Similarly, ANSYS provides two techniques for setting up multi-physics problems: for a variety of coupled-field problems - such as inductive heating, electrostatic actuation, Joule heating, electroelasticity, piezoresistivity, etc. - the coupled-physics can be modeled and solved for directly using only one FEM model. For many coupled problems (e.g. thermal-electric, thermalelectricstructural, EMstructural, etc.) sequential modeling can be applied: a model must be defined for each individual discipline; each discipline is then solved sequentially, and convergence is obtained between the disciplines at each iteration during the solution [2]. ANSYS also includes design exploration tools which allow for direct or response optimization across single or multiple domains, support design of experiments, sensitivity and six-sigmas analysis.

Set up of multiphysics simulation requires expertise and proficiency in all involved domains. A good overview of the state of the multiphysics software, challenges and approaches in multi-physics simulation can be found in [40]. The author underlines that the main opportunity in multiphysics simulation is still in "leveraging known concepts in new contexts" rather than scaling up the performance of the coupled simulation.

The algorithms in this work target antenna optimization and integration of the antennas with the existing structures. These algorithms could be used in a CAD tool as a separate module, enabling the users to evaluate the structure's radiation properties and modify

it to act as an efficient radiator. We apply the domain-specific optimization techniques to allow for fast assessment of each structure and predict the promising feed positions. The accomplished research does not attempt to compete with the general-purpose CAD and optimization tools, but rather extends existing multi-physics methods to the coupled optimization of antennas.

In this work, we use the domain-specific techniques/simulators to obtain most accurate and efficient evaluation of the objective function. For some problems, analytical functions exist to describe structural properties of the antennas, e.g. simple FEM models of trusses and beams are solved using the structural code implemented in MATLAB. Method of Moment (MoM) codes - NEC2C or WIPL-D- are applied to simulate antenna's EM performance.

### 1.3 Summary

Interactions between an antenna's mechanical and EM properties has been the subject of interest in various application domains. We desire to engineer antennas that can bear heavy loads while providing robust communication performance. On the other hand, we want to reuse existing structures or structural components to enhance an antenna's radiation. In this research work, we develop a systematic approach to optimization of antennas across mechanical and EM domains. We develop a theoretical foundation for optimization of structural antennas. Building on the TCM, we improve the search in the EM domain for easier integration with the structural optimization methods (Chapter 3). The fields of EM and structural optimization are very mature but have developed along different paths. We consider optimization of several basic coupled EM and mechanical systems as multi-objective problems and investigate solution techniques that can effectively leverage domain-specific methods and solution representations (Chapter 4). Finally, we test the performance of proposed algorithms on a real-world optimization problem (Chapter 5).

# Chapter 2

## Related Research

The contributions of this thesis relate to the fields of electromagnetics and multi-objective optimization (MOO). In the electromagnetic (EM) domain, we define new fitness functions based on the theory of characteristics modes (TCM). Section 2.1 introduces the TCM for conductive bodies and reviews the existing research on its application to antenna design. In chapter 3, the TCM is extended to automated feed placement. Chapter 4 builds on the material presented in Sections 2.2 and 2.3. Section 2.2 describes the typical flow of an evolutionary algorithm in antenna optimization. Section 2.3 introduces the concept of Pareto optimality and reviews the classical and evolutionary approaches to MOO as well as the techniques for their hybridization. The section also defines the metrics for evaluating algorithms' performance on multi-objective benchmark problems.

### 2.1 Background: Theory of Characteristic Modes

TCM is based on the method of moment (MoM) formulation, which is a classical method to simulate antenna structures. The input to the simulation is antenna's geometry as well as position and magnitude of the power source that determines how energy is coupled into the antenna. In MoM, an antenna is subdivided into multiple elements, segments or patches.

The main task of the simulation is to determine the currents on each of the segments produced by the excitation, from which any other metric of the antenna performance, like impedance at the feed, electric fields, radiation pattern, etc. can be calculated. The relation between the unknown total current  $J_{total}$  on the antenna subdivided into  $n$  segments and the known excitation vector  $E$  is expressed in matrix form [8]:

$$[Z]_{n \times n} [J_{total}]_{n \times 1} = [E]_{n \times 1}$$

$$J_{total} = Z^{-1} E$$

$J_{total}$  and  $E$  are  $n \times 1$  column vectors;  $Z$  is an  $n \times n$  interaction or impedance matrix that expresses the mutual EM interactions between any two segments in the structure.  $Z$  consists of complex entries and can be decomposed into real and imaginary parts as  $Z = R + jX$ . MoM procedure includes two major computational steps: assembly of the impedance matrix  $Z$  and second, inversion of this matrix and its multiplication with the excitation vector  $E$ .

A theory of characteristic modes describes the behavior of a scattering or radiating system in terms of several independent modes. The total current on the conductor surface is represented as a weighted sum of orthogonal eigencurrents, while the electric fields produced by these eigencurrents form orthogonal set over the infinite sphere [32], i.e., in the far field of the conducting body.

Mathematically, these modes can be obtained by applying the method of moments to the solution of Maxwell's equations on the boundary of the conducting body and diagonalizing the linear impedance operator in the resulting matrix equation. The solution of the general eigenvalue problem provides a set of real eigenpairs  $(\lambda_i, J_i)$  termed eigenmode [32]:

$$\lambda_i R J_i = X J_i$$

where  $R$  and  $X$  are real and imaginary parts of the general impedance matrix in the MoM

formulation;  $\lambda_i$  is the  $i^{th}$  eigenvalue;  $J_i$ s are the corresponding eigenvectors (or eigencurrents) that form an orthonormal set.

The eigenvalues are proportional to the difference between the magnetic  $W_{mag}$  and electric energy  $W_{el}$  stored on the antenna.  $w$  is the angular frequency.

$$\lambda_i = \frac{1}{2w}(W_{mag} - W_{el})$$

A positive eigenvalue indicates higher magnetic energy and denotes an inductive mode; a negative value is termed capacitive, while a zero eigenvalue is called an externally resonant mode. In the following, we always order the modes according to the ascending magnitude of the eigenvalue because the significance of the mode, i.e. its contribution to the radiated or scattered power, decreases with increasing magnitude.

Only few modes are needed to describe the currents on small and intermediately sized bodies. The total current  $J_{total}$  on the antenna can be represented as a weighted sum of the eigencurrents [32]:

$$J_{total} = \sum_{i=1}^n \alpha_i J_i$$

The weights  $\alpha_i$  are referred to as excitation coefficients and describe how well the energy from the excitation vector  $E$  is coupled into each mode [32].

$$\alpha_i = \frac{\langle J_i^* \cdot E \rangle}{(1 + \lambda_i j) \langle J_i^* R J_i \rangle}$$

TCM for conducting bodies was first introduced by Garbasc [28] and then developed by Harrington and Mautz [32]. It was also extended to the dielectric bodies [33] but did not receive much attention in the antenna community until the advent of accurate electromagnetic and mathematical tools and until cheap computational power became available.

Newman was the first to introduce the idea of a structural antenna [58]. He suggested to think of a small antenna mounted on a support structure (e.g. ship, airplane, tank) not

as the primary radiator but rather as a probe to excite currents on the support. He showed that by choosing the proper position radiation efficiency can be maximized. TCM was used to determine the optimum location and operating frequency. To excite mode  $n$  on the structure, the excitation probe should be placed at or near the maximum of  $J_n$ . The probe should be oriented in such a way that the excitation field  $E_i$  and current  $J_n$  are parallel [58]. This approach has been extended to pattern synthesis and placement of NVIS antennas [3]. Following the method developed by Mautz and Harrington, they determine the excitation coefficients and the total current on the structure that produces the required far fields. To calculate the excitation voltage for an  $N$ -port feed system, they select  $N$  segments -  $N$  distinct positions on the support structure - and estimate the excitation voltage vector  $V_s$  by solving an  $N$  by  $N$  linear system of equations [3]

$$V_s = [J_s^T]^{-1}[\alpha]$$

where  $J_s$  is the matrix containing the values of  $N$  scaled modal currents at  $N$  excitation segments and  $[\alpha]$  is the column vector with the excitation coefficients  $\alpha_n$ .

Lately, the procedure has been applied to multi-objective optimization of UAV [15] and NVIS shipboard antennas [16]. In these works, researchers apply the multi-objective evolutionary algorithm based on decomposition (MOEA/D) to find Pareto-optimal current vectors that satisfy three objectives, i.e. produce radiation in the desired directions, maximize the front to back ratio and constrain the amount of power in the main beam. For several Pareto solutions, feed probes are designed to excite the synthesized currents: the feeds are placed at the maxima of the most significant modal currents. The approach is validated by simulation and measurement of the scaled models.

The TCM has been instrumental in the design of electrically small antennas for mobile terminals [10], [1], [44], [54]. As miniaturization of mobile devices continues, the antennas are subjected to stringent size and shape constraints. To achieve acceptable performance,

the designers can take advantage of the phone structure, using the actual antenna element to excite the phone’s resonant modes. Cabedo et al. investigated in depth how the TCM can be applied to mobile antenna design and how the modes on the phone chassis can be excited efficiently [10]. A method for antenna matching based on impedance models from TCM is developed by Adams and Bernhard [1]. They seek to identify the near-optimum modes and couple energy into the existing modes rather than to create more complex radiating structures with resonant modes. The TCM has been applied to estimate the bandwidth potential - obtainable bandwidth - of non-resonant and electrically small antennas [62].

The use of TCM is very promising for MIMO applications: since characteristic modes are  $R$ -orthogonal to each other and there is no coupling of energy between them, exciting these modes independently would allow for multiple antenna systems to be integrated into one structure. Miers and Lau modify the phone chassis by adding a metallic bezel and shorting it to the casing: this way, they introduce an additional radiating mode below 1 GHz which is orthogonal to the fundamental chassis mode. Both modes become radiating in the GSM-850 band and if excited efficiently, can enable MIMO operation with high isolation [45]. They design excitation ports based on the analysis of the reactive near-field of the radiating modes: the first mode is excited at the maximum of the mode’s magnetic field with an inductive coupling element; the second feed - a folded monopole - excites the second mode at the maximum of the second mode’s electric field. With this approach, high isolation of the antenna ports is achieved [45]. The research group from Ohio applied characteristic mode analysis to automated feed design and to the reduction of mutual coupling between antennas [63].

## 2.2 Evolutionary Algorithms

In this work, we focus on population-based stochastic search algorithms (SSA), a class of algorithms widely used when little is known about the search landscape, optimal solutions

are not required, accurate simulation tools are available, and solution quality is valued over algorithm running time. This makes SSAs particularly attractive to solving real-world engineering problems, which are often not completely specified at the beginning of a project and may consequently undergo numerous modifications [73].

Evolutionary algorithms represent a large class of SSAs inspired by the biological evolution that operate through selection, mutation, and recombination [73]. Evolutionary algorithms start with a population of potential (or candidate) solutions and apply the principles of the survival of the fittest to produce better candidates. At each iteration, the fitness of every individual in the population is evaluated, multiple individuals are stochastically selected from the current population (based on their fitness) and modified (recombined and possibly randomly mutated) to form a new population. The algorithm terminates when either a maximum number of generations has been produced, or a satisfactory fitness level has been reached for the population. If the algorithm has terminated due to a maximum number of generations, a satisfactory solution may or may not have been reached.

A typical evolutionary algorithm requires two important components to be defined: 1) genetic representation of the candidate solutions, 2) a fitness function to evaluate and compare the solutions [25].

In Figure 2.1, we show the typical flow of an evolutionary algorithm for antenna optimization. The fitness of every antenna configuration is evaluated using NEC2C (Numerical Electromagnetics Code), an open source simulator which takes antenna geometry as input and computes far/near field radiation patterns, current and voltage distributions as well as antenna parameters such as gain and VSWR.

Evolutionary algorithms have proven capable in finding high-performance antenna designs with much less engineering labor than by-hand approaches [49]. They have been successfully applied to a variety of electromagnetic optimization problems, including phased array synthesis, the design of dual and multi-band patch antennas, aperiodic antenna ar-

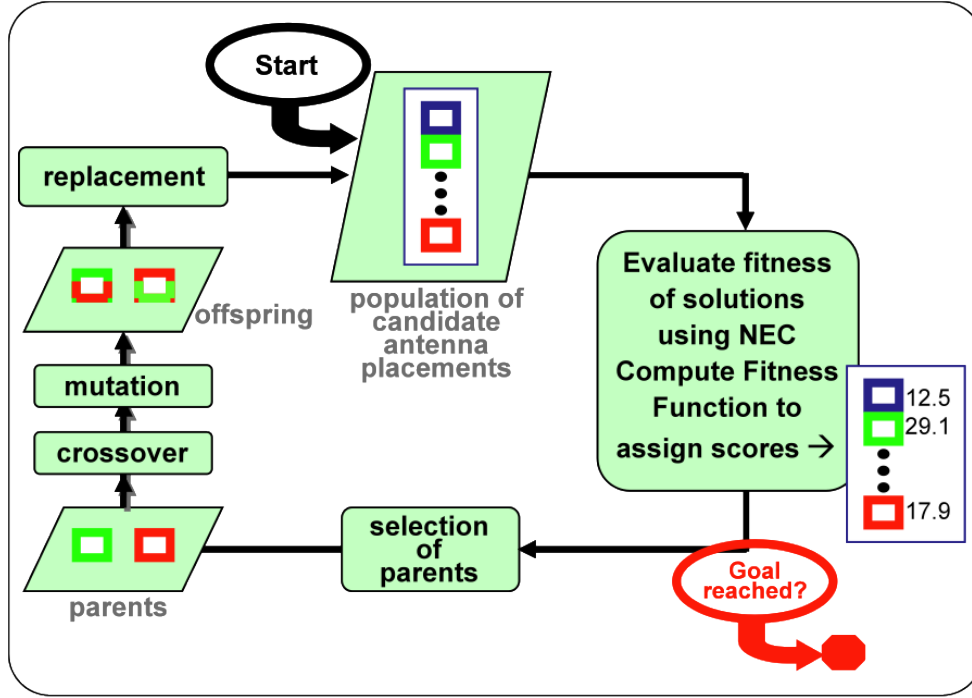


Figure 2.1: Flowchart of an evolutionary algorithm for antenna optimization.

rays, spacecraft antennas, and phase and amplitude pattern nulling of antenna arrays [39], [13],[41].

One major challenge in using stochastic techniques is the need to tune their parameters to achieve strong performance on a problem. Performance is commonly measured in terms of algorithm efficiency and effectiveness. Efficiency describes the ability of an algorithm to find solutions fast, i.e. using the least number of candidate solution evaluations. Effectiveness, on the other hand, describes its ability to find high-quality solutions: for instance, this is related to the ability to escape local optima and identify the most promising areas of the search space.

As electromagnetic simulations are computationally costly and algorithm performance is strongly problem dependent, it is important to understand each algorithms strengths and limitations before applying them to complex real-world problems. This can be done by running multiple tests of the algorithms on a number of benchmark problems, representative of the more complex fitness landscapes.

## 2.3 Multi-objective Optimization Algorithms

Let us consider a multi-objective minimization problem (MOP) with  $M$  objective functions  $F_i(x)$  subject to inequality constraints  $h(x) \leq 0$  and equality constraints  $g(x) = 0$ . The objectives and constraints are functions of  $x$ , which is a vector of design variables with dimensionality  $n$ . The goal of multi-objective optimization is to find a solution (solutions) that minimizes the objective functions and satisfies the constraints. However, a vector that simultaneously optimizes all of the objectives might not exist. In the case of competing objectives, we must define additional criteria on the quality of solution vectors. The Pareto optimality criterion states that the solution vector to a MOP must be non-dominated. For a minimization problem a solution  $x^*$  is said to be non-dominated if no other solution is better than  $x^*$  in all objectives. A distinction is made between weak and strong dominance.

**Definition 1 (Non-dominated solution)**  $\forall x \in X \setminus x^*, \quad \exists i \quad F_i(x^*) < F_i(x)$ ,

where  $X$  is the set of all feasible solutions, satisfying the constraints.

**Definition 2 (Strong dominance)** A solution  $x_1$  strongly dominates solution  $x_2$  ( $x_1 \prec x_2$ ), if  $\forall i \quad F_i(x_1) < F_i(x_2)$

**Definition 3 (Weak dominance)** A solution  $x_1$  weakly dominates solution  $x_2$  ( $x_1 \preceq x_2$ ),

if 1)  $\forall i \quad F_i(x_1) \leq F_i(x_2)$  and

2)  $\exists i \quad F_i(x_1) < F_i(x_2)$

Using the Pareto optimality criteria, the goal of multi-objective optimization is to obtain the globally optimal Pareto set, i.e., a set of vectors  $x^*$  that are non-dominated in the entire feasible space.

**Definition 4 (Pareto-optimal set)** The globally Pareto-optimal set is the set of all weakly non-dominated solutions in the feasible search space.

### 2.3.1 Classical Approach to Multi-objective Optimization

The classical approach to MOO (also referred to as preference-based) relies on scalarization of the problem: MOP is reformulated as a number of single-objective tasks (SOPs), the solution to which gives points on the Pareto front/set. The main strength of classical methods is the existence of convergence proofs. Most of them guarantee convergence to a Pareto-optimal solution. The main disadvantage is that one run can produce at most one solution and that the result is highly sensitive to the choice of the conversion parameters.

Three classical MOP formulations are the weighted sum formulation, the  $\epsilon$ -constraint formulation and the weighted metric method:

1. *Weighted sum formulation.* A new objective function is defined as a weighted sum of the initial objectives:

$$F_{scalar} = \sum_i \lambda_i F_i(x), \quad \lambda_i > 0$$

The weights  $\lambda_i$  express the importance of minimizing the corresponding objective [7]. A classical way of solving the MOP is to start multiple runs with various weight vectors to obtain multiple solutions along the Pareto front. The solution to this single-objective problem is guaranteed to be Pareto-optimal [55].

However, there is a number of issues associated with this approach. First, for non-convex MOPs it is not guaranteed that there exists a positive vector for every Pareto-optimal solution [55]. It is possible that not every Pareto-optimal point can be reached using a weighted sum of objectives. Second, the solution to the SOP is very sensitive to weight assignment. The choice of the weights is not intuitive: multiple sets might converge to the same solution; some runs might produce no feasible solution at all; there are no straightforward rules on how to set up preference vectors to obtain uniform distribution along the Pareto front. In addition, proper normalization of objectives is required to define a composite objective function. Finally, since each optimization run results in at most one point on the trade-off surface, this approach incurs significant computational cost. The

difficulties in choosing the weights further exacerbate this problem as the algorithm can be wasting computational resources on solving SOPs with unfortunate weight assignment.

2. In  *$\epsilon$ -constraint formulation* one objective is minimized, while other objectives are included in SOP as constraints and are upper bounded by  $\epsilon$ , where  $\epsilon$  is a positive vector [29]:

$$\begin{aligned} & \text{Minimize} && F_j(x) \\ & \text{subject to} && F_i(x) \leq \epsilon_i \quad i = 1 \dots M, \quad i \neq j \\ & && h(x) \leq 0 \\ & && g(x) = 0 \end{aligned}$$

Unlike the weighted sum approach, this formulation guarantees the existence of the  $\epsilon$ -vector for each Pareto-optimal solution for both convex and non-convex MOPs. The other shortcomings of the weighted sum method also apply to this approach.

3. *Weighted metric formulation:*

$$\begin{aligned} & \text{Minimize} && l_p(x) = \left( \sum_{j=1}^M w_j |F_j(x) - z_j^*|^p \right)^{(1/p)} \\ & \text{subject to} && h(x) \leq 0 \\ & && g(x) = 0 \end{aligned}$$

Objective function is defined as the distance from the current solution to some ideal solution  $z^*$  in the objective space. The most popular formulation is minimization of the  $l_p$  distance or minimization of the maximum weighted deviation in all dimensions  $l_{\inf}$  (Tchebycheff problem) [21, p. 59]. When the weighted Tchebysheff metric is used, any Pareto-optimal solution can be reached [55].

### 2.3.2 Evolutionary Approach to Multi-objective Optimization

Evolutionary algorithms take a population-based approach to solving the MOP. They start with a set of candidates and by applying stochastic operators (recombination, mutation, survival and offspring selection) attempt to reach the most accurate approximation of the Pareto-optimal front in one run.

In order to steer the search toward non-dominated solutions, fitness assignment strategies that rely on dominance relations within the current population and distribution/density of the candidates in the search space have been developed. Most of the algorithms maintain a current - 'working' - population and an external population that contains the non-dominated vectors found by the algorithm so far. At each iteration, the external population is updated with new non-dominated solutions, while individuals from both populations are used to generate offspring.

In this work, we characterize the performance of two MOEAs on coupled optimization problems - the Strength Pareto Evolutionary Algorithm 2 (SPEA2) [84] and the Elitist Non-dominated Sorting Genetic Algorithm II (NSGA-II) [23]. The algorithms take different approaches to fitness assignment and elitist preservation in the search for Pareto solutions and both have shown superior performance on multiple benchmark problems [21].

NSGA-II performs diversity maintenance by using crowding comparison and tournament selection. The algorithm starts with a randomly initialized population of size  $2N$ . Dominance sorting is performed in which the population is subdivided into multiple non-dominated fronts: each non-dominated front includes the individuals with the same rank, equalling the number of solutions in the population that the individual strongly dominates. The offspring population is filled with the individuals from different fronts. Competition between solutions is decided using crowded tournament selection: solution that belongs to a better front wins; if two solutions have the same rank, the solution that lies in a less crowded region wins. This sorting procedure defines  $N$  individuals to be included in the

offspring. After the offspring is modified by crossover and mutation and evaluated, new population is combined with the parent population. The selection procedure is repeated. Computational complexity of the algorithm is determined by non-dominated sorting. For a population with size  $N$  and  $M$  objectives, the sorting procedure requires  $O(MN^2)$  computations [21].

SPEA2 - another elitist MOEA - was developed and improved by Thiele and Zitzler [84]. It differs from NSGA-II in that it explicitly keeps an archive of non-dominated solutions. At each iteration, the archive is updated with new non-dominated solutions from the current population and the existing archive. If the archive grows beyond a specified size, the more crowded individuals are deleted from the elites.

Both the external (archive) and the working population are used to produce offspring. Every individual is assigned *strength* based on how many solutions in the combined population it dominates. Then the fitness of each solution is calculated as the sum of the strengths of all members that weakly dominate it. To avoid the situation in which individuals dominated by the same solutions have the same fitness, density information is incorporated into the fitness function: the inverse of the distance to the  $k$ th nearest neighbor is added to the individual's raw fitness. The archive is filled with non-dominated solutions from the current archive and working population. If the number of non-dominated individuals exceeds archive size, truncation operation is applied: at each stage, the individual with the smallest distance to its nearest neighbor is deleted; if multiple individuals have the same distance, the tie is broken by considering the second neighbor and so on. The mating pool is selected from the combined population using binary tournament, and the offspring is modified by crossover and mutation.

Run-time complexity of SPEA2 is governed by the complexity of the truncation operation, which in the worst case is  $O((\bar{N} + N)^3)$ , where  $\bar{N}$  denotes the size of the archive. The average complexity is lower at  $O((\bar{N} + N)^2 \log(N + \bar{N}))$  [84].

### 2.3.3 Multio-bjective Optimization with Local Search

Multi-objective algorithms explore and exploit the search space by applying various stochastic operators to a population of candidate solutions. It has been shown that including a local search step in an evolutionary algorithm (called hybridization) improves the effectiveness of the algorithm and allows for reaching higher precision in the Pareto solutions [34], [36]. Hybrid EMO was first applied by Ishibuchi and Murata [34] to flowshop scheduling. Their algorithm uses scalarization of the objectives with a random set of weights for fitness assignment during parent selection and applies local search to each offspring produced by regular genetic operators. Jaskiewicz describes the multi-objective genetic local search (MOGLS) for the 0/1 knapsack problem. At each iteration, local search is performed on the offspring population [36].

Evolutionary strategies (ES), multi-objective steepest descent method (MSDM), combined-objectives repeated line search (CORL) have been investigated as local optimizers in MOEAs. Harada et al. suggested a new local search method - a Pareto Descent Method (PDM) - which moves the solutions along the descent directions to improve all objective functions simultaneously [31]. NSGA-II was hybridized with the reference point method used in MSDM [70]: an achievement scalarizing function (ASF) defined as the maximum of the distance from an objective to the ideal reference point was minimized. At each iteration, a subset of offspring population was selected for the local search. The minimization problem was solved using mathematical programming algorithms. On a number of benchmark problems the hybrid approach was faster and more accurate in getting to the Pareto-optimal solutions than the original NSGA-II [69]. An archive-based micro genetic algorithm (AMGA) switches between the regular mutation and the gradient-based optimization as the mutation operator. Every several generations, each individual in the offspring is optimized using the sequential programming method (SQP). The objective function is defined as a weighted sum of the objectives; in addition, constraints on the

objective values are introduced such that the local solution always dominates the starting point [76]. The authors show that SQP speeds up the search and helps obtain the fine-grained objective values. Though the hybrid AMGA is successful in discovering the global Pareto solutions, the spread of these solutions is not uniform and further diversity preservation operators are required. In highly multi-modal problems, the search is not able to escape the locally optimal basins of attraction [76]. More recently, Lara et al. presented a hill climber with side step (HCS) as a local search procedure in a multi-objective memetic algorithm [43].

MOEA with decomposition (MOEA/D) can be included into the class of memetic algorithms [82]. The optimization problem is decomposed into multiple subproblems (SOPs) each described by an aggregation function which can be defined using a weighted sum of several objectives, a Tchebysheff approach or boundary intersection approach [82]. Each problem maintains one solution in memory during the search and generates new solutions by combining the genotypic material from its neighbor subproblems. The neighborhood relation is defined by the distance between the subproblem's weighting vectors. The locally optimal solution for each subdomain can be achieved by optimizing the assigned function in a local search procedure.

### 2.3.4 Challenges for MOEAs

Deb names two main tasks of the multi-objective optimization: first, it should converge as close to the true Pareto-optimal region as possible; second, it should maintain as many widely spread non-dominated solutions as possible [21, p. 332]. He also identifies the main characteristics of the search space that can make these tasks difficult for the MOEA. As in single-objective optimization, multi-modality, deceptive attractors, isolated optima, and collateral noise may cause major challenges for the algorithm to converge to the global Pareto front [21, p. 333]. In achieving the second task, the major hurdles are the non-

convexity/concavity, discontinuity of the Pareto front, and the non-uniform distribution of the solutions in the search space [21, pp. 333-340]. Most MOEAs favor solutions of intermediate quality since the survival probability of the candidate depends on how many solutions it dominates. This puts individual champions at a disadvantage. For discontinuous Pareto fronts the competition between the solutions in various Pareto sub-regions may lead to the extinction of some of these regions. The non-uniform distribution of the solutions makes it difficult for the algorithm to locate Pareto regions with lower density.

Constrained optimization further exacerbates the difficulties: adding hard constraints to the problem can make part of the unconstrained Pareto front infeasible or can shift parts or the entire Pareto front to the constraint boundary.

### 2.3.5 Performance Metrics

In assessing an MOA's performance, three measures are important [21, p. 306]: first, the ability of the algorithm to maintain diversity of the solutions along the Pareto front; second, its ability to converge to the global Pareto front (lateral to the front); third, its ability to handle different shapes of the Pareto front (discontinuous, convex or non-convex).

The set coverage metric is commonly used to determine how close the Pareto set  $Q$  obtained by the algorithm approaches the known Pareto set  $P$  [83]. Given two solution vectors  $P$  and  $Q$ , the set coverage metric  $C(P, Q)$  calculates the proportion of solutions in  $Q$  weakly dominated by solutions in  $P$  [21, p. 311]. This metric is useful in comparing the found solution to the true Pareto front and comparing two algorithms with each other.

$$C(P, Q) = \frac{|\{q \in Q \mid \exists p \in P : p \preceq q\}|}{|Q|}$$

To monitor the convergence of the algorithm toward the global Pareto front, the generational distance (GD) is used. GD calculates the average distance of the solutions in  $Q$

from the solutions in  $P$  [78].

$$GD = \frac{\left(\sum_{i=1}^{|Q|} d_i^p\right)^{1/p}}{|Q|}$$

The distance  $d_i$  is the Euclidean distance in the objective space between the solution  $q_i \in Q$  and the nearest solution  $p_j \in P$

$$d_i = \min_j \sqrt{\sum_{m=1}^M (f_m^i - f_m^j)^2}$$

The variance of the GD is calculated to verify that the metric measures the distance to the Pareto front rather than the fluctuations in the distance values. Also, the objective values are normalized to calculate the distance measure.

The diversity metric measures the distribution of the solutions along the Pareto front. We use the metric proposed by Deb et al. [21, p. 314].

$$\delta = \frac{\sum_{m=1}^M d_m^e + \sum_{i=1}^{|Q|} |d_i - \bar{d}|}{\sum_{m=1}^M d_m^e + |Q| \bar{d}}$$

where  $Q$  is the set of the solutions obtained by the algorithm,  $M$  is the number of objectives,  $d_i$  is some distance measure between the neighboring solutions (in this work, the crowding distance) and  $\bar{d}$  is their mean value. The distance  $d_m^e$  is the distance between the extreme solutions of the true Pareto and found Pareto solutions corresponding to the  $m$ -th objective function.

In general, the set of non-dominated solutions is most diverse when the spread is close to zero. However, in the problems where the Pareto front consists of multiple distinct regions in the search space or includes individual champions, low spread value might indicate that some of the Pareto regions were not found by the algorithm. In such cases, the value should be compared to the spread of the true Pareto front, or the metric can be calculated separately for each cluster of solutions.

## 2.4 Summary

In this chapter, we have reviewed the background for the research in the following sections. The TCM proves very promising for coupled structural-electromagnetic optimization because it provides information about the resonant frequency and radiating properties of the conductive body based on the body's topology (geometry and materials). TCM-based objectives can be used to guide the optimization procedure in the EM domain. Without the defined feed, TCM can not distinguish between the various EM objectives (VSWR, gain, polarization) but it may not be necessary in the initial stages of the search. The TCM-based optimization in the EM domain would allow for better integration with the existing techniques in the structural optimization.

This research focuses on stochastic search for solving the coupled optimization problems. Evolutionary algorithms have proven very successful in the field of multi-objective optimization, because they can find multiple Pareto-optimal solutions in one run. Hybridizing evolutionary algorithms with local search can further improve an algorithm's performance, though it often requires special operators for maintaining a diverse set of solutions. Memetic algorithms are of particular interest as they provide a way to combine the domain-specific algorithms for the most efficient and effective multi-disciplinary optimization.

# Chapter 3

## Automated Antenna Design using the Theory of Characteristics Modes

### 3.1 Introduction

In this chapter, we develop algorithms for automated antenna design and optimization based on the Theory of Characteristic Modes (TCM). Integrating antennas as structural elements requires a new approach to optimization in the EM domain. Unlike traditional antenna optimization described in Chapter 1, structural antennas are electrically connected to a larger metallic structure, whose shape and topology is dictated by mechanical considerations (e.g., the structure must bear specific loads or enclose a certain volume) and whose radiating performance is unknown a-priori. In order to turn an arbitrary metallic structure into an efficient radiator, we must solve the following tasks: a) determine a structure's potential to radiate in the frequency band of interest; b) modify the structure such that it resonates in the desired band; c) find the feed configuration that best satisfies the specifications.

TCM is well suited for all of the tasks because it gives valuable information about the EM performance based on a structure's topology and does not require full electromagnetic

analysis to characterize its EM properties. A theory of characteristic modes describes the behavior of a scattering or radiating system in terms of several independent modes. The total current on the conductor surface can be decomposed into a weighted sum of orthogonal eigencurrents, while the electric fields produced by these eigencurrents form orthogonal set over the infinite sphere [32], i.e. in the far field of the conducting body. In other words, the total current and the radiation pattern can be represented as a composition of the individual eigenmodes: the contribution of each mode to the full EM performance is determined by the feed configuration.

This chapter is organized as follows. In section 3.2, we introduce a procedure for automated feed placement and verify it on a number of conventional antennas. In section 3.2.1, we investigate how TCM can be applied to automated antenna design by deriving the TCM-based objectives (radiation efficiency and matching). Their advantages and limitations in guiding the search procedure toward optimal designs are discussed in section 3.3. We support our findings with results on several test problems (section 3.3.2). Finally, the TCM-based objectives and feed placement are used to solve two real-world optimization problems in the EM domain: integration of a GPS antenna with the frame of a mobile phone and integration of an S-band antenna with the face of a CubeSAT (sections 3.3.5 and 3.3.6).

## 3.2 Power Analysis Based on TCM

In this section, TCM is used to determine the best feed point for an arbitrary wire antenna. A general procedure for optimizing the excitation vector  $E$  was presented in [63]. Inspired by compressive sensing, the algorithm applies gradient-based optimization to find an excitation vector consistent with the specified set of excitation coefficients. Though the algorithm is robust and can find general excitation vectors, the procedure is semi-automated and requires an intelligent initial guess for excitation coefficients as well as the

inspection of the resulting plots by the human designer. In addition, the authors do not perform convergence analysis or identify clearcut criteria when the optimization procedure fails or succeeds. Previous research on the design of structural antennas has focused on synthesizing the currents on the existing structures and then attempting to design feed networks to excite these currents at the maxima of the current modes. The research on feed design and placement optimizes voltage vectors that in the end must be converted into practical feed design. Our research addresses a different problem: rather than exciting particular modes on an antenna [63], we are interested in the rapid assessment of the radiating properties of an arbitrary metallic structure. This procedure will be integrated with the optimization routine that modifies the initial topology, should be lightweight and allow designers to quickly compare the radiating properties of one candidate wire structure against another.

The developed procedure determines the placement of an inductive/coaxial feed. The antenna is excited by a sinusoidal voltage source with 1V magnitude and  $0^\circ$  phase shift. We assume a perfectly conducting structure composed of wires and plates radiating into free space.

The power accepted by the structure from the excitation source is the main criterion for evaluating antenna's radiation efficiency. For the perfectly conducting antenna in a lossless medium, the power accepted by the antenna is partly stored in the antenna (reactive power) and partly radiated into the far field. In this section, we will also determine conditions on the power to obtain well-matched designs. For many common antenna shapes (dipoles, Yagi-Uda, PIFAs, etc.) formulas and empirical guidelines exist to tune the antenna performance. However, for an arbitrary metallic structure, either obtained as a result of generative optimization or prescribed by other constraints, feed placement may not be obvious or easily predicted. In the following, we provide mathematical analysis based on TCM, demonstrate the ability of the feed placement algorithm to predict best feed position

on a number of standard structures and apply them to arbitrary shapes.

The following derivations build on the background material discussed in section 2.1. To reiterate,  $R$  and  $X$  are real and imaginary parts of the general impedance matrix in the MoM formulation;  $\lambda_i$  is the  $i^{th}$  eigenvalue;  $J_i$ s are the corresponding eigenvectors (or eigencurrents) that form an orthonormal set. The notation  $J^*$  denotes a conjugate transpose of vector  $J$ , and  $\langle \dots \rangle$  denotes the inner product.

Consider  $n$  modes that possess the eigenvalues with the smallest magnitude; the input power to the antenna can be expressed as [63]:

$$P = \frac{1}{2} \langle J_{total}^* R J_{total} \rangle$$

$$P = \frac{1}{2} \sum_{i=1}^n \alpha_i^2 \langle J_i^* R J_i \rangle = \frac{1}{2} \sum_{i=1}^n \frac{\langle J_i^* \cdot E \rangle^2}{(1 + \lambda_i^2) \langle J_i^* R J_i \rangle}$$

For the delta-gap source placed on segment  $x$ , there is only one non-zero entry in the excitation vector  $E = \begin{bmatrix} 0 \dots e_x \dots 0 \end{bmatrix}'$ . Substituting  $E$  and assuming that eigencurrents are normalized such that  $\langle J_i^* R J_i \rangle = 1$ ,  $P$  becomes:

$$P_x = \frac{1}{2} \sum_{i=1}^n \frac{((J_i)_x \cdot e_x)^2}{1 + \lambda_i^2} = \frac{1}{2} (e_x)^2 \sum_{i=1}^n \frac{(J_i)_x^2}{1 + \lambda_i^2}$$

The goal is to find segment  $x$  that maximizes the input power  $P$  to the antenna.

Besides increasing the radiated power, it is desirable to match the antenna's input resistance to  $50 \Omega$ . We can derive the conditions on the modes by considering antenna's resistance  $R_x$  at feed segment  $x$ . The eigencurrents in the following expressions are assumed to be taken at the feed segment and we drop the subscript  $x$  for clarity of presentation.

We also assume that the segments have equal lengths and omit the factor  $e_x^2$ :

$$\begin{aligned}
R_x &= 2 \frac{Re(P)}{|J_x|^2} = 2 \frac{P_x}{|J_x|^2} \\
R_x &= 2 \frac{0.5 \sum_{i=1}^n |\alpha_i|^2}{(\sum_{i=1}^n \alpha_i |J_i|)^2} = \frac{\sum_{i=1}^n |\alpha_i|^2}{\sum_i |\alpha_i|^2 |J_i|^2 + Re(\sum_{i \neq j} \alpha_i \alpha_j^* |J_i|^2 |J_j|^2)} \\
R_x &= \frac{\sum_i \frac{1}{(1+\lambda_i^2)} J_i^2}{\sum_i \frac{1}{(1+\lambda_i^2)} J_i^4 + \sum_{i \neq j} \frac{1+\lambda_i \lambda_j}{(1+\lambda_i^2)(1+\lambda_j^2)} J_i^2 J_j^2} = \frac{\sum_i \frac{1}{(1+\lambda_i^2)} J_i^2}{\sum_j \sum_i \frac{1+\lambda_i \lambda_j}{(1+\lambda_i^2)(1+\lambda_j^2)} J_i^2 J_j^2}
\end{aligned} \tag{3.1}$$

Note that the dimensions are correct because the currents are normalized such that  $\langle J_i R J_i \rangle = 1$ :

$$[\Omega] = \frac{[1]}{(A/\sqrt{W})^2} = \left[ \frac{W}{A^2} \right]$$

Define the normalized real and imaginary power components  $P_r$  and  $P_{im}$  as:

$$\begin{aligned}
P_r &= \frac{1}{2} \sum_i \frac{J_i^2}{(1+\lambda_i^2)} \\
P_{im} &= \frac{1}{2} \sum_i \frac{\lambda_i J_i^2}{(1+\lambda_i^2)}
\end{aligned}$$

Then the denominator in equation (3.1) can be expressed as:

$$denominator = \sum_i \frac{J_i^2}{(1+\lambda_i^2)} \sum_j \frac{J_j^2}{(1+\lambda_j^2)} + \sum_i \frac{\lambda_i J_i^2}{(1+\lambda_i^2)} \sum_j \frac{\lambda_j J_j^2}{(1+\lambda_j^2)} = 4P_r^2 + 4P_{im}^2$$

Substituting into equation (3.1), the input resistance becomes:

$$\begin{aligned}
R_x &= \frac{2P_r}{4P_r^2 + 4P_{im}^2} \\
R_x &= \frac{1}{2} \frac{P_r}{P_r^2 + P_{im}^2}
\end{aligned}$$

Rewriting, we obtain:

$$\begin{aligned} P_r^2 - \frac{1}{2R_x}P_r + P_{im}^2 &= 0 \\ (P_r - \frac{1}{4R_x})^2 + P_{im}^2 &= \frac{1}{16R_x^2} \end{aligned}$$

The solution to the initial equation is expressed as a function of normalized real and imaginary power components  $P_r$  and  $P_{im}$ . Solutions lie on a circle centered at  $(\frac{1}{4R_x}, 0)$  and of radius  $r = 1/(4R_x)$ . The feeds that result in power values on or close to the circle boundary are promising in terms of the real input resistance. To achieve best matching, we want to minimize the imaginary power and obtain the points to the right side of the circle where  $P_{im}$  goes to 0 and  $P_r$  equals  $1/(2R_x)$ . We could have arrived at this conclusion by considering a  $1V$  excitation source attached to the antenna with a purely real impedance  $R_x$ .

In TCM, the above condition can be written as a system of equations linear in the variables  $t_i = J_i^2$ . Geometrically these equations represent two hyperplanes in an  $n$ -dimensional space, where  $n$  is the number of eigenmodes. The intersection of these planes defines the set of possible solutions

$$\begin{aligned} \sum_i \frac{1}{1 + \lambda_i^2} J_i^2 &= \frac{1}{R_x} \\ \sum_i \frac{\lambda_i}{1 + \lambda_i^2} J_i^2 &= 0 \end{aligned}$$

As an example, consider a metallic wire structure that possesses one strong radiating mode with  $|\lambda_1| \approx 0$  and  $|\lambda_1| \ll |\lambda_2|$ . In this case, the contribution from the first mode determines the current flowing on the antenna, and the upper modes can be ignored. The system reduces to one equation in terms of the first eigencurrent:  $J_1^2 = \frac{1}{R_x}$  or equivalently  $J_1 = \frac{1}{\sqrt{R_x}}$ . The segment for which the value of the first eigencurrent  $J_1$  approaches the inverse of the desired input resistance should be chosen as the antenna feed. If the input resistance cannot be physically realized, then the maximum of the eigencurrent determines the feed position with the highest possible input resistance.

### 3.2.1 Relation between the Radiated Power and Matching

Voltage standing wave ratio (VSWR) is one of the widely used measures of how well an antenna is matched to a source. We can derive a lower bound on the VSWR in terms of the real resistance and radiated power. The relation between the power and the VSWR can be expressed as follows:

$$\begin{aligned}
 \Gamma &= \frac{Z - Z_0}{Z + Z_0} = \frac{R + jX - R_{des}}{R + jX + R_{des}} \\
 |\Gamma| &= \frac{\sqrt{(R^2 - R_{des}^2 - X^2)^2 + (2XR)^2}}{(R + R_{des})^2 + X^2} \\
 \text{VSWR} &= \frac{1 + |\Gamma|}{1 - |\Gamma|} \\
 &= \frac{(R + R_{des})^2 + X^2 + \sqrt{(R^2 - R_{des}^2 - X^2)^2 + (2XR)^2}}{(R + R_{des})^2 + X^2 - \sqrt{(R^2 - R_{des}^2 - X^2)^2 + (2XR)^2}} \\
 &\geq \frac{(R + R_{des})^2 + |R^2 - R_{des}^2|}{(R + R_{des})^2 - |R^2 - R_{des}^2|} \\
 \text{VSWR}_{min} &\geq \begin{cases} \frac{R_{des}}{R} & \text{if } R \leq R_{des} \\ \frac{R}{R_{des}} & \text{if } R > R_{des} \end{cases}
 \end{aligned}$$

With the assumption of zero imaginary power, we can rewrite this condition in terms of the radiated power

$$\text{VSWR}_{min} \geq \begin{cases} \frac{P_r}{P_{des}} & \text{if } P_r \geq P_{des} \\ \frac{P_{des}}{P_r} & \text{if } P_r < P_{des} \end{cases} \quad (3.2)$$

Here,  $P_{des} = \frac{1}{2R_{des}}$  is the power radiated by an antenna with a purely real resistance  $R_{des}$  and excited by the voltage source with 1V amplitude. An example of the relation between the power and the VSWR for various mesh antennas is shown in Figure 3.1. Cross symbols

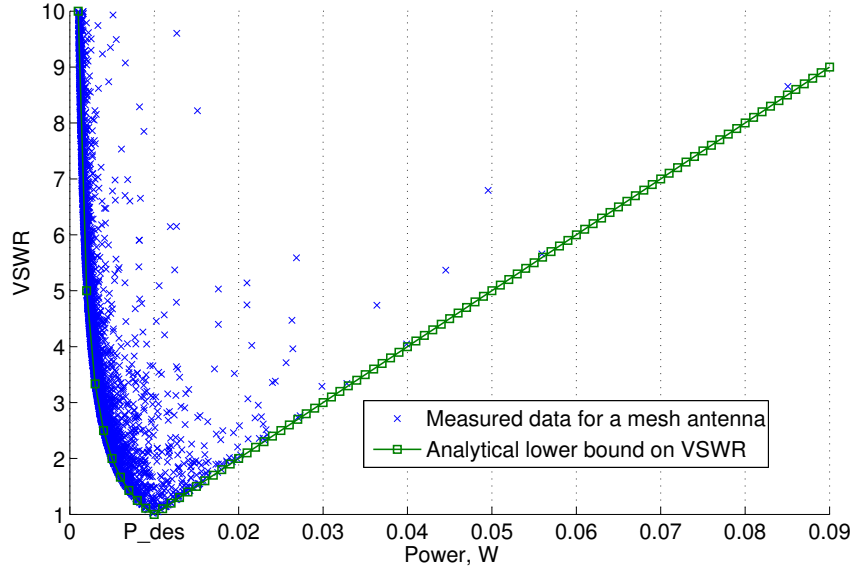


Figure 3.1: VSWR as a function of radiated power: green boxes show the lower bound on VSWR calculated from Equation (3.2); blue crosses are power values calculated from TCM for various antennas.


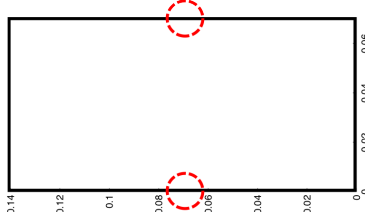

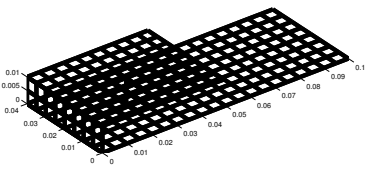
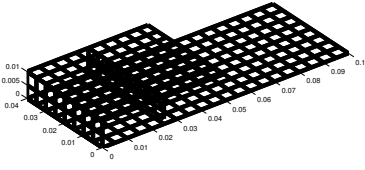
correspond to numerically calculated VSWR and power of multiple grid antennas. Box symbols denote the lower bound determined from the equation above. The desired input resistance is  $50 \Omega$ , and the radiated power at the best matching point equals to 10 mW. For most designs, the radiated power is below the desired value so that increasing the power most likely leads to improvement in VSWR. The power value close to 10 mW is a necessary but not sufficient condition to achieve a better matching. When choosing the feed, we want not only to increase the real power but also to find a way to move closer to the boundary by decreasing the imaginary component.

The derived conditions can be used in two ways: a) to determine the segment on the antenna that results in the highest radiation resistance; b) as objectives in the optimization procedure based on TCM. In an optimization procedure, antennas with different topologies are compared to each other: the variations in the radiated and stored power across the designs might be significant so that the use of the real power component alone might not provide sufficient guidance to the algorithm. However, if we need to compare the

potential feed positions within a given design, the real power can often predict feasible source positions with good matching. For a number of standard antennas, the maximum radiated power determines the standard position of the feed. In the following section, we investigate how the real power from TCM can be used for feed placement.

### 3.2.2 Feed Placement for Dipole, Yagi-Uda, Wire Loop and PIFA Antennas

Table 3.1: Standard antenna shapes used to verify TCM-based algorithm for feed placement. Red circles show best positions for the voltage gap source.

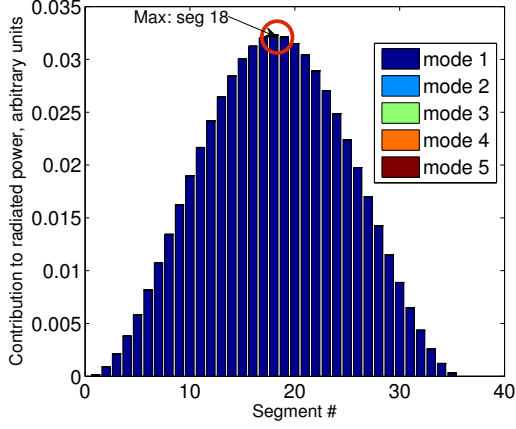
Antenna type	Description	Resonance	Best Feed
	centrally fed $\lambda/2$ dipole	850 MHz	central segment 18
	wire loop ; width x height at resonance $0.2\lambda \times 0.4\lambda$	850 MHz	center of the long side (segments 15 and 56)
	Yagi-Uda antenna	2.45 GHz	center of the driving element (segment 18)
	wire grid model of the PIFA antenna [10] with a shorting wall along the width of the patch	1.6 GHz	wire connecting the ground plane and the top element
	wire grid model of the PIFA antenna [10] with two shorting walls: a vertical plate between the top and ground patches is added	1.6 GHz	wire connecting the ground plane and the additional vertical element

We verify the performance of the proposed algorithm for each antenna type listed in Table 3.1. The following analysis is performed: first, we investigate VSWR or return loss in the band of interest to confirm the antenna’s resonant frequency and bandwidth. For the same frequency range, we perform the eigenvalue analysis and show how the radiating modes explain the resonance. Finally, at the resonant frequency we apply the excitation source at each potential feed position (for small antennas, simulation is performed for each segment of the design) and record VSWR and the power accepted by the antenna calculated from TCM.

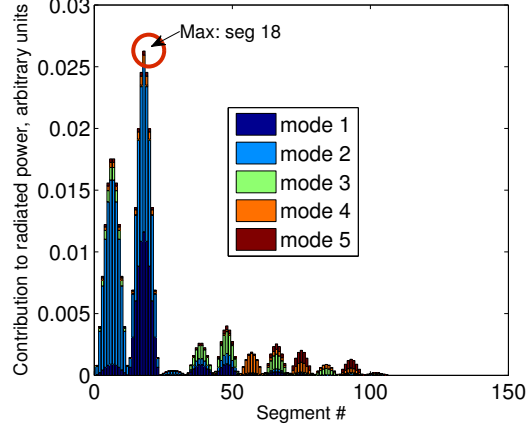
Figure 3.2 summarizes representative results: bar graphs show the contribution of each radiating mode to the radiated power for standard antenna types. Segment numbers along  $x$ -axis indicate the position of the feed for which the power is estimated. The segment with the maximum power value determines the feasible feed position.

For antennas with one dominant radiating mode (e.g., dipole), the maximum current of this mode corresponds to the best feed position. The total current on the antenna is most similar to the first eigencurrent at the resonance, which is solely responsible for the radiation at the resonant frequency. In the case of the loop antenna, though the first radiating mode dominates ( $\lambda_1 = 0.745$ ;  $\lambda_2 = 2.8$ ) and still determines the best feed points (centers of the long side of the loop), the second mode becomes prominent and might be excited independently of the first mode at the center of the short side. In the case of the Yagi-Uda antenna, two modes get close to zero around 2.45 GHz. The second mode contributes at least half of the radiated power when the antenna is excited at the driving element, so that both modes are responsible for the resonance.

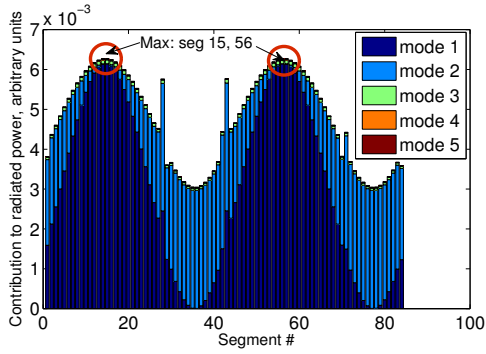
The two PIFAs are used to validate algorithm performance on wire grid models. The PIFA-like structures represent a folded mobile chassis with an inductive feed and a distributed feed developed for broadband operation and were investigated in depth in [10]. All wire grid plates satisfy the empirical rule for accurate grid modeling [66], i.e. for the square



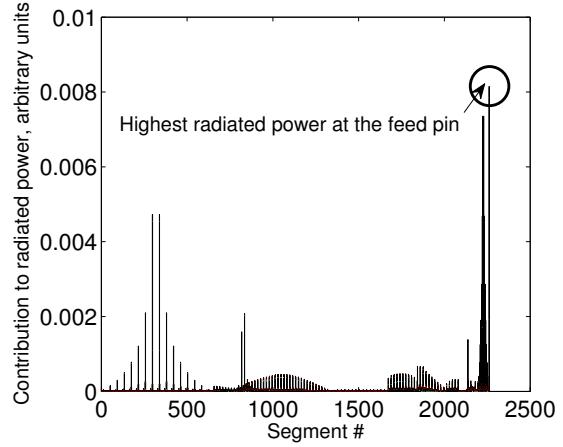
(a) Dipole antenna



(b) Yagi-Uda antenna



(c) Loop antenna



(d) PIFA antenna

Figure 3.2: Power contribution calculated from TCM for different antenna types. Segment numbers along  $x$ -axis indicate the position of the feed for which the power is estimated. Segments with the maximum power value determine the best feed position.

grid, the radius of the wire is chosen as the segment length squared divided by  $\pi$ . The simulation of the return loss/impedance of the wire grid model run in NEC2C is verified against the full MoM simulation in WIPL-D. The TCM analysis using wire grid models in NEC2C agrees well with the results in [10] that use plate models of the antennas. For both PIFAs, segments connecting the upper and lower plates are identified as the best feed positions.

### 3.2.3 Feed Placement for an Arbitrary Wire Structure

Upon validation of the TCM-based algorithm on standard antennas for which the feed position is known, we apply it to an arbitrary wire structure which represents the central part of the phone's frame, also called endoskeleton. TCM analysis shows that the structure possesses several strong radiating modes above 1.5 GHz which is promising for the use in the GSM, GPS and WiFi bands. A prominent radiating mode exists around 1GHz - close to the GSM-900. Figure 3.3a shows the antenna input power calculated using full electromagnetic simulation and power predicted from ten characteristic modes at 2.45 GHz. The best candidate for the excitation source at this frequency is segment 58.

Because the modes are frequency dependent, the power contributions and the optimal feed placement also change with frequency. Figure 3.3b shows the distributions at 850 MHz. There is only one prominent mode that can be most efficiently excited at segment 26.

Figure 3.3c demonstrates how the source placement affects antenna's VSWR. VSWR is a measure of mismatch loss between a  $50\ \Omega$  voltage source and the antenna and is also a suitable measure of the radiation performance for a lossless wire antenna. The radiation resistance is equivalent to the real part of the impedance taken at the current maximum, which corresponds to the highest power that can be accepted and radiated by this structure. As expected, at 850 MHz feeding at segment 26 results in a better VSWR, while segment 58 gives better performance at 2.45 GHz. Both feeds produce resonances at 1040 MHz, 1340 MHz and around 2000 MHz. The power analysis, however, fails to predict the correct ordering (in terms of VSWR) of the most promising segments at the resonant frequencies: it can identify candidates for good source positions (all produce VSWRs close to 2) but the ranking based on power values does not reflect the ordering based on VSWR. This is investigated further in the following sections.

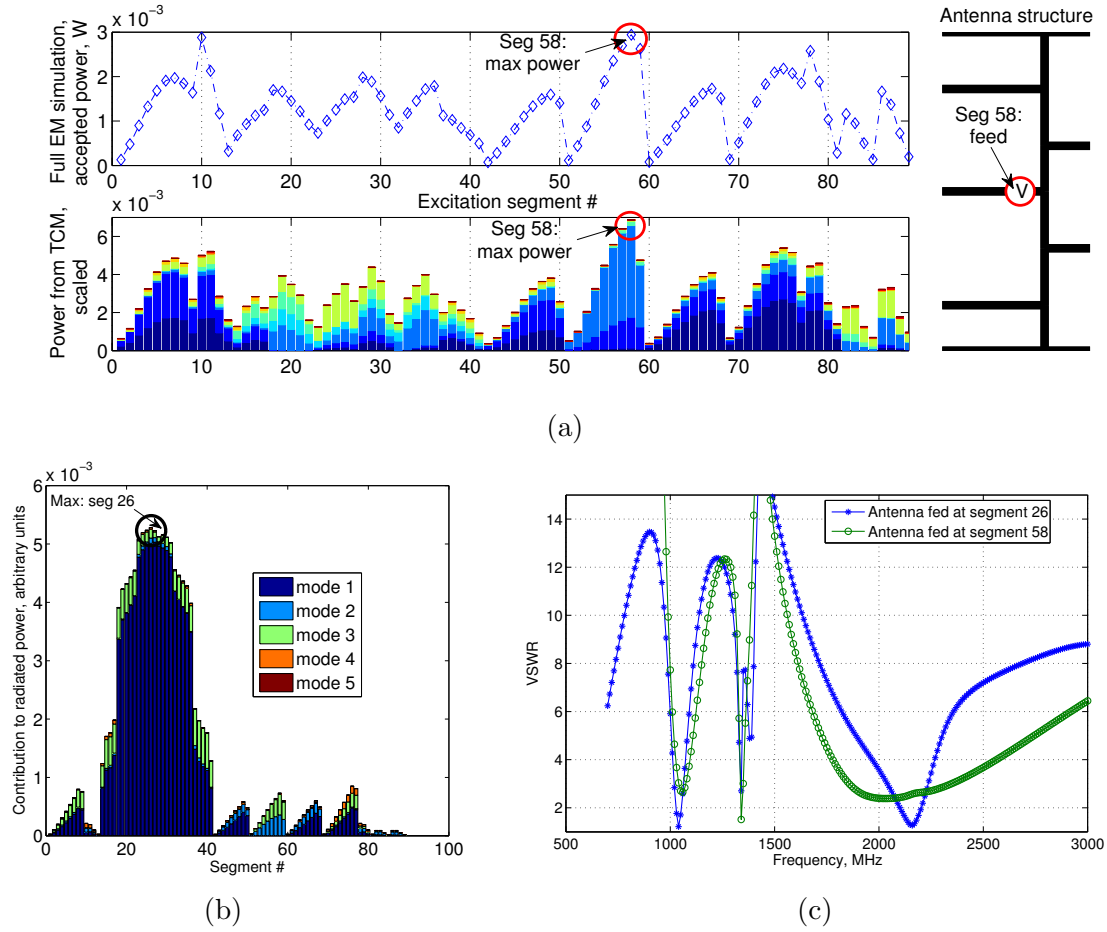


Figure 3.3: Feed placement for an arbitrary wire structure. (a) Comparison of potential feed points based on the radiated power for the given antenna structure (2450 MHz); (b) Input power to the antenna estimated from TCM at 850 MHz; (c) VSWR for the two feed positions determined from TCM analysis.

### 3.3 Using TCM in an Optimization Procedure

In this section, we investigate how information obtained from TCM can be used to guide EM optimization. The eigenmodes provide useful data so that the algorithm can identify the most promising areas of the search landscape. In the exploitation phase, full EM analysis can be run to fine-tune the solution.

Antenna optimization is a multi-objective, multi-constrained problem: the figures of interest include impedance, radiation efficiency, directionality, polarization, and bandwidth. The constraints can include the size and weight of the antenna and the position of the feed. A common approach is to define the fitness function as the weighted sum of all objectives. The geometric constraints are usually checked explicitly, and infeasible geometries are not allowed. EM constraints are incorporated into the objective using a penalty function. For EM optimization problems, the resulting composite objective function is usually non-linear, non-convex, and multimodal.

The weights express the trade-offs between the multiple objectives that the designer defines based on his/her knowledge and intuition. However, multiple objectives and non-linear interactions between the optimization variables (hysteresis) make the choice of the weights a challenging task. In the complex EM problems, these interactions are not always obvious or easily predicted so that a trial and error approach is often necessary to determine acceptable weights. Failed weight assignment can impede the effectiveness and efficiency of the search in many ways: for example, it can lead the search away from good quality solutions, favoring mediocre designs; it can prevent the algorithm from exploring certain areas of the search space and create flat fitness landscapes, providing little guidance to the algorithm and making it a “needle in haystack” problem.

The multi-objective approach avoids the challenges of defining the objective by exploring the design trade-offs explicitly. The goal of this optimization process is to obtain multiple solutions situated on a Pareto front. The Pareto front consists of the designs that

are better than any other design in the search space in at least one objective. Such solutions are called non-dominated. For dominated candidates, there exists at least one solution which supersedes it in all objectives. Multi-objective optimization algorithms (MOAs) have high memory requirements because they must keep an archive of non-dominated designs. They also incur a much higher computational cost than the single-objective procedures, as in each iteration, each candidate in the population and/or archive must be compared against each candidate to calculate the dominance relation. The MOAs need to go through a much larger number of candidate solutions to approximate the Pareto front, and the results are often discontinuous/discrete trade-off plots in the objective space that do not translate easily into the design space.

Thus, the single-objective approach is easy to implement and interpret but requires expertise and trial runs to define a suitable objective function; multi-objective algorithms require no assumptions and can find the trade-offs in the objective and design space but at a high computational cost. We can envision a two-stage optimization procedure in which the first stage relies on a single objective determined from TCM. In the second stage, the objectives of interest calculated from full EM analysis can guide the search to fine tune the obtained solutions.

Characteristic modes give accurate, though incomplete information, about the radiating properties of the structure. They do not distinguish between the various objectives but it is not necessary in the initial stages of the search. The modes are fast to compute, and an approximation procedure can further speed up optimization.

### 3.3.1 Computational Challenges

There are multiple computational challenges associated with the estimation of power using TCM. First, the gain in computational time is only achieved if we use small number of modes. A small number of modes (10 to 20 modes for the considered structures) gives good

accuracy for the real power, as the members of the series decrease as  $1/\lambda_i^2$ . The imaginary components decrease much slower - as  $1/\lambda_i$  - so that higher order modes are required. In addition, the estimates of the imaginary power are calculated as the sum of an alternating series and are less reliable, because contributions from partial sums toward the end of the series can be comparable to the contributions of the first terms. Since we can only get an order of magnitude estimate of the imaginary power using a limited number of eigenmodes, in the optimization procedure we cannot directly use the equation of a circle (Equation 3.2) to determine the best feed.

Another source of error is related to our choice of the electromagnetic simulator. Our TCM approach assumes the symmetry of the interaction matrix which guarantees the  $R$  - orthogonality of the eigenvectors. However, NEC2C uses a collocation method for matrix computation, which results in a non-symmetrical matrix and non-orthogonal eigenvectors. This causes errors in the power calculations, especially for larger structures that possess multiple strong modes. In our experiments/optimization runs, we are not looking for exact solutions from TCM; rather we use TCM to guide the algorithm in a search procedure and employ approximation methods to speed up computation. As the inaccuracies due to eigenmode calculation do not seem to mislead the algorithm in its search for optimal design, we assume the errors negligible.

In the following section, we investigate further how the errors affect the ability of the proposed algorithm to steer the optimization procedure.

### 3.3.2 Validation of the Algorithm on Small Test Problems

The goal of this section is to demonstrate the feasibility of our approach to antenna optimization on a set of test problems. We investigate whether: 1) TCM provides accurate estimates of the radiated power; 2) the conditions on power derived in section 3.2 are correlated with the objective in terms of VSWR; 3) TCM approach provides significant

computational advantage as compared to the the full EM simulation of each design; 4) the approximation procedure can further improve the computational time without drastically degrading the accuracy of the power estimates.

We select six benchmark problems to test the developed algorithm and focus on the optimization of square or rectangular plates. A plate represents the basic building block of a larger structure; TCM analysis of rectangular plates is commonly performed in other TCM research; the dimensionality of the optimization problem can be scaled by either increasing the mesh density or the size of the plate. We also consider two real-world problems: integration of an antenna with the skeleton of a mobile phone and modification of a cubic structure. The problems are representative of two application domains - small spacecraft and mobile wireless communications - in which antenna specifications include stringent weight and space constraints.

For each problem, we create 10,000 designs by randomly removing the segments from the full plate structure. The full structure is simulated in NEC2C to obtain the full interaction matrix. For each design, we apply the approximation procedure to identify a viable feed position. The estimates of the real and imaginary power components at the feed are recorded. Then a full MoM analysis of the design is run to obtain exact values of the input resistance and power accepted by the antenna. We also record the time required by the simulator to assemble and invert the interaction matrices. For this same design, we perform the eigenvalue analysis on the exact interaction matrix and record five smallest eigenvalues, the real and imaginary power components and the best feed segment estimated from TCM.

We use the simulation results to characterize correlations between the initial specifications and TCM-based figures of merit, and to develop a suitable objective function in TCM terms. Because we are interested only in the relative values of the estimates to determine the search directions, we use the Spearman rank correlation to illustrate the relations between the variables (real power, VSWR and impedance). Spearman coefficients

can vary between  $-1$  and  $1$ , with the value  $1$  meaning that one variable is a monotonically increasing function of the other,  $-1$  a monotonically decreasing function, and a value of zero indicating no correlation. For  $n$  observations of the variables  $X$  and  $Y$ , Spearman's coefficient is calculated as follows [72]:

$$\rho = 1 - \frac{6 \sum d_i^2}{n(n^2 - 1)}$$

Here  $d_i = X_i - Y_i$  denotes the difference between the ranks of the variables sorted in the ascending order.

The linear correlation coefficient is used instead of the ranking metric to understand the conditions under which the ranks of the variables are poorly correlated. The  $p$ -value describes the significance of the observed correlations; the values close to zero indicate high level of significance.

*Test problem 1 (TP1).* Square plate (Figure 3.4a). We optimize a square plate with the side  $\lambda/2$  in length to obtain a resonant antenna at 1575 MHz. The plate is meshed at  $1/20\lambda$  so that the full structure consists of 220 segments, resulting in a  $220 \times 220$  full interaction matrix. The feed is fixed at one of the corner segments. About 2% of the simulated designs show vswr below 2, making it relatively easy to find a well matched design. The electrical size of the plate is representative of the more complex problems we will approach in later sections. The structure possesses several strong modes at the frequency of interest so that multiple characteristic modes are required to predict its electromagnetic behavior.

*Test problem 2 (TP2).* Finely meshed square plate (Figure 3.4b). To understand how much these results depend on the problem, we reduce the size of the meshing grid by 2 and repeat the experiments. The number of segments in the model increases to 840, and the search space is enlarged to  $2^{780}$ . About 1.5% of the evaluated structures exhibit VSWR below 2, the best structure having the impedance of  $51 - j0.85 \Omega$  and accepted power of 10 mW. The setup is the same as in test case 1, except for each design, the

feed segment is selected based on the approximation of the power values. Among 10,000 random evaluations, 10% have VSWR below two which is 5.7 times more quality designs than in the runs with the fixed feed.

*Test problems 3 and 4 (TP3, TP4).* Design of a small plate GPS antenna (Figure 3.4a and 3.4b). The problems are used to evaluate the TCM-based feed placement. The previous test cases show that power estimates are suitable to compare the quality of the designs of various sizes and configurations relative to each other. Unlike the first two test problems, where the feed is fixed at the first segment of the design, in *TP3 TP4* we use power estimates to predict the best position for the feed. By selecting the appropriate segment for the excitation source, we expect to obtain more higher quality candidates: if this is the case, the algorithm is considered effective at placing the feed. The geometry and meshing of the plates is the same as in problems one and two.

*Test problem 5 (TP5).* Design and integration of a GPS antenna with the phone's endoskeleton (Figure 3.4c). The problem is used to evaluate the TCM-based feed placement. The frame of the phone is represented as a wire model in 3D space. The structure of the phone, the endoskeleton, consists of several slots for the modules of various sizes. Based on TCM analysis, one of these slots is selected for placing a GPS antenna. A plate structure is added on top of the module; on the sides it attaches to the metallic endoskeleton and is assumed to be electrically connected. The unmodified structure is meshed into 1477 wire elements. The additional structure consists of 182 segments, making the size of the search space  $2^{182}$  - comparable to the first test case. As in the previous benchmarks, we remove a random number of segments and record the TCM and full EM descriptors. The search space is further reduced by prohibiting disconnected designs, in which parts of the structure are not linked to its edges by at least one wire segment.

*Test problem 6 (TP6).* Design and Integration of an ISM-band antenna on a CubeSAT (Figure 3.4d). We want to modify a hollow cubic structure so that it acts as an antenna

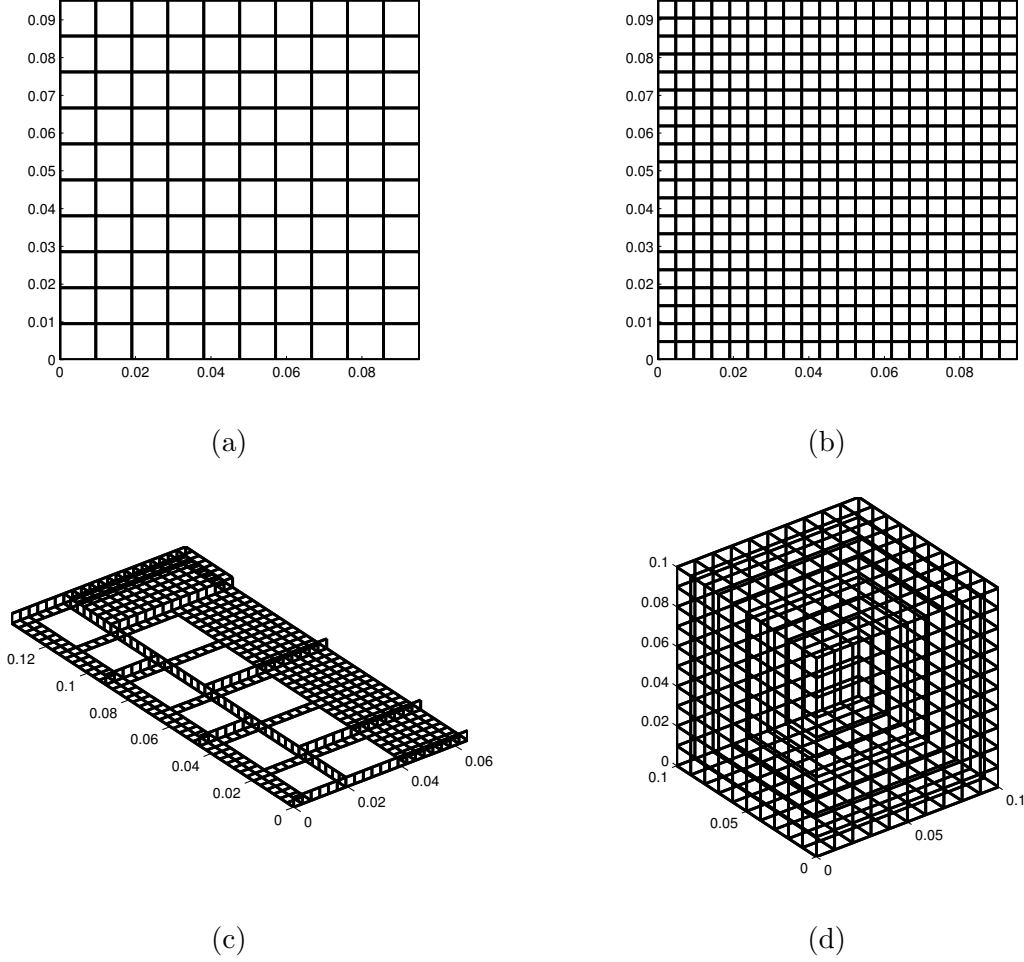


Figure 3.4: Unmodified structures used for testing the TCM objectives: (a) *TP1*: a square plate; (b) *TP2*: a finely meshed square plate; (c) *TP4*: GPS antenna and the endoskeleton; (d) *TP5*: CubeSAT structure.

at 2.45 GHz. The structure has the dimensions of 1u CubeSat, measuring 0.1 m on the side. One face is chosen for optimization. The meshed structure has 1200 elements, and the meshed face consists of 180 segments, similar to the previous test case. Disconnected designs are not allowed. *TP6* differs from the CubeSat optimization problem discussed in section 3.3.6: while optimization objectives are the same in both problems, in section 3.3.6 full cubic structure is allowed to be modified to achieve desired performance.

### 3.3.2.1 Simulation Results

Table 3.2 summarizes the Spearman coefficients for the six test problems. In all test cases, the rank correlation is high between the real power  $P_r^{TCM}$  predicted from the TCM and the power  $P_r$  obtained from the full EM. The correlation approaches one for smaller problems with fixed feed and is slightly degraded for the  $TP3$  through  $TP6$ , for which the feed placement is applied. Overall, the TCM estimates are well correlated with the full MoM results and we can use them in the search procedure with good confidence.

The results for correlations of real power with the power values obtained from the approximate matrix  $P_{app}^{TCM}$  are inconsistent across the problems: the approximation can give acceptable prediction for problems with fixed feed (test problems one and two) but not when the excitation segment is varied ( $TP3$ ,  $TP4$ ,  $TP6$ ). One of the reasons is that the accuracy of the approximate procedure depends on how many neighbors the removed segments possess. A completely random removal tends to create irregular designs, such that many segments “lose” their neighbors and the entries in the initial MoM matrix are no longer representative of the local fields. The accuracy of the power estimates varies from segment to segment within the design as well as between the designs, depending on the number and position of the removed segments. In the first test problems, the approximation is relatively good because the feed is fixed at the corner of the plate and can lose at most one direct neighbor. The feed chosen based on the TCM analysis might lie internally and have up to six neighbors: the variance in the error is increased, which results in poor correlation between the full EM and approximate values.

$TP5$  is a notable exception as the TCM approximations and full EM powers have the ranking coefficient comparable to the fixed-feed problems. One of the possible explanations is that in these problems, a large proportion of designs have relatively poor radiating performance: 80% to 90% of the explored designs radiate less than 1 mW of power at 1 V excitation.

The correlation between the power values using the approximate matrix and the real radiated power is insignificant, showing that the approximate modes cannot correctly rank the candidate designs.

We also measure the ranking correlation between the inverse of the TCM power estimates and the VSWR. According to the lower bound equation derived in section 3.2.1, VSWR is proportional to  $1/P_r$ , when  $P_r$  is below the desired radiated power. In most cases, more than 90% of the randomly generated designs accept less than 10 mW of power. This is reflected in the high value of the ranking coefficient  $\rho(1/P_r^{TCM}, \text{VSWR})$ . This relation is investigated further using the linear correlation coefficient.

Table 3.2: Rank coefficients for the six test problems. First column shows the percent of all designs with VSWR less than 2. Column 3 is the rank coefficient between the power calculated from full EM simulation  $P_r$  and from TCM  $P_r^{TCM}$ . Column 4: rank coefficient for the full EM power and TCM power estimates calculated from approximated impedance matrices. Column 5: rank coefficient for the inverse of the TCM power and VSWR.

Problem	% VSWR < 2	$\rho(P_r, P_r^{TCM})$	$\rho(P_r, P_{app}^{TCM})$	$\rho(1/P_r^{TCM}, \text{VSWR})$
TP1: Small Plate	1.78%	0.98	0.75	0.98
TP2: Large Plate	1.5%	0.98	0.77	0.98
TP3: Small Plate + feed	10.1%	0.89	-0.22	0.87
TP4: Large Plate + feed	11.1%	0.93	-0.18	0.89
TP5: Endo GPS + feed	0.7%	0.84	0.76	0.81
TP6: Cube + feed	6.4%	0.86	-0.22	0.82

*Test problem 1.* We measure how accurately TCM can predict the input resistance of the antenna using the formula derived in 3.2. If we consider all the samples, there is no correlation between the resistance predicted from TCM and the real resistance. This lack of correlation is due to an error in the imaginary power estimates: this error is lower for some designs. To demonstrate this, we reassemble the array of designs and corresponding descriptors in the order of increasing reactance of the antenna. Then we compute the correlation using an increasing number of observations, i.e. first we compute the correlation between resistance and its TCM estimate using two first designs, then three, four, etc. Figure 3.5 shows how the correlation changes as we add more observations with higher

input reactance. The three curves correspond to three relations: a) between the inverse of the exact real power and the resistance ( $1/P_r$  vs.  $R$ ); b) between the inverse of the real power from TCM and the resistance ( $1/P_r^{TCM}$  vs.  $R$ ); and c) between the derived TCM expression  $\frac{P_r}{P_r^2 + P_{im}^2}$  and  $R$ . There is a very strong positive correlation for small reactances especially in the curves a) and b), a sharp transition when the reactance reaches 100 Ohm, and an insignificant negative correlation toward the tail of the curve. The transition and the negative part indicate poor ability of the TCM to predict the ranking of the designs with high reactance: this behavior is expected since in these designs, power is predominantly imaginary, and must be included in the calculations. However, the behavior of curves b) and c) particularly at low reactances indicates that  $P_{im}$  is not improving the accuracy of the estimates - on the contrary, for the designs with low reactance it degrades the correlation by about 20% as compared to the estimates based on the real power alone. Correlation shows that the inverse of  $P_r$  from TCM can differentiate very well between the candidates with low input reactance and can be used in place of the power values from full EM simulation. It should be noted that the “good” candidates with correlations above 0.95 constitute only about 15% of the explored designs.

A high level of correlation is also achieved between the inverse of input resistance and the radiated power (Figure 3.6) for the small ratios of  $Im(Z)/Re(Z)$ . The correlation goes below 90% at 1.5, and 50% correlation is still observed for reactance values five times the resistance. Significant positive correlation accounts for 56% of the evaluated candidate designs.

*Test problem 2.* The obtained results are very similar to the results of the smaller plate problem: the correlation between the exact power values and TCM estimates is very high at 97%. The correlation between the resistance and the radiated power of the samples (in the order of increasing  $Im(Z)/Re(Z)$ ) exceeds 50% for approximately 40% of the tested solutions and becomes insignificant for the ratios above 6. The accuracy of TCM predictions

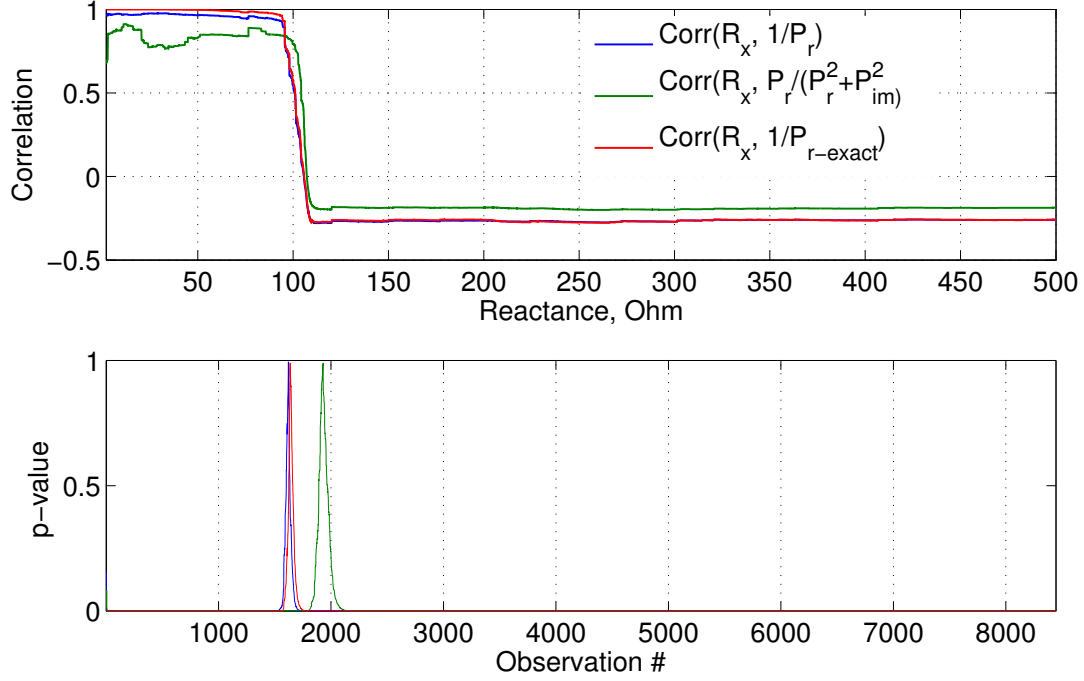


Figure 3.5: TP1: Correlation and its significance for the observations in the order of increasing reactance.

using the imaginary power is much lower than in the first test problem, showing significant correlation with the resistances from full EM only for 4% of the candidate solutions.

Finally, we use this data to illustrate how radiated power is related to the VSWR: from Figure 3.7 the inverse of the power is significantly correlated with VSWR only for poorly matched antennas with VSWRs higher than four. For VSWRs below two, there is no linear correlation between the variables, and the real power alone gives no information about matching. Overall, increase in the radiated power indicates an improvement in matching and could be applied as a fitness function in the initial stages of the search. To distinguish between the good designs, the reactive component and the matched impedance must be considered. However, we cannot rely on the estimates of the reactive power because their accuracy is limited.

*Test problem 3.* Design of a small plate GPS antenna. Among 10,000 random evalu-

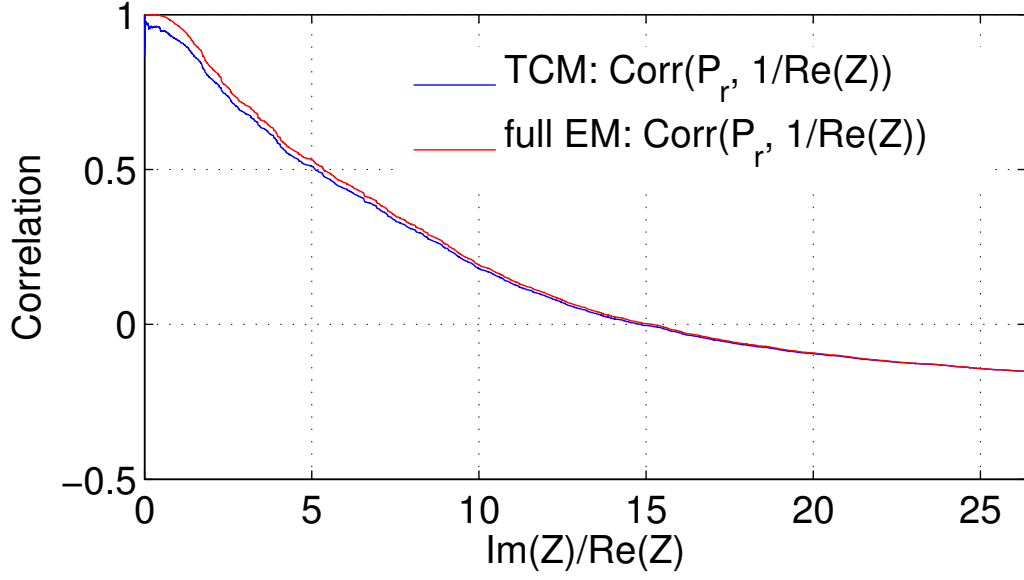


Figure 3.6: TP1: Correlation for the observations in the order of increasing ratio of imaginary and real parts of the impedance.

ations, 10% have  $VSWR$  below two which is 5.7 times more quality designs than in the runs with the fixed feed. The feed placement algorithm works quite well - even though the correlation between the variables in this experiment is significantly reduced. Thus, the correlation between the power and its TCM estimates lessens to 0.83. Due to a much larger proportion of poor designs (50%), whose radiated power is on the order of  $10^{-6}$  W, the numerical errors significantly affect the calculation accuracy; excluding the results with  $VSWR$  above 100, the correlation is 0.95. The correlation between the inverse of the power and the input resistance also goes down. This behavior is expected and corroborates the observation from previous experiments that TCM predictions cannot make the fine distinction between good quality candidates. As the algorithm tends to explore better solutions with comparable resistances around the desired value, their ranking grows more dependent on the reactive power component.

The correlation results are summarized in Table 3.3. For all problems, the  $VSWR$  and inverse of TCM power are linearly correlated for the designs with  $VSWR > 2$ , especially

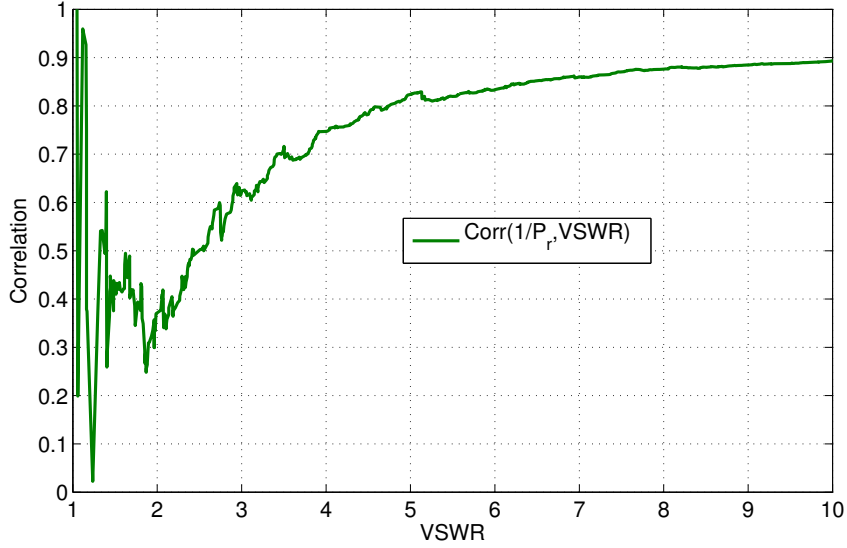


Figure 3.7: Correlation between the inverse of the real power and VSWR. The independent axis shows how the correlation changes as samples with increasing VSWR are added to calculate the correlation.

Table 3.3: Correlation between various TCM objectives and VSWR on six test problems. Rows 2 through 6 show the correlation coefficient between various functions of radiated power  $P_r$  and VSWR.  $\text{VSWR}_{<2}$  denotes all designs with VSWR below 2.  $R_{des}$  is the desired input impedance to be matched. The correlation coefficient is not shown, where the confidence in the calculated value is low. Values in parentheses show correlation for truncated data, from which the designs with  $\text{VSWRs} > 100$  are excluded.

Correlation coefficient	TP1	TP2	TP3	TP4	TP5	TP6
$(1/P_r, \text{VSWR}_{<2})$	0.58	0.53	0.55	0.48	no	0.45
$(1/P_r, \text{VSWR}_{>2})$	0.99	0.83(0.95)	0.99	0.91(0.97)	0.53(0.94)	0.99
$(\text{abs}(P_r - 0.5/R_{des}), \text{VSWR}_{<2})$	0.69	0.73	0.65	0.66	no	0.58
$(\text{abs}(P_r - 0.5/R_{des}), \text{VSWR}_{>2})$	0.49	0.17	0.28	0.20	no	0.38

when the numerical error is reduced by excluding the designs with microscale power levels (values in brackets). The VSWRs of matched designs (VSWRs below two) are better correlated with the function  $f = \text{abs}(P_r - 1/(2R_{des}))$ , where  $R_{des}$  is the resistance of the excitation source.

### 3.3.3 Generation of New Designs

We compare how the way we generate designs affects the exploration of the search space. In the previous simulations, the new designs were generated by removing randomly a number of segments from the interior of the plates. We want to compare if on average, we can achieve better designs by constraining the algorithm to create only contingent slots of rectangular shapes. In this experiment, the same structure is used; however candidate designs are created by randomly selecting four nodes of the plate. Each pair of nodes defines the corners of a rectangular slot.

Among the 10,000 generated designs, only 17 had VSWR less than three. Obviously, regular slots do not increase the probability of generating a good design: yet, the regularity of the resulting structures provides for much better correlation between the power inverse and the VSWR, which exceeds 96% for all designs.

Also, the error between the estimates of power using approximate and exact MoM matrix is significantly reduced: overall, the values show 90% correlation. However, the error for well-matched candidates ( $\text{VSWR} < 3$ ) is still very poor, and the approximate approach fails to predict the correct ranking of the top found designs. This can be explained by the fact, that the accuracy of the approximate procedure depends on how many neighbors the removed segments have. A completely random removal - as in the first experiment - tends to create irregular designs, such that many segments “lose” their neighbors and the entries in the initial MoM matrix are no longer representative of the local fields. With regular slots, only segments on the boundary of the slot are affected (each losing at most two neighbors out of six) and the error in matrix entries is acceptable, resulting in the reasonable estimates of the power.

Analyzing the obtained designs, we notice that good antennas possess feeds with two neighbors, i.e. the wire with the excitation source connects to only two wires. The neighboring segment parallel to the feed segment and immediately adjacent and perpendicular

to it are absent in 70% of good designs. This explains why the approximation procedure always fails to rank the well matched designs.

### 3.3.4 Computational Time

In this section, we investigate how the computational time scales with the size of the meshed structure and what computational advantage we can expect from using the TCM versus the full EM simulation. We compare the runtime of three MATLAB procedures:

1. TCM-based analysis (20 eigenmodes): a generalized eigenvalue problem is solved using MATLAB routine  $eigs(R, X, n, 'sm')$ . The power values are estimated for all segments of the structure.
2. TCM-based analysis (40 eigenmodes): a generalized eigenvalue problem is solved using MATLAB routine  $eigs(R, X, n, 'sm')$ . The power values are estimated for all segments of the structure.
3. Solution of the MoM equations using the MATLAB inverse function  $Z_{inv} = [Z]^{-1} = inv(Z)$ : matrix is inverted once at the beginning of the run and stored; it is then used to calculate the current and the impedance at the excitation segment. The equation  $I = Z_{inv}V$  has to be solved for each new feed segment.

All procedures operate on the same matrices. The interaction matrices for the structures of different sizes are assembled in NEC2C and represent antennas discussed above. Figure 3.8 shows the runtimes for each procedure performed on a 2.53 GHz Intel dual core MacBookPro with 4 GB RAM. Each data point in the figure is the mean of hundred computations. The three curves are plotted on a semilog scale and represent the three approaches. The computational complexity of the three algorithms is evaluated elsewhere to be  $O(n^3)$  where  $n$  is the dimension of the matrix, and we can see this trend in all three curves. However, the rate of increase of the TCM curves is significantly lower, because the TCM approach requires a limited number of modes (full eigenanalysis can produce up to

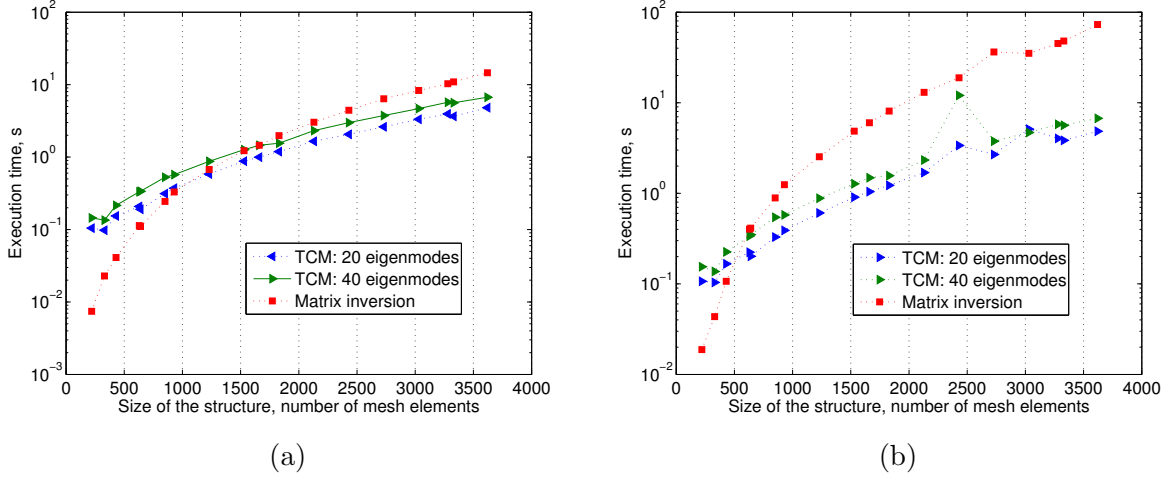


Figure 3.8: Execution time of full EM and TCM-based procedures: (a) Time to compute the power at one feed position; (b) Time to compute the power at all feed positions.

$n - 1$  eigenmodes) to compute the power estimates.

Because the TCM-based approach evaluates all segments in one run, its computational advantage becomes significant as the number of tested feed positions increases. To show how this affects the cross-over point, we investigate the two limiting cases - the worst and best case scenarios for the TCM. In the first one, only one evaluation is required (Figure 3.8a). In the second approach, all segments must be evaluated to obtain impedance values (Figure 3.8b).

From Figure 3.8a, the TCM using 20 modes starts to outperform the full MoM procedure for structures with 1000 elements or more even when one feed position is considered. For structures larger than 3000, the TCM procedure runs three times faster. Depending on the number of tested feed positions, the cross-over point changes: as the number is increased, the cross-over shifts to lower  $n$  hitting a limit around 500 segments (Figure 3.8b).

It should be noted that the speed up is achieved at the cost of accuracy. As shown in previous sections, due to the numerical errors TCM-based power estimates can give a rough approximation for the matching at the feed segment, while the other two procedures

provide the impedance with accuracy limited primarily by the fidelity of the EM model.

To summarize, maximizing the power accepted by the antenna leads to more efficient and better matched radiators. We have demonstrated that for the considered design problems, power values are correlated with the VSWR - particularly for the designs of intermediate quality.

TCM provides estimates of the radiated power that are strongly correlated with the power values from full EM calculation and can be used for fitness assignment in an optimization procedure. The use of TCM estimates speeds up fitness evaluation for larger and finer meshed structures. In addition, TCM selects the most promising feed position for each structure, thus improving the proportion of good designs among the explored candidates. Yet, the estimates are not accurate enough to rank the quality of the best matched designs, and full EM optimization should be run to fine tune them. The eigenanalysis performed on the approximate interaction matrix cannot provide useful information for the optimization procedure.

### 3.3.5 Optimization of the Endoskeleton

The endoskeleton chassis can be used to enhance the performance of miniaturized mobile antennas. The wire antenna we investigated in the previous section represented a part of the endoskeleton. In the real design, it is electrically connected to a large bottom plate.

Figure 3.9 shows the mesh grid model of the endoskeleton and the first five modes as the function of frequency. The first five eigenmodes are all significant for the radiation, as the magnitudes of the eigenvalues are less than 5.

The endoskeleton is a relatively large structure and produces multiple radiating modes in the band of interest. The interplay of these modes results in the large reactive component of the power: the excitation by a coaxial probe at the point with the highest real power does not result in a good performance as the antenna's impedance is dominated by the

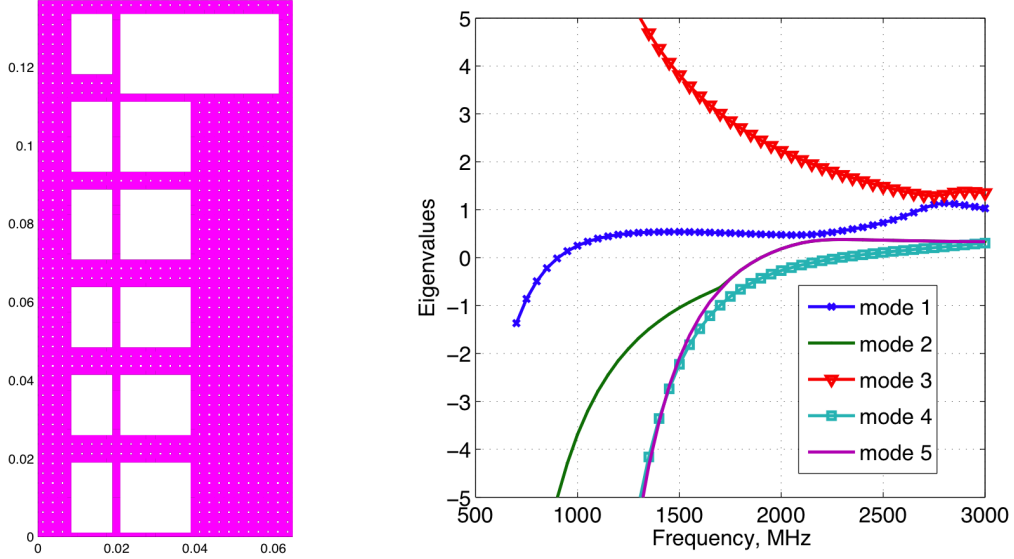


Figure 3.9: (a) Mesh grid model of the endoskeleton; (b) Characteristic modes of the endoskeleton.

inductive component. We need to modify the structure - by introducing slots or adding material - so that the desired radiating modes are enhanced and inductive and capacitive effects are balanced out, creating the resonance.

The capacitive effect can be created by adding a metallic plate on top of the module. We define a metallic patch in the plane parallel to the endo-structure at the height of 0.5 mm and apply a greedy hill climber to optimize its shape. The additional structure is modeled as a wire grid, whose elements are aligned with the elements on the bottom. This new grid is represented as a binary vector, in which 1 denotes the presence of the mesh element, while 0 indicates its absence in the design.

We analyze the structure in the GPS band (1575 MHz), at which it is challenging to design an antenna fitting into a single phone module. From the power distribution graphs, the third mode is the highest contributor to the radiated power. The eigencurrent of this mode peaks at the upper edge of the endoskeleton and therefore, we choose this area for optimization.

We apply the greedy hill climber, implemented in MATLAB, to optimize the shape of

the additional structure. The interaction matrix is evaluated in the external EM simulator NEC2C and imported into MATLAB for eigenvalue analysis. To speed up fitness evaluation, we apply an approximation procedure [38]: NEC2C is not run after each modification of the structure (e.g., in each iteration). Initially we obtain an interaction matrix with all the segments present. During optimization, when removing an element, we remove the corresponding rows and columns in the initial matrix. The approximate matrix is used to find the eigenvalues of the new structure and calculate the objective function. The error is tolerable as long as the changes in the structure and the changes in the eigenvalues due to the modification are small. Once we see a big relative improvement (or no improvement for many iterations), we fix the changes and rerun the full EM simulation to obtain the exact solution. Then the search continues with the exact matrix as a starting point. On average, the full EM analysis is run once every hundred iterations. The minimization objective/fitness function is based on the conditions derived in section 2.2:  $F = \text{abs}(P_r - 1/(2R_x))$ . The goal is to increase the real power, keeping the reactive component small.

The search procedure starts with all segments present. In each iteration, a subset of segments is removed to generate a new design. The hill climber accepts a change only if it improves the objective function. The search terminates after 400 generations or when no improvement occurs for several generations. After the algorithm terminates, the power analysis is applied to find the optimal feed position and the full EM simulation is run to characterize input impedance and radiation pattern of the structure.

One of the optimized designs is shown in Figure 3.10a - 3.10b : the patch has several thin slots and is electrically connected to the endoskeleton on three sides; feed location is highlighted in red. The structure becomes resonant around 1.575 GHz, achieving a VSWR of 1.4 (Figure 3.10d). Its main radiation beam is directed away from the plane of the antenna and has a relatively broad beamwidth of 60 degrees (Figure 3.10c).

Figure 3.11a - 3.11b shows another design obtained by the hill climber. In this run, the

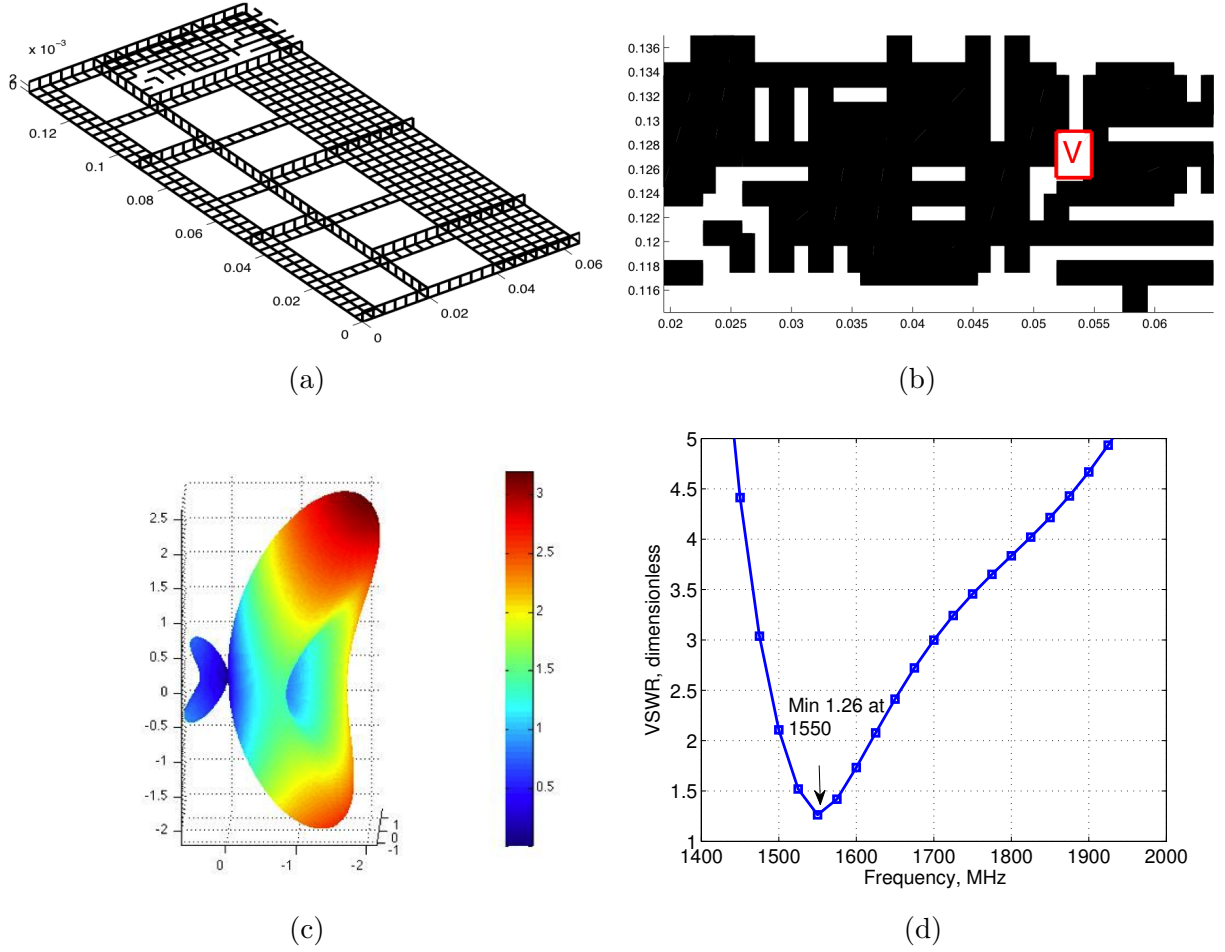


Figure 3.10: Design 1: Endoskeleton modified to radiate at 1575 MHz. (a) Endoskeleton with an optimized patch; (b) Patch geometry; (c) Radiation pattern at 1575 MHz (dimensionless); (d) VSWR as a function of frequency.

algorithm started by removing all additional elements and created new designs by adding the segments. The resulting structure is more compact but has performance characteristics similar to Design 1 (Figure 3.11c - 3.11d).

### 3.3.6 Feed Placement and Optimization of the Cubic Structure

Another application area is the integration of an antenna with a 1u CubeSat. The simplified model of the CubeSat is a cubic grid model measuring 0.1 m on each side. The objectives are the same as in problem *TP6* discussed in section 3.3.2. However, in this problem full

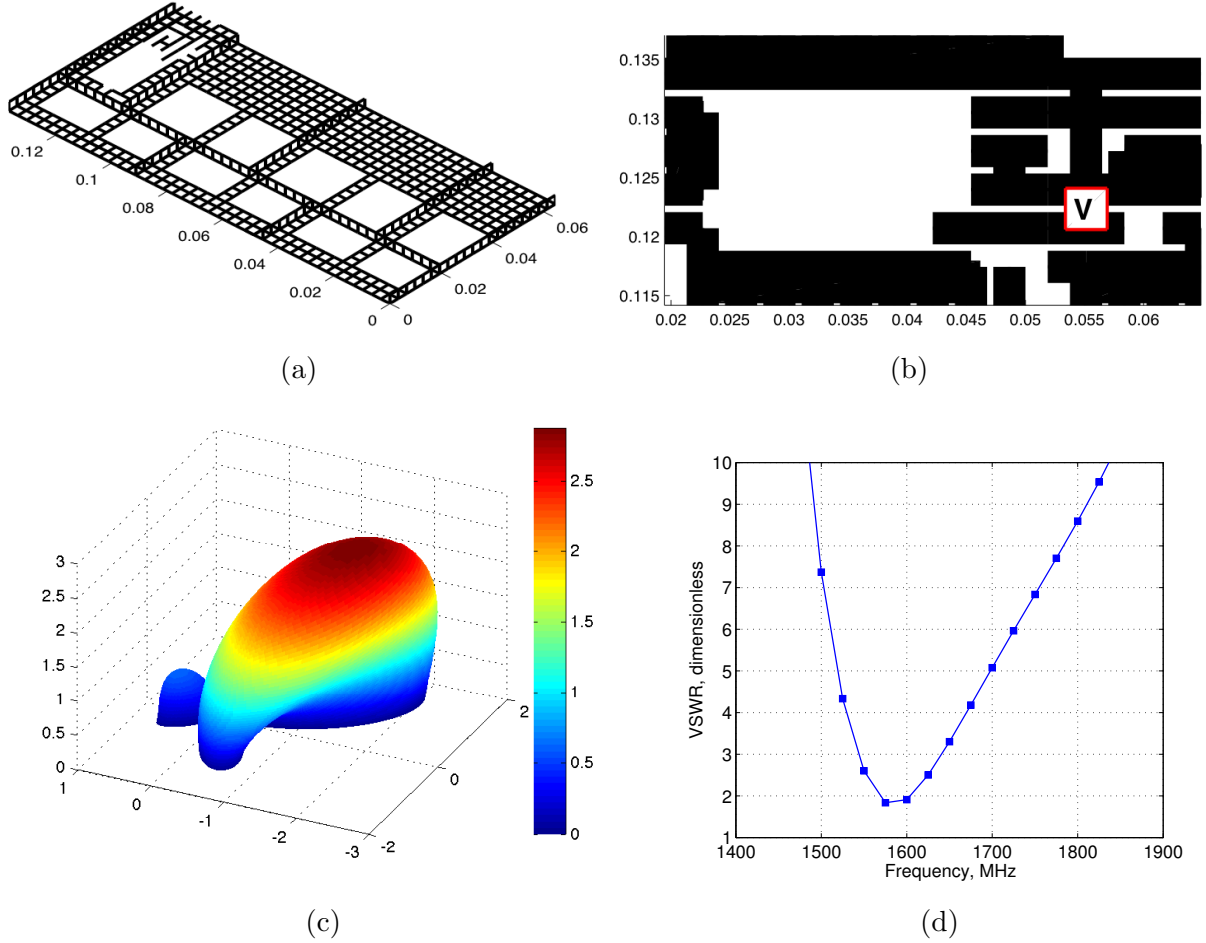


Figure 3.11: Design 2: Endoskeleton modified to radiate at 1575 MHz. (a) Endoskeleton with an optimized patch; (b) Patch geometry; (c) Radiation pattern at 1575 MHz (dimensionless). Due to symmetry with respect to  $XY$  plane, only the top part of the pattern is shown; (d) VSWR as a function of frequency.

cubic structure is chosen for optimization, rather than just one face of a cube as in *TP6*. We apply the same optimization routine as in section 3.3.5 to modify the structure at 2.45 GHz. The algorithm gives a good result within 100 iterations, performing only two calls to the full EM simulation. The obtained design and the VSWR plot is shown in Figure 3.12. The optimized cube structure shows a broad impedance bandwidth with VSWR values below 3 between 2 and 3 GHz. Note the VSWR peaks at two frequencies around 2.1 and 2.55 GHz. The discontinuities occur due to the numerical instability in the MoM simulation, which is associated with the existence of internally resonant waveguide modes.

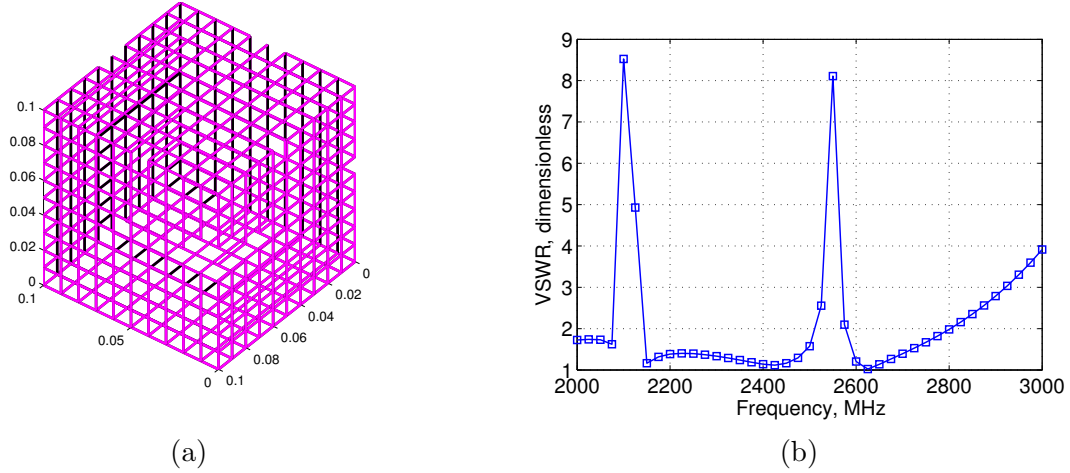


Figure 3.12: Cube structure modified to radiate at 2.45 GHz: (a) Optimized cube geometry; (b) VSWR as a function of frequency for the optimized design.

### 3.4 Summary

In this section, we explored the advantages and limitations of the TCM for guiding the antenna optimization. We derived an algorithm for placing the excitation source on the structure and verified its performance on a number of representative antennas. Maximizing the radiated power is a suitable objective in the initial stages of the optimization procedure. The power is strongly correlated with the inverse of the antenna's input resistance and is a good measure of how well matched the antenna is and how much power is transformed into the electromagnetic waves. Finally, we successfully applied the proposed algorithm to two real-world problems: integration of a GPS antenna with the chassis of the mobile phone and integration of an antenna with the metallic CubeSat structure.

# Chapter 4

## Multi-objective Algorithms for Coupled Optimization

### 4.1 Coupled Electromagnetic and Mechanical Optimization

The disciplines of mechanical and electromagnetic (EM) optimization have developed along different paths. In the mechanical domain, classical optimization methods dominate. Convex formulations of the structural optimization problems exist, which can be efficiently solved using derived optimality criteria or mathematical programming [74]. Continuous topology optimization with thousands of variables has been demonstrated [5], [6], [4]. In contrast, optimization in the EM domain is usually performed using stochastic population-based algorithms [39], [13], [41], [49], [38]. Because of the inherent complexity and non-linearity of the EM landscapes, research in the field of antenna optimization has focused on defining suitable algorithmic parameters and representations rather than rigorous mathematical formulations of the optimization problems.

For antenna design and optimization, the coupling between the EM and mechanical domains is a one-way coupling: while the EM performance strongly depends on the changes in shape due to mechanical impact, structural properties are not affected by the EM. Depending on the ultimate application, we can distinguish between two scenarios: in one case, the dynamical interactions between the domains are significant such that the EM performance depends on the results of the mechanical analysis. Both objectives are functions of the design and state variables. An example would be a dipole antenna whose main beam

is shifted when the antenna is deflected under load. If we wanted to find a sequence of applied loads that would steer the radiation beam in certain directions by deflecting the dipole, then we will need to run both mechanical and EM analysis to evaluate each of the candidate solution vectors. Another example is the aberration in the focus of the reflector when its surface is deformed because of the thermal gradients or snow. In some sensing applications, strong interactions between the domains are desired: for example, when the changes in an antenna’s performance are used to measure structural deformations or when mechanical reconfiguration is used to obtain specific EM performance. In such cases, the evaluation of the EM objective requires the output of the mechanical analysis, and full decoupling of the optimization procedure between the domains is not possible.

In the second case, the EM properties are independent of the mechanical performance unless there is catastrophic failure resulting in the degradation or loss of communication. For example, an antenna integrated with the spacecraft can be subjected to significant vibrational loads during the launch and can also be mechanically damaged by space junk/meteorites when in orbit. In this case, the domains are linked only through the design variables. The antenna can be optimized for EM performance, and its structure can be reinforced to be mechanically robust.

In this chapter, we focus on the second problem type, in which EM and mechanical domains are linked statically by the design variables. In the mechanical domain, we consider linear elastic and isotropic materials. Objectives in structural optimization are continuous functions of the design variables and lend themselves well to solution by gradient-based methods. Calculation of the mechanical properties is significantly faster than simulation of the EM response. This is accounted for in the design of the multi-objective optimization engine in section 4.3.

In this chapter, we investigate how to leverage the domain-specific methods and solution representations in coupled optimization of antennas. We develop a multi-objective optimization framework based on the local search in each domain. In this procedure, the local optima in each objective are modified to create a new population of candidate designs. Local optimization becomes the primary way of exploring and exploiting the search space. We evaluate the proposed technique on a number of benchmark problems and compare its performance to the performance of leading MOEAs.

We start the chapter by illustrating the coupling for a load-bearing dipole example. In section 4.2, we define the optimization benchmarks with objectives and constraints in both domains and plot the corresponding fitness landscapes and Pareto fronts as a function of

design variables. In section 4.3, we describe the implementation of the proposed multi-objective algorithm with local search (MOLS). In section 4.4, we present and discuss the results of extensive tests of MOAs on benchmark problems.

## 4.2 Benchmark Problems and Their Solutions

Table 4.1 summarizes the properties of the four benchmarks problems investigated in this section. The size of the search space is calculated from the box constraints on the design variables assuming precision of  $10^{-6}$  in each variable. Benchmarks B1 through B4 are presented in sections 4.2.2, 4.2.3, 4.2.4, and 4.2.5 correspondingly.

Table 4.1: Characteristics for four benchmarks B1 - B4.

	Mechanical	EM	Variables	Objectives	Constraints	Search space
B1	cantilever beam	monopole over ground	1	displacement VSWR	box	11,633
B2	two-bar truss	monopole over ground	2	displacement mass gain inverse	box stress	$2.48 \times 10^7$
B3	two-bar truss	monopole over ground	3	displacement mass gain inverse	box stress	$5.82 \times 10^{10}$
B4	ten-bar truss	radiating structure	10	compliance mass first eigenmode	box stress statical determinancy	$8.69 \times 10^{25}$

### 4.2.1 Load-bearing Dipole Antenna

We select the deflection of a dipole antenna under load as a benchmark because it combines the basic problem characteristics in both domains. In the mechanical domain, the antenna represents a cantilever beam subjected to uniform or point loading. In the EM domain, it is a dipole placed over ground and fed at its base with a voltage source.

First, let us illustrate how the pattern of the horizontal antenna is affected by the deformation. Figure 4.1 shows the representation of the problem in the mechanical and EM domains. From the structural perspective, the antenna is represented as a cantilever beam fixed at its end. The uniform loading is applied along the length of the antenna, resulting in the deflection of the structure. With the assumption of a slender beam (i.e. the radius of the beam cross-section is less than 1/10 of its length), the deformation  $z$  can

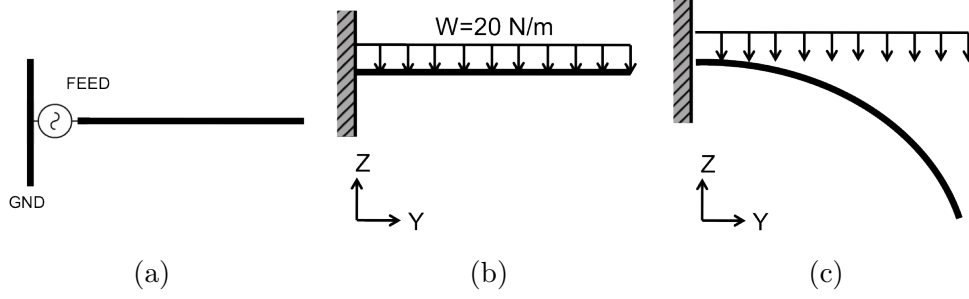


Figure 4.1: Monopole antenna under load: (a) definition of the problem in the EM domain, monopole over infinite ground; (b) in the mechanical domain the antenna is represented as a uniformly loaded cantilever beam; (c) beam deflected under load.

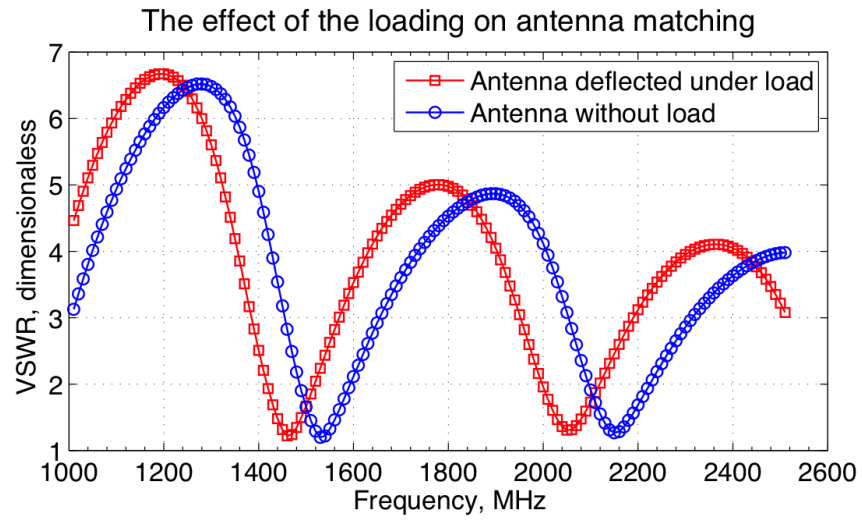
be expressed analytically as a function of position  $y$  on the beam:

$$z(y) = -\frac{w}{24EI}(y^4 - 4Ly^3 + 6L^2y^2)$$

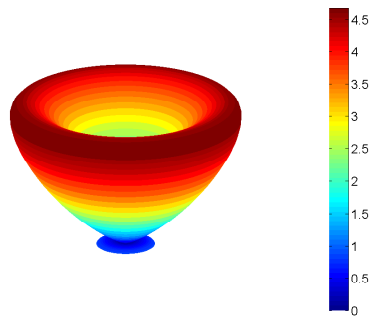
where  $z$  is the vertical deflection,  $L$  is the total length of the undeflected beam,  $E$  is the Young's modulus, and  $I$  is the area moment of inertia. For the circular cross-section with radius  $r$ ,  $I_y = \pi r^4/4$  [20]. In the EM domain, the beam is a monopole antenna placed over an infinite ground plane. We consider an antenna made of ABS plastic and covered by a perfectly conductive layer. The plastic material is lighter and less rigid, and as a result larger deformations occur before the material breaks. We compare the VSWR and the change in the radiation patterns of the undeflected and deflected antenna. The performance is summarized in Figure 4.2.

The change in VSWR can be completely explained by the elongation of the antenna under the load. As the material bends, the effective length of the dipole is increased, shifting the resonance (VSWR minima) to lower frequencies. Because of the bend, the main radiation beam splits into multiple lobes, and the symmetry of the pattern is destroyed. Main beam in the plane of deflection is depressed, with the gain decreasing from 4.5 to about 2.5. Power flow in the direction of the deflection and parallel to the ground increases by a factor of 4 (Figure 4.2b and 4.2c).

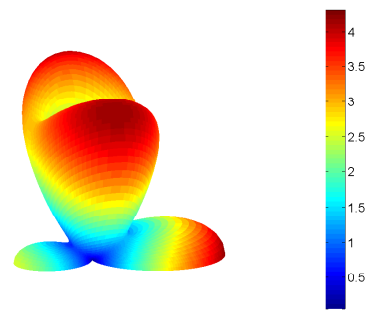
Suppose we want to optimize the matching of the monopole and reduce the effect of the loading on its performance. In other words, we want to find the length and radius of the monopole such that the maximum deflection and VSWR are minimized. There is an additional mechanical constraint on the maximum bending stress  $\sigma_{max}$  at the support: it should not exceed the yield stress of the material so that the deformation does not



(a)



(b)



(c)

Figure 4.2: Change in EM Performance due to the uniform loading: (a) VSWR of the deflected and undeflected monopole antenna. Radiation pattern of the (b) undeflected and (c) deflected antenna.

become irreversible. The deflection is proportional to the ratio of  $(L/r)^4$ . The VSWR is changing periodically as a function of  $L/\lambda$ , with the resonances occurring in approximately  $\lambda/2$  intervals. The increase in radius tends to broaden the VSWR minima, decreasing the effects of the deformation; however VSWR is much less sensitive to the changes in radius than to the changes in length.

The optimization problem is:

$$\begin{aligned}
& \text{minimize} && z_{max}(L, r) \\
& && VSWR(L, r) \\
& \text{subject to} && \sigma_{max} < \sigma_{yield} \\
& && L_{min} \leq L \leq L_{max} \\
& && r_{min} \leq r \leq r_{max}
\end{aligned}$$

where

$$\begin{aligned}
z_{max} &= \frac{wL^4}{8EI} = \frac{w}{2E\pi} \left(\frac{L}{r}\right)^4 \\
\sigma_{max} &= \frac{wLr}{2I_y} = \frac{2w}{\pi} \frac{L}{r^3}
\end{aligned}$$

The mechanical objective and constraints are convex functions of the design variables. For  $r > 0$  and  $L > 0$ , both the deflection and the stress are monotonically increasing functions of the variables  $x_1 = 1/r$  and  $x_2 = L$ . The optimal solution to the mechanical problem is obtained at  $(L_{min}, r_{max})$ , i.e. for the shortest and thickest beam which minimizes both the deformation and the stress. The EM objective is the one that determines the size of the Pareto front which consists of the designs and resultant objective values close to the constraint boundaries and near the minima of the VSWR.

#### 4.2.2 Benchmark B1: Cantilever Beam Optimization

To illustrate this, we consider a fixed diameter beam and plot the values of maximal deformation and VSWR as a function of  $L$ . Figure 4.3 shows the two objectives as a function of the beam's length (blue points) and the resultant Pareto optimal points highlighted in green.

This plot underscores several properties of the problem: first, the Pareto optimal set is discontinuous in the design space. It consists of two distinct regions: one near the bound-

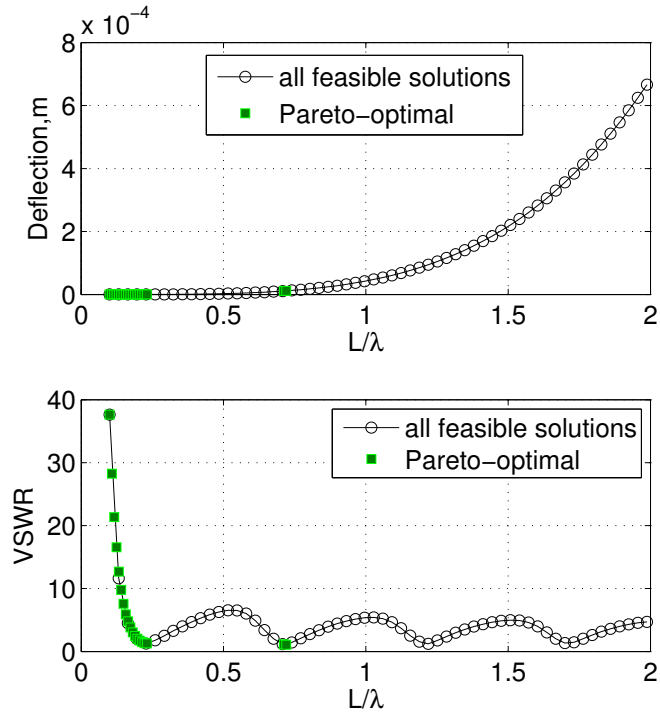


Figure 4.3: B1: Illustration of the Pareto optimal solutions for the cantilever beam problem: VSWR as a function of beam's length  $L$  normalized to the wavelength (bottom). Maximal deflection of the beam (top).

ary starting with  $L_{min} = 0.1\lambda$  that contains solutions non-dominated in the mechanical objectives; the second region - near the second VSWR minimum - is dominated by the first set of designs in deflection but is non-dominated by it in VSWR. While locating the first region of non-dominated solutions should be easy for any multi-objective algorithm, finding the two individual champions toward the middle of the search space represents a challenge. The candidate solutions that might be evolved into the desired Pareto designs in the second region are strongly dominated by multiple solutions with smaller lengths. As a result, the algorithm tends to preserve and exploit the candidates at the lower boundary of the search space, eliminating the regions with the best VSWR.

Another observation is that in this problem, running domain optimizers independently of each other and identifying local optima in both of them should yield a good approximation of the Pareto front. In general, it is desirable to decouple the optimization process in separate domains as much as possible, so that each area could benefit from its most efficient techniques, algorithm parameters and solution representations. A synchronization engine should monitor the search progress in each domain, synchronize the candidate populations and compute the dominance relations in some suitable intervals of time. Such distributed structure is also very amenable to parallelization. If fitness evaluation is much faster in a particular domain, then it should not wait for other simulators to finish before processing the next batch of candidate solutions. The search in each separate domain should ensure diversity of the population: the goal is not to obtain a globally optimal design but rather to identify many local optima in various areas of the design space.

### 4.2.3 Benchmark B2: Geometry Optimization of a Two-bar Truss

The two-bar truss structure is one of the mechanical problems that has been widely used as a benchmark in structural multicriteria optimization (Figure 4.4). In the mechanical domain, this two-dimensional structure is optimized in two objectives: minimizing the weight and minimizing the displacement at node 3 under the specific load conditions [18], [12], [30], [22]. Both objectives can be expressed as a function of the applied load, material properties and three design variables (width, height, and bar radius).

Here we extend this problem into the EM domain. The two-bar truss represents a horizontal monopole antenna above the infinite ground plane fed at its end with a gap voltage source. The antenna should resonate at 2.45 GHz, providing the best impedance match to  $50 \Omega$  and high gain in the vertical direction at the desired frequency. The third

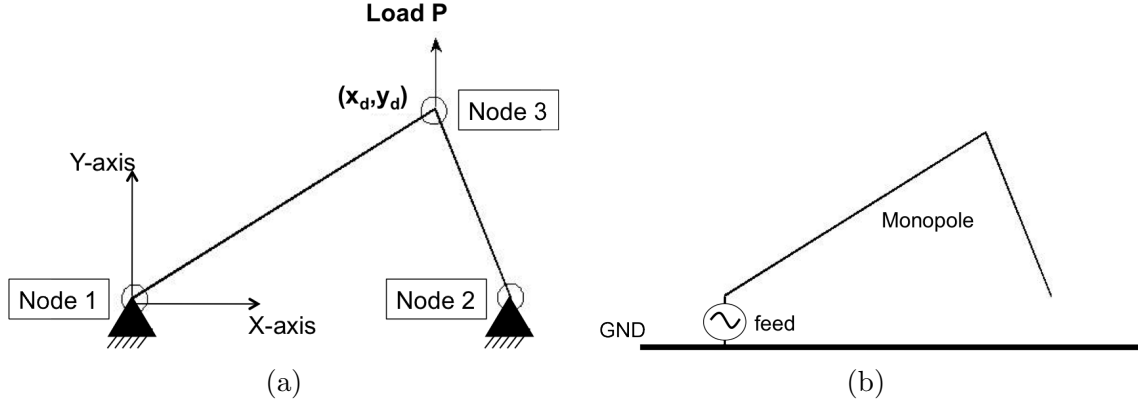


Figure 4.4: B2: Problem definition in the mechanical and EM domains. (a) Truss loaded at the central node. (b) Corresponding antenna problem, i.e. monopole over ground.

objective, maximization of the realized gain, is added to the initial optimization problem. Unlike the mechanical domain, this objective must be evaluated numerically, using NEC2C, which incurs significant computational cost.

The first variant of the two-bar truss problem can be used to test algorithm's ability to optimize the topology of the structure. In this problem, the design variables are the coordinates of the central node  $(x_d, y_d)$ . The position of the corner nodes (nodes 1 and 2 in Figure 4.4), the radius of the bars and the height above ground are fixed during the optimization. The coordinates are varied between 0 and  $\lambda/2$ . The objectives in the mechanical domain are displacement at the central node and the mass of the truss. In the EM domain, the objective is to maximize the realized gain ( $RG$ ) along the  $y$ -axis, i.e., vertically. To formulate the problem as a minimization problem, the EM objective is calculated as the inverse of the gain:

$$\begin{aligned}
 &\text{minimize} && f_1 = \text{displacement}(x_d, y_d) \\
 &&& f_2 = \text{mass}(x_d, y_d) \\
 &&& f_3 = 1/RG(x_d, y_d) \\
 &\text{subject to} && \sigma_{max} < \sigma_{all} \\
 &&& 0 < x_d \leq \lambda/2 \\
 &&& 0 < y_d \leq \lambda/2
 \end{aligned}$$

Figure 4.5a–4.5c depicts the search space of the test problem: displacement, mass and realized gain are shown as a function of the coordinates. Figure 4.5d shows the Pareto-

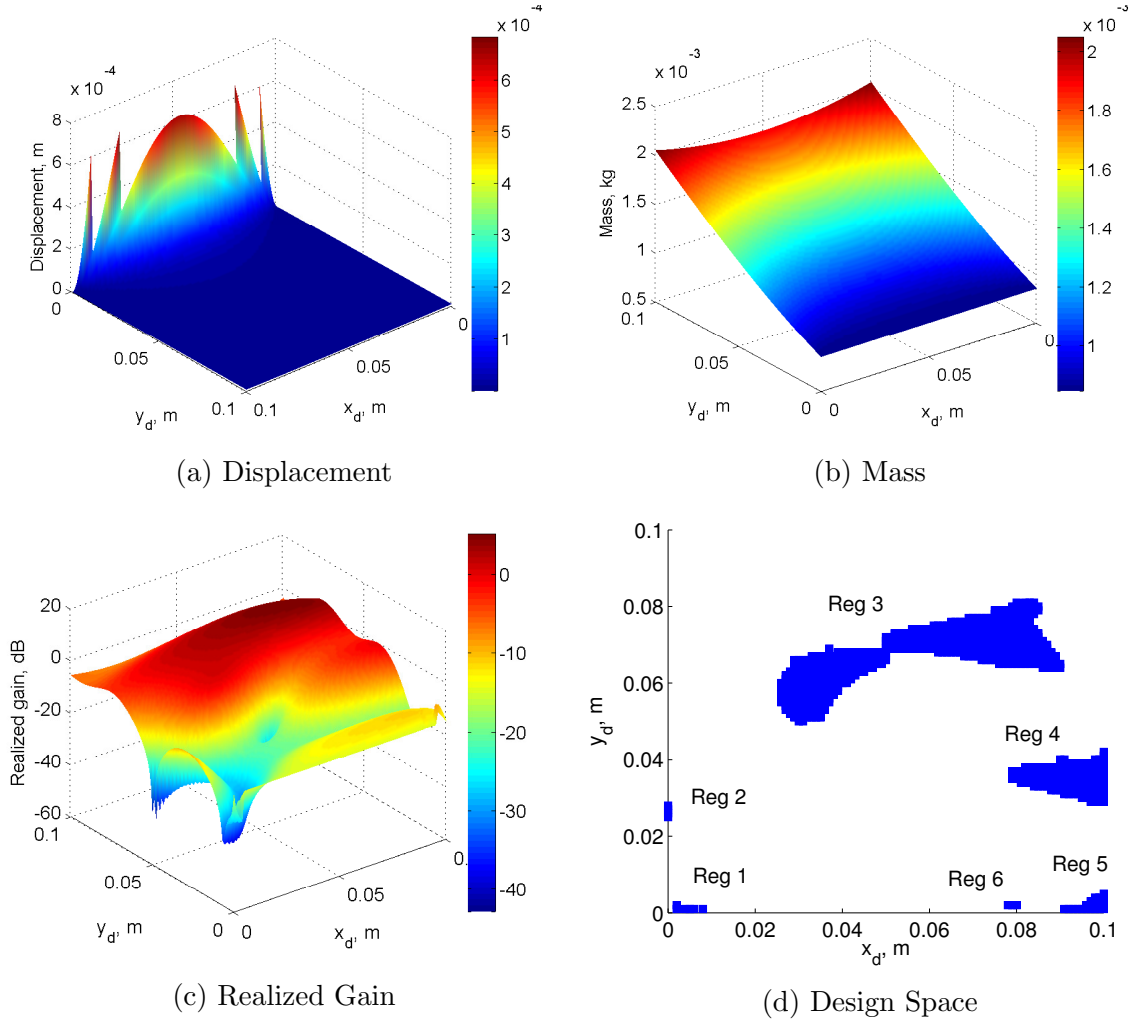


Figure 4.5: B2: The search space and the Pareto optimal designs for the various truss topologies. The three objectives are shown as a function of the design variables, the central node's coordinates  $(x_d, y_d)$ : (a) displacement at the central node, (b) mass of the truss; (c) realized gain in dB to be maximized. (d) Pareto-optimal points in the decision space: the set consists of six separate regions numbered clockwise as *Reg1* – *Reg6*.

optimal designs. There are several distinct areas of non-dominated solutions. The two designs with the smallest  $y_d$  values correspond to the local minima of mass and displacement functions, which occur on the boundaries of the search space; antennas with high  $(x_d, y_d)$  are located near the global maximum of the gain function. The designs in the middle are dominated by the top designs in gain but not in mass or displacement; on the other hand, the bottom designs dominate the solutions in the middle in mass and displacement but show a lower gain.

The fitness landscapes in both mechanical objectives are relatively flat: mass changes

rapidly as a function of  $x$  but slowly along  $y$ , while the displacement function has small gradient along both directions. Mass function reaches its minimum at the point  $(0.005, 0.005)$  but since this design does not satisfy the stress constraints, it is not included in the Pareto set.

Several aspects of this problem represent a challenge to the multi-objective algorithm. First, there exist six isolated solution regions in the Pareto set. Smaller regions *Reg1*, *Reg5* and *Reg6* consist of the designs that are non-dominated in the mass objective. The constraints become active on the boundary of the search space where  $x_d$  has the smallest value. In the vicinity of the points where the stress in the bars exceeds the allowed value we observe the spikes in the displacement function (Figure 4.5a).

It should be noted that the mechanical objectives are symmetric with respect to  $y - y_{max}/2$  axis. Because of the symmetry of the problem in the mechanical domain, the Pareto regions occur on both sides of the symmetry axis, e.g. *Reg1* and *Reg6*, *Reg2* and *Reg4* shown in Figure 4.5d. In the EM domain, the symmetry is not preserved because of the feed position, which results in the Pareto-optimal design regions of varying size and density.

It should be beneficial to find the locally-optimal designs in each of the objectives and explore the space around these local optima in other domains. This will help with identifying the solutions of intermediate quality that represent best trade-offs between the objectives.

#### 4.2.4 Benchmark B3: Sizing Optimization of a Two-bar Truss

The second variant of this problem (the structural part) has been commonly used to benchmark the performance of the multi-objective algorithms. The problem is formulated as follows. Given a horizontal monopole antenna in Figure 4.6 loaded with weight  $P$  and given its material properties (density  $\rho$ , Young's modulus  $E$ , yield stress  $\sigma_{all}$ , and electric conductivity  $\sigma$ ), determine  $h$ ,  $w$ , and wire radius  $r$ , such that the antenna has minimum weight, experiences minimum displacement at node 3, can withstand stresses up to the yield stress and has the maximum possible realized gain perpendicularly to the ground plane:

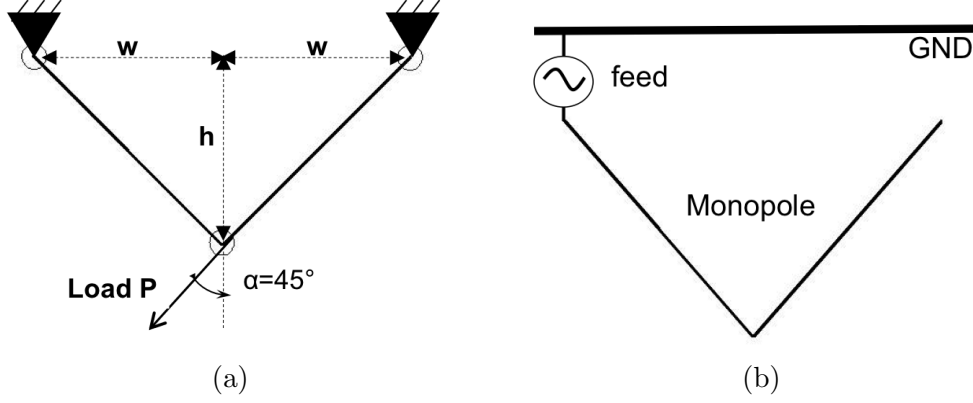


Figure 4.6: B3: Problem definition in the mechanical and EM domains. (a) Illustrates the two-bar truss under load and defines the design variables. (b) The corresponding antenna problem - monopole over an infinite ground plane.

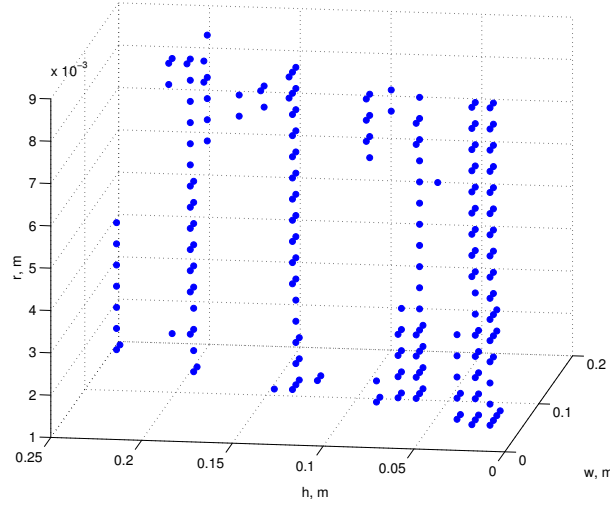
$$\begin{aligned}
 &\text{minimize} && f_1 = 2\sqrt{w^2 + h^2}\pi r^2 \rho \\
 &&& f_2 = \frac{(w^2 + h^2)^{3/2} P}{2\sqrt{2} E \pi r^2 h^2} \\
 &&& f_3 = 1/RG(w, h, r) \\
 &\text{subject to} && \sigma_{max} < \sigma_{all} \\
 &&& h_{min} \leq h \leq h_{max} \\
 &&& w_{min} \leq w \leq w_{max} \\
 &&& r_{min} \leq r \leq r_{max}
 \end{aligned}$$

where  $f_1$  is the mass of the structure,  $f_2$  is the displacement at node 3,  $f_3$  is the realized gain.  $\sigma_{max}$  denotes the maximum stress in the bars caused by the applied load and should not exceed the material-specific yield stress  $\sigma_{all}$ :

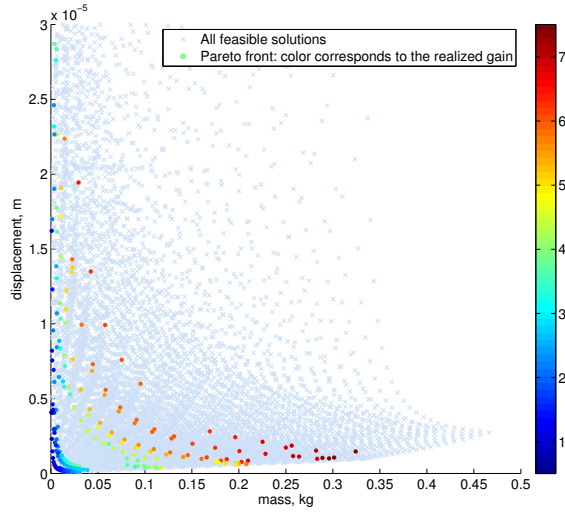
$$\sigma_{max} = \frac{P}{2\sqrt{2}} \frac{(w + h)\sqrt{w^2 + h^2}}{wh\pi r^2}$$

The Pareto-optimal solutions are presented in Figure 4.7b. For clarity, the data is plotted in 2D, with the color-coded EM objective and the mechanical objectives along the  $x$  and  $y$ -axis. The gray markers indicate all feasible mechanical solutions. The scattered data with the colored markers are the non-dominated solutions with the color corresponding to a certain  $RG$  value. Most optimal solutions lie on or close to the boundaries of the feasible region. The Pareto-optimal front consists of several distinct regions. In the design space

(Figure 4.7a), each region corresponds to a  $(w, h)$  pair and is continuous in the value of the wire radius  $r$ . The stress constraints become active for small wire radii, making solutions on the boundaries of these regions infeasible. In the design space, it results in several small disconnected sets of solutions that are difficult to locate. The multi-objective algorithm should be able to discover the various regions on the discontinuous and non-convex Pareto front.



(a) Design space



(b) Objective space

Figure 4.7: B3: Pareto solutions for the two-bar truss. (a) Pareto solutions in the decision space. (b) Feasible points in the objective space and the Pareto-optimal points with the color corresponding to a certain  $RG$  value.

### 4.2.5 Benchmark B4: Topology Optimization of a Ten-bar Truss

In B4, we consider topology optimization of a ten-bar truss structure. In classical and EA literature, the combinatorial problem of truss topology design is reformulated as a sizing optimization problem using the ground structure approach [4]. The goal of this approach is to find the optimal subset of truss members defined in the ground structure, which consists of a set of fixed nodes and a set of all allowable connectivities between them. The cross-sectional areas of the bars used as design variables are varied continuously between some maximal value and zero so that the bars can be made vanishingly small and eventually removed from the design. Figure 4.8a shows the loaded ground structure used in B4.

In mechanical domain, we want to minimize structure's mass and deflection from the unloaded position subject to stress constraints in the members. In the EM domain, we seek to find the topology with the optimal radiating properties at 100 MHz as described by the magnitude of the eigenvalue of the first characteristic mode. Since the largest dimension of the structure is comparable to the wavelength (approximately  $\lambda/5$ ), the ground structure already possesses a relatively efficient first eigenmode with eigenvalue  $|\lambda_1| = 6$ . Besides optimizing the radiating properties, we are interested in studying their sensitivity to the bar's radii. Determining how much improvement can be achieved by varying the bar's radii of the antenna structure is also of interest in solving this MOP.

The MOP is defined as follows:

$$\begin{aligned}
& \underset{\mathbf{A}}{\text{minimize}} && f_1 = \mathbf{u}(\mathbf{A})^T \mathbf{F} \\
& && f_2 = \rho \mathbf{A}^T \mathbf{L} \\
& && f_3 = \lambda_1(\mathbf{A}) \\
& \text{subject to} && \sum_i a_i l_i \mathbf{K}_i \mathbf{u} = \mathbf{F} \\
& && \sigma_{max} < \sigma_{all} \\
& && -a_{max} \leq a_i \leq a_{max} \\
& \text{where} && i = 1 \dots 10
\end{aligned}$$

where  $\mathbf{A} = [a_1 \dots a_i \dots a_{10}]^T$  is the column vector of the bar areas;  $f_1$  is the compliance of the truss calculated as a product of the displacement vector  $\mathbf{u}$  and the vector of nodal loads  $\mathbf{F}$ ; it expresses the amount of work done by the external forces to deform the structure. The second objective  $f_2$  is the mass of the truss, with  $\mathbf{L} = [\mathbf{l}_1 \dots \mathbf{l}_i \dots \mathbf{l}_{10}]^T$  denoting the vector

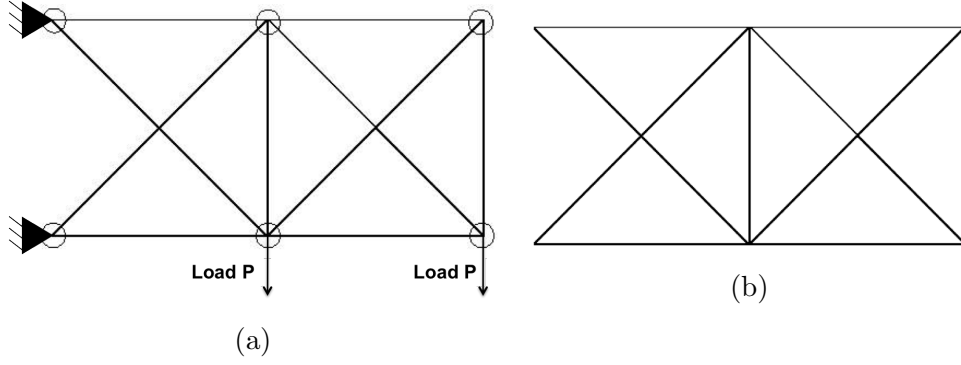


Figure 4.8: Definition of the problem B4 in the mechanical and EM domains. (a) Ground structure - the full ten-bar truss - loaded with the same load  $P$  at the two bottom nodes. (b) In the EM domain the metallic structure of the truss is considered a radiator and its properties are evaluated using the theory of characteristic modes. Optimization variables are the cross-sectional areas of the bars.

of bar lengths.  $\lambda_1$  is the eigenvalue corresponding to the first radiating mode calculated from the theory of characteristic modes (TCM) at 100 MHz.

The first constraint function describes the conditions of static equilibrium of the truss.  $\mathbf{a}_i \mathbf{l}_i \mathbf{K}_i$  is the element stiffness matrix for bar element number  $i$ ; the sum of these matrices determines the global stiffness matrix  $\mathbf{K}$ , which is positive definite for feasible trusses (i.e. structures that are not mechanisms or moving rigid bodies under the specified load). Then the displacements are calculated as  $\mathbf{u} = \mathbf{K}^{-1} \mathbf{F}$  and removed from the problem. In our implementation this is always the case, as the infeasible structures are identified and assigned a very large score before the mechanical analysis is run. Note that for the given feasible topology, compliance is a convex function of the cross-section areas and the existence of solutions for minimizing the compliance is guaranteed [74].

The other constraints restrict the maximal stress  $\sigma_{max}$  in the truss members and impose the bounds on the cross-sectional areas. The design variables are allowed to take on negative values to enable the changes in the truss topology. When the area of the bar falls below the specified minimum value  $a_{min} = 1e^{-7}$ , the bar is removed from the structure for calculation of EM and mechanical objectives. The use of negative areas during initialization ensures the diversity of topologies in the starting population.

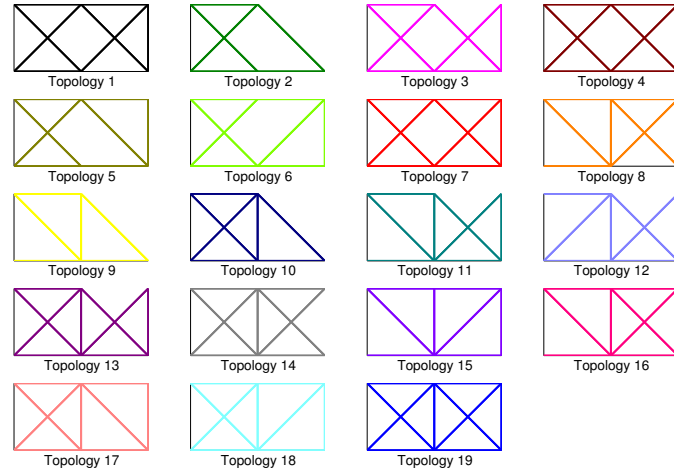
The definition of the structural problem largely follows the formulation by Deb [22] though the dimensions of the ground structure and the amount of applied load are different. Our definition also differs in the choice of one of the mechanical objectives - Deb minimizes the displacement rather than the compliance of the truss. However, the two formulations

are equivalent and we expect to obtain similar topologies in the mechanical domain as in [22].

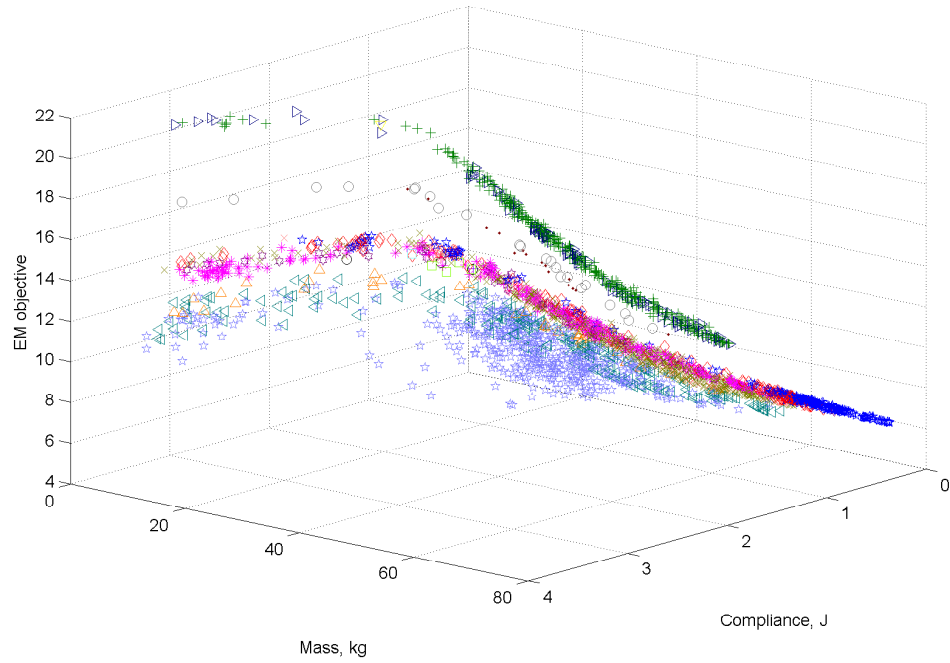
The Pareto solutions obtained in multiple runs of the optimization algorithms on B4 are shown in Figure 4.9. Figure 4.9a summarizes the topologies present in the found Pareto set; the color of the points in Figure 4.9b maps the objective values to the corresponding topologies. We observe that the Pareto front consists of several continuous regions, each of which corresponds to a different topology. Within such a region, the designs differ in the values of their cross-sectional areas. The stress constraints can further split a single-topology region into multiple segments, as in the case of topology 4 (brown points in Figure 4.9b below the green crosses). The designs with topology 4 lie on the constraint boundaries, as do some of the designs with a neighboring topology 14 (gray colored circles) which differs from topology 4 in only one central member; the introduction of a thin vertical member strengthens the structure, such that the constraint is no longer violated. We observe multiple design pairings of this type where the neighboring topology fills the gap in the Pareto front created by the stress constraints (topology 4 and 14, 2 and 10, 5 and 7, etc.). In general, the regions of neighboring and similar topologies overlap.

To validate our results, we compare the trade-offs in the mechanical objectives to the solution of the ten-bar problem by NSGA-II presented in [21]. Deb’s Pareto set contained only two optimal topologies that are also present in our solution, namely topology 2 and 7. The overall shape of the trade-off curve between the mechanical objectives (compliance vs. mass) also matches well with Deb’s findings. However, there are some important deviations in our results: our multi-objective study finds a more diverse set of topologies in the mechanical domain. Along the Pareto front, designs with topology 2 (green crosses in Figure 4.9b) that prevail among the solutions non-dominated in mechanical objectives are competing with topology 10. Though direct comparison of the results is not possible due to differences in the problem definition, we note that Pareto set in Deb’s study is missing the ground structure, which has the largest mass but cannot be dominated by any other design in the displacement (or compliance) objective. In Figure 4.9, this region shows as a set of blue stars on the boundary of the Pareto surface where lowest compliance is reached.

Problem B4 measures how well the performance scales with the number of design variables. Increased search space exacerbates the difficulties encountered in previous benchmarks: the discontinuous, non-convex Pareto surface consists of multiple competing regions with the various topologies competing within each region. An important metric will be the number of optimal topologies that the algorithms will be able to locate in a single run.



(a)



(b)

Figure 4.9: Pareto solutions for the ten-bar truss problem B4. (a) Pareto-optimal truss topologies. (b) Pareto surface with the three minimization objectives on the axis. The color of the points matches to the corresponding topologies in (a).

## 4.3 Multi-objective Optimization with Local Search

We propose a new multi-objective optimization algorithm with local search (MOLS) that starts by obtaining the local optima in each objective and then proceeds by exploring the space between the obtained solutions. Locally optimal solutions and their neighborhoods in individual disciplines are likely to be part of the Pareto front. Attaining these optima requires evaluation of the candidates in only one of the objectives; for local search, gradient-based methods can be applied which usually require small number of iterations to converge especially when analytical expressions for gradients are available, e.g., in the mechanical domain. In the initial stage of the search, the optimization in individual domains can be run in parallel, independently of each other. In this way, domain-specific techniques can be used to achieve best results.

The pseudocode for MOLS is given on page 85; in the following discussion, line numbers refer the reader to the corresponding operation in the pseudocode. In MOLS, optimization in each domain starts with the same population of solutions (l.6). Each individual is optimized in each objective, and as a result, the size of the current population  $CP$  increases from  $N$  to  $mN$ , where  $m$  is the number of objectives (ll.7-9). The initial population size  $N$  is chosen to be small, and the algorithm relies on the mutation for maintaining diversity in the first iterations. Local search also helps generate a more diverse population, because local optimization of the same candidate solution  $x_i$  in each objective usually leads to local optima spread out in the search space.

Objectives of the remaining solutions are evaluated in each domain (l.10), and a dominance sort is run to eliminate the dominated solutions (l.11). The current non-dominated set is used to generate the population for the next iteration: first, triangulation is created over the set of non-dominated solutions (l.13); the edges in the triangulation define the neighborhood relation for each design point. The midpoints of the edges define the next population of solutions (l.15). Some of them are added directly to the offspring population (l.16). Points that belong to longer edges undergo mutation and are passed as starting points to the local search (ll.17-19). The shortest edges are excluded from mating (l.14). The algorithm iterates through these steps until the specified number of evaluations is reached.

The approach can be viewed as a special case of the problem decomposition with the number of subproblems equal to the number of objectives. The subproblem's scalarization functions are the objective functions. Like many memetic algorithms, MOLS can result in

a poor distribution of solutions along the Pareto front. Because local search is implemented as a deterministic procedure, the algorithm can get stuck when offspring do not produce any new solutions in the Pareto set. In the crowded regions of the search space, local search starting from multiple points will terminate at the same local optimum, wasting computational time and ignoring the trade-off solutions in its vicinity. To avoid algorithm's premature convergence and preserve diversity, care must be taken in the generation and selection of the offspring population for the local search. The following modified operators are used:

1) The depth of the local search in each objective is varied between iterations. As the search proceeds, we decrease the number of function evaluations during the local step, forcing the algorithm to terminate at a sub-optimal solution, which then competes with the others for its place in the Pareto set. Following the descent directions in the vicinity of the local optimum in a given objective, local search explores solutions along the slopes that can be non-dominated in other objectives. Toward the end of the run, when the candidate solutions have congregated in the most promising areas of the search space, local search becomes virtually inactive. New candidate solutions are added primarily between the neighboring designs, with the neighborhood relation defined by the triangulation of the non-dominated designs.

2) Small edges: the design points that lie very close to each other are excluded from producing offspring. Duplicate points are removed during triangulation.

3) Diversity is also maintained by the mutation operator. We add Gaussian noise with zero mean and standard deviation equal to 10% of the upper bound in the corresponding dimension. The candidates chosen for the local search belong to the longest edges in the triangulation (1.17).

4) At each iteration, the offspring that are not sent to the local search procedure are selected randomly from the current population (1.16 on page 85). This randomness helps preserve diversity in all search stages, because it adds the midpoints of longer edges directly into the offspring population. As the search progresses, the density of solutions around the locally optimal areas increases, the proportion of longer edges connecting these regions and the probability of their selection decreases. However, it does not go to zero and design points away from the rigorously exploited regions are occasionally introduced. Random selection also ensures a more uniform distribution of candidates in the dense Pareto areas.

In MOLS, several parameters control the balance between the local and global search:

---

**Algorithm 1** Multi-objective Optimization with Local Search (MOLS)

---

**Assumptions:** effective local search in each objective that can handle constraints; triangulation procedure  $Tri$  for computing the neighborhood relation

**Notations:**  $OP$  is the offspring population;  $CP$  is the current population;  $P$  is the non-dominated population that contains the non-dominated solutions found so far;  $x_i$  is the vector of continuous or discrete design variables

**Inputs:** objective functions  $F = [F_1, F_2, \dots, F_j \dots F_m]$ , termination condition, the size of initial population  $N$ , the size of the population used in the local search  $N_l$ , the size of the offspring population  $N_o$ , minimum allowed distance between neighboring designs  $L_{min}$ , mutation operator and probability

**Outputs:** Non-dominated set  $P$  and non-dominated front  $PF$

```
5: Initialize population  $CP = [x_1, x_2 \dots x_N]$  uniformly at random
   Set  $X_l = CP$ ,  $P = \emptyset$  and  $OP = \emptyset$ 
    $Y = performLocalSearch(X_l)$ 
    $CP = Y$ 
10: Evaluate objectives  $F(CP)$ 
   Compute the non-dominated set  $P \subset CP$ 
   while TERMINATION CRITERIA not met do
     Compute the triangulation  $Tri$  on  $P$  and the lengths of edges  $L = ||Tri.edge_k||$ 
     Sort and reduce the set of edges  $inds = \{i | L_i \geq L_{i+1} \geq L_{min}\}$ 
15:   For  $j = 1 \dots |inds|$ , compute the edge midpoints  $M_j = (Tri.X_{j1} + Tri.X_{j2})/2$ 
     Randomly select  $N_o$  midpoints to fill  $OP \subset M$ 
     Select  $N_l$  midpoints of the longest edges for local search  $X_l \subset M$ 
     Apply mutation to  $X_l$ 
      $Y = performLocalSearch(X_l)$ 
20:    $CP = P \cup Y \cup OP$ 
     Evaluate objectives  $F(CP)$ 
     Compute the non-dominated set  $P \subset CP$ 
      $PF = F(P)$ 
   end while
25: return  $P$  and  $PF$ 
```

```
Method  $performLocalSearch(X_l)$ 
  for each  $x_i \in X_l$  do
    for each  $F_j \in F$  do
30:        $k = (i - 1) * m + j$ 
        $y_k = \arg \min_x F_j$ 
    end for
  end for
  return  $Y$ 
```

---

the size of the offspring population generated by averaging the neighboring points  $N_o$ ; the number of individuals passed to the local search at each iteration  $N_l$ ; the depth of the local search  $d$ , i.e. the number of evaluations allowed for the local optimizer in each of the objectives and most importantly, the schedule for adjusting the depth as the search progresses.

The proportion of the local to global search can be adjusted by limiting the number of iterations taken by the gradient-based optimizer. As the search proceeds, we reduce the number of fitness evaluations in each objective. The assumption is that the algorithm is able to identify the local optima in the early stages of the search - limiting the depth of the local search toward the end prevents the algorithm from converging to the local minima that it has already visited.

We use a geometric progression for adjusting the depth of the search  $d$ :

$$d_{i+1} = pd_i$$

Here  $p$  is the common ratio between 0 and 1. If the fractional  $d_i$  is always rounded to the lowest integer, we can find the upper bound on the total number of evaluations performed by the local search throughout the run. The relation is convenient for controlling the proportion of fitness evaluations allowed in the local search step. The algorithm is terminated when it reaches the specified number of total objective function calls TE. We select  $p$  such that the total number of evaluations during local search does not exceed some desired fraction  $f$  of TE.

$$f \cdot \text{TE} = N_l \sum_{i=1}^{n-1} d_i < N_l d_0 \frac{1}{1-p}$$

$$p = 1 - \frac{N_l d_0}{f \cdot \text{TE}}$$

There are some important differences between how MOLS and MOEAs search for the Pareto solutions. First, MOLS does not require special fitness assignment to rank the candidates (no crowding or density calculations are needed). In each generation, only non-dominated individuals survive. Second, most MOEAs define the density of solutions in the objective space, while MOLS operates in the design space. The mating can occur only between neighboring solutions as defined by the triangularization of the current population. MOLS allows for efficient integration of techniques from various domains. If optimization in one domain can be run more efficiently, MOLS provides a way to integrate multiple locally

optimal points into the population and use them to steer the search toward promising trade-off regions.

### 4.3.1 Implementation of MOLS

MOLS is implemented in MATLAB, and structural analysis in B2 and B4 is performed using MATLAB-based FEM codes [61]. In B1 and B3, analytical formulas and gradients for both mechanical objectives are known. EM objectives are evaluated numerically in the open-source method of moments code NEC2C [8].

*Local search.* In the mechanical domain, local single-objective optimization problems (SOPs) are solved by the MATLAB *fmincon* function. Because of the non-linear stress constraints, SOPs B2-B4 are handled by the sequential quadratic programming (*SQP*) - an algorithm for constrained non-linear optimization which at each iteration finds quadratic approximation of the Lagrangian function and linearizes the constraints to determine the feasible search directions [75]. One of the advantages of SQP is that it maintains strict feasibility with respect to the constraints, and returns a feasible solution at each iteration. The algorithm also recovers from failing steps, when during the iterations the objective function value becomes complex, NaN or infinity. The number of iterations in the SQP can be specified by the user.

The SQP algorithm must start from a feasible design point. While it was not a serious issue in B2, where a small number of infeasible designs were simply discarded from the search process, on B3 we learned that this strategy greatly degraded MOLS' performance. Based on this knowledge, in B4 we implemented a special repair procedure before running local optimization. For statically indeterminate trusses, the absent connections were added randomly (up to five attempts were allowed) until the topology became feasible.

The local search in the EM domain is performed using a randomized hill climber with the Gaussian update. At each iteration, small Gaussian perturbation is added to one of the design variables. If there is an improvement in the objective value, the perturbed vector is accepted as a new starting point, and the procedure is repeated. The algorithm terminates when the number of maximal function evaluations is reached or if no improvement is achieved for more than 20 iterations. Figure 4.10 shows the schematic representation of the local optimization procedure on B4.

*Triangularization.* In MOLS, parent selection is based on the triangularization of the current population in the design space. Triangularization imposes a neighborhood relation

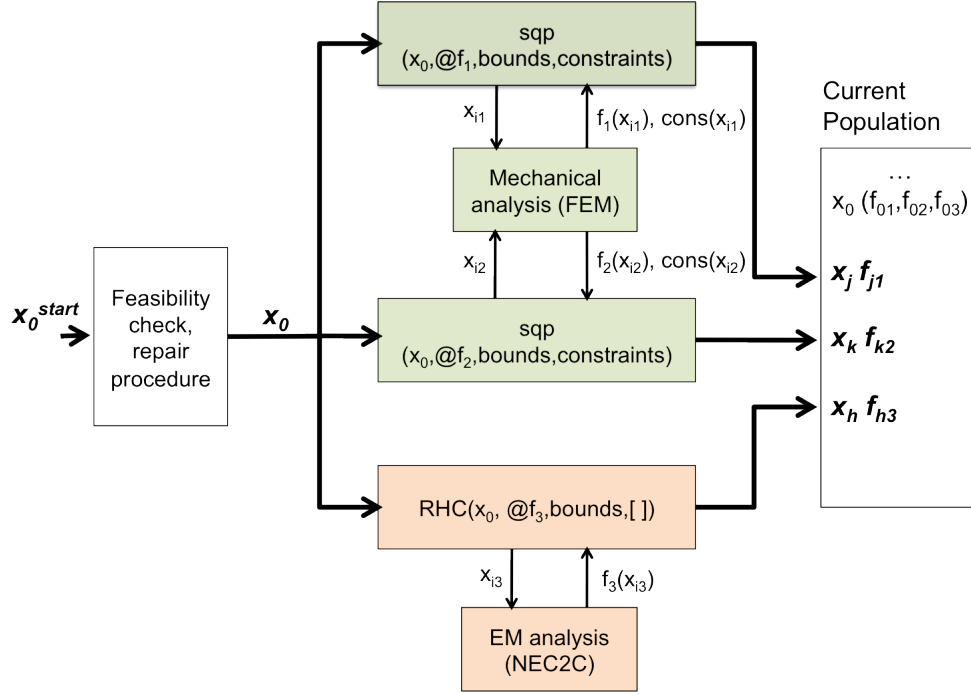


Figure 4.10: Local search step in MOLS algorithm as used in B4. The initial design vector  $\mathbf{x}_0^{\text{start}}$  is repaired and passed to local optimizers in each of the objectives. The two mechanical objectives  $f_1$  and  $f_2$  (shown in green) are optimized by the MATLAB's sequential quadratic programming (SQP) routine. An FEM simulator is used to evaluate objectives and constraints  $\text{cons}$ . In the EM domain (shown in orange), local search is performed by the randomized hill climber (RHC). The optimized design vectors are inserted into the current population.

such that only a triangle’s vertices can be mated with each other to generate offspring. The triangulation is constructed using the MATLAB function *DelaunayTri* that accepts a set of point coordinates, removes the duplicates, and outputs the matrix with the vertices of the triangles (or tetrahedra) and the connecting edges. This procedure is applied directly for building 2D triangulation in B2 (triangles) and 3D triangulation in B3 (tetrahedra). Since triangularization cannot be performed in one-dimensional space, in B1 we sort the candidate designs in the ascending order of the single design variable. The neighbors are allowed to create offspring. In higher dimensions, computing triangulation becomes very time-consuming. Therefore, in 10-dimensional B4 we first create several orthogonal projections of the initial coordinates on a 3-dimensional space in which the triangulation is computed. The obtained connectivity matrix and corresponding lengths determine the neighborhood relation.

## 4.4 Comparison of the Algorithms on Benchmark Problems

### 4.4.1 Experimental Set-up

We test the variants of NSGA-II and SPEA2 described in Chapter 2 and MOLS described in the previous section on each of the benchmarks. Random search is implemented for comparison: it finds non-dominated solutions from the randomly generated set of points in the search space. The number of random samples equals the number of total function evaluations. In our experiments, 1000 runs were performed for each algorithm on B1-B3 and 100 runs on B4.

The algorithm’s parameters used in each problem are summarized in Table 4.2. The population and archive sizes are determined by the cardinality of the global Pareto set  $P$  which was calculated from a large number of uniform samples in the feasible search space. For the second benchmark, for which the global Pareto set is large (858 points), the population size is taken as the mean size of the sets obtained by random search from 1000 random samples.

Termination is determined by the total number of evaluations performed in the EM objective, since the call to the EM simulator is the most compute intensive operation. In MOLS, we impose an additional stopping criterion to avoid the bloating of the non-

dominated set. Since the size of the stored Pareto set is not restricted, the averaging of neighboring points might create a large number of Pareto solutions, overcrowding certain regions. Therefore we terminate the algorithm when the number of individuals in the current set exceeds the archive size used in SPEA2.

This additional criterion seemingly puts MOLS at a disadvantage. However, the criterion is not very restrictive as by the time the Pareto set is filled up to the limit the local search is no longer contributing to the exploration of the search space. New regions can be discovered mostly by chance - through application of the mutation operation. The algorithm either keeps generating Pareto solutions between the closely spaced points or the search stagnates because of the limitations on the distance between the mating points. In addition, we adjust the parameters of MOLS in such a way that the size of Pareto set reaches maximum approximately after the specified number of function evaluations. This is achieved by increasing the proportion of local search evaluations: the algorithm finds more local optima, while less evaluations are spent on exploiting the solutions. Thus, the resulting set at termination is representative of the algorithm’s capabilities.

The EA’s recombination and mutation operators have been taken from previous work [22]. In the first two benchmarks, whole arithmetic recombination creates an offspring as a weighted sum of the parental genes; the weight is a random number between 0 and 1. This approach is similar to the way offspring are created in MOLS – as the average of two neighboring solutions. On larger dimensions (B3 and B4), one-point cross-over has shown better performance.

The parameters for MOLS are selected using the following guidelines. The initial population size  $N$  is equal to the number of solutions passed to the local search ( $N_l$ ). The number of offspring from averaging the neighboring points is chosen as  $N_l \times num_{obj}$ , such that equal number of new candidates is generated by the two procedures at each iteration. The initial number of evaluations  $d_0$  is on average slightly larger than the number of steps required by the gradient-based optimizer to terminate at the locally optimal point. It is determined before the run as follows: the local search algorithm is allowed to take as many steps as necessary for convergence for each individual in the initial population;  $d_0$  equals the mean number of evaluations in the EM objective. The common ratio  $p$  is chosen according to equation 4.3 such that in B1 two thirds of total EM evaluations (TE) are performed by the local search ( $f = 2/3$ ), 90% of TE in B2, 75% in B3, and 80% in B4.

In each run, we collect statistics about the found Pareto set: the set coverage  $C(P, \bar{P})$  of the found  $\bar{P}$  by the true  $P$ , generational distance  $GD$ , and spread  $\sigma$  as defined in Chapter

Table 4.2: MOA’s and random search parameters.

Parameter	B1	B2	B3	B4
Number of runs	1000	1000	1000	100
Total EM evaluations	340	1040	2000	4000
MOEAs: SPEA2, NSGA-II				
Population size	20	160	200	150
Archive size (SPEA2)	20	160	200	150
Rec. prob.	0.8	0.8	0.8	0.9
Mut. prob.	0.1	0.1	0.1	0.1
Rec. operator*	WAR	WAR	1PX	1PX
Mut. operator**	$N(0, 0.1)$	$N(0, 0.1)$	$N(0, 0.1)$	$N(0, 0.005)$
MOLS				
Initial population size	4	10	20	20
$N_l$	4	10	20	10
$N_o$	8	30	60	30
Initial $d_0$	40	50	50	100
$p$	0.3	0.5	0.34	0.7
Rec. operator	averaging of neighboring solutions			
Mut. operator**	$N(0, 0.1)$	$N(0, 0.1)$	$N(0, 0.1)$	$N(0, 0.001)$
Neighborhood relation	triangle vertices in Delaunay triangulation			

\*WAR: whole arithmetic recombination; 1PX: one-point crossover

\*\* $N(0, \sigma)$  Gaussian with zero mean and  $\sigma$  standard deviation

2, section 2.3.5. For B1, we are interested in the number of runs in which the champion solution has been found and how well the spread of solutions in the first region is. In B2, we also record the number of solutions in each of the Pareto regions. In B4, the distribution of Pareto-optimal topologies is of interest.

## 4.4.2 Experimental Results

### 4.4.2.1 Performance on B1: Cantilever Beam

B1 is a one-dimensional optimization problem - very simple even for the random search. The only difficulty is the existence of several champion solutions around the global minimum of the VSWR, separated from the main continuous Pareto-optimal region. The successful algorithm should be able to locate the stand-alone individual and maintain a uniform spread of solutions along the continuous region.

In addition to  $C$  and  $GD$ , we use two metrics to compare the behavior of the algorithms

in this landscape: we count the number of runs, in which the smaller region was found and calculate the distribution of solutions within the larger region. The primary goal of this test is to reveal the problems and pitfalls with the approach taken by MOLS in discovering the Pareto set.

MOLS is expected to perform well on this problem. First, because of the local search step MOLS can get close enough to the optimal VSWR so that the solution cannot be eliminated from the population during the non-dominance sort. Second, in the dense Pareto region, the objective functions show opposite behavior: the deflection is increasing with the length of the beam, while the VSWR is decreasing. Hence, the local search will move in opposite directions in each of the objectives, exploring the solutions along the whole region. Third, algorithm’s offspring generation is favorable to finding the Pareto set, because the midpoints between the already found designs in the first region are also Pareto-optimal.

MOLS performance is comparable to NSGA-II and random sampling. It finds the optimal VSWR region in 88% of the runs vs. 95% by NSGA-II and 99% by random search. It achieves 0 set coverage 84% of the time. These results are summarized in Table 4.3.

The Pareto fronts with the best spread in the first region are shown in Figure 4.11a. NSGA-II and MOLS achieve the most uniform distribution along the front. SPEA2 can get a good distribution closer to the search boundary but fails to include the solutions in the tail of the curve.

The differences in algorithms’ behavior are best illustrated by the worst-case performance. Figure 4.11b shows the Pareto fronts with the worst spread of solutions (highest  $\sigma_1$ ) in the first region. It is noted that in the runs with poor solution distribution and set coverage, MOLS tends to create many solutions around the local minima of the VSWR. The final Pareto front also contains duplicate points that degrades the spread value; the points, however, cover the whole region, including the extreme objective values. This is in contrast to NSGA-II and SPEA2, for which the worst results mainly contain solutions near the search boundary (small values in the first objective  $f_1$ ).

Overall, MOLS’ metrics have a much larger variance than the other algorithms. It can reach the lowest generational distance and the most uniform spread (Table 4.3) but it also has runs in which half of the obtained solutions are not Pareto-optimal.

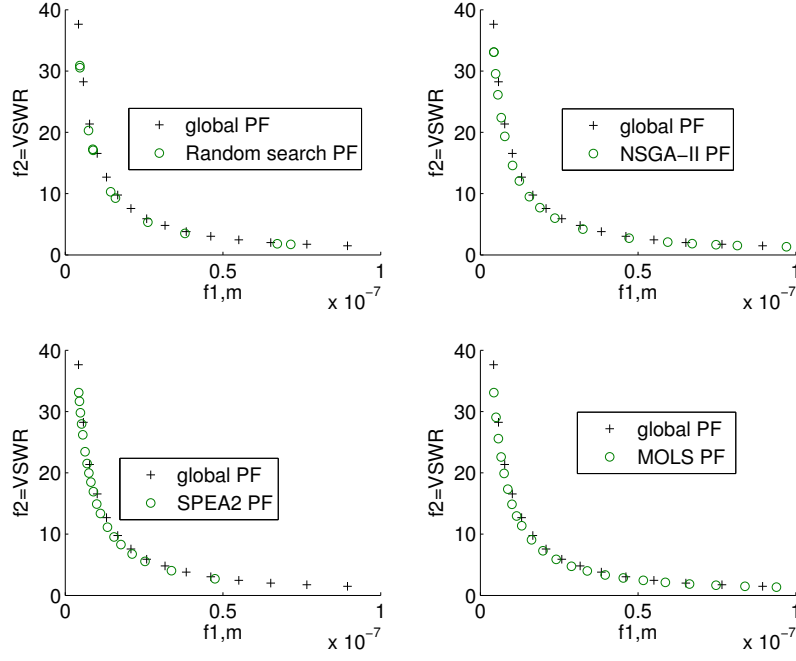
The main shortcoming of MOLS in B1 seems to be its dependence on the initialization and lack of diversity preservation during the run. MOLS starts with a small population: since every candidate must undergo local optimization, a larger population would introduce many duplicate points and closely spaced solutions, wasting evaluations. It is expected that

optimization in different objectives would produce a diverse set of new candidates. As the algorithm proceeds, local search remains MOLS’ primary mechanism for exploring the search space. However, if the number of evaluations in the local step is reduced very fast (as in B1), this exploration time becomes very short and the solutions tend to congregate around the local optima in each objective. On more complex problems with larger number of design variables and objectives (B2, B3, and B4) this issue is less pronounced, because the algorithm is given more time (i.e., fitness evaluations) to explore and local search in multiple objectives produces locally optimal designs widespread in the search space. In addition, to mitigate the lack of diversity, dominance sort is only run (l. 11, l. 21 on page 85) when the current population  $CP$  reaches 10x the size of the initial population  $N$ , so that the algorithm can accumulate a large number of promising candidates in various areas of the design space.

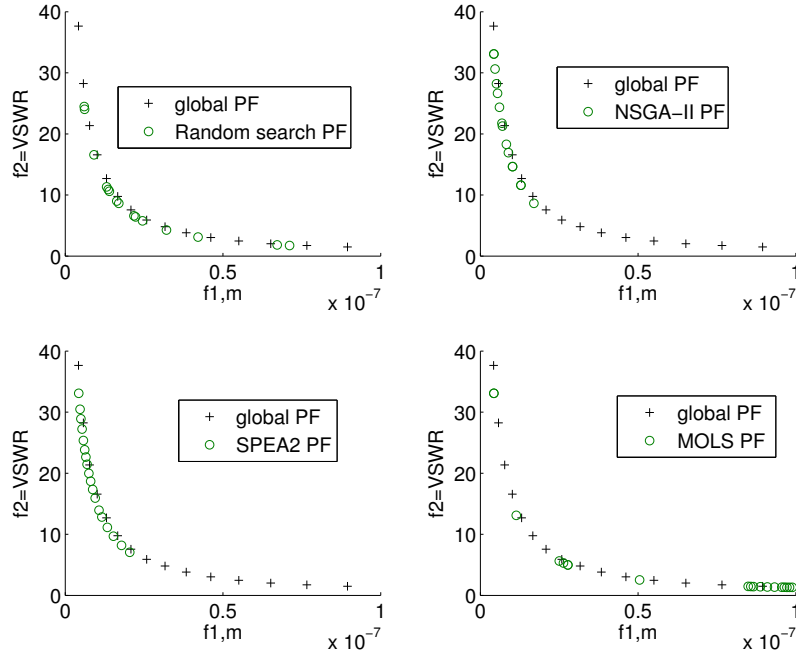
Unlike MOEAs, MOLS does not include any operators to discriminate against solutions in the objective space based on the dominance rank or crowding distance. Therefore, MOLS often overexploits the regions near the local optima. In some runs on B1, the final Pareto set is split evenly between the first wide Pareto region and the region near the global minimum of VSWR that only contains several champion solutions.

Table 4.3: Performance on B1. For each algorithm, the percentage of the runs in which all found solutions were Pareto-optimal, the generational distance to the global Pareto front  $GD$ , the spread of solutions along the front  $\sigma$ , and the percent of runs in which the found Pareto set contained the champion solutions located away from the main Pareto region. Note that lower values of  $GD$  and  $\sigma$  correspond to better performance.

	Metric	Random	SPEA2	NSGA-II	MOLS
% runs with C=0		77.8%	69.6%	92.4%	84%
GD	min	$2.2 \times e^{-4}$	$2.2 \times e^{-3}$	$1.6 \times e^{-3}$	$6.4 \times e^{-4}$
	median	$8.9 \times e^{-4}$	$2.5 \times e^{-3}$	$2.2 \times e^{-3}$	$1.4 \times e^{-3}$
	max	$2.0 \times e^{-3}$	$6.2 \times e^{-3}$	$4.7 \times e^{-3}$	$3.9 \times e^{-2}$
$\sigma$	min	0.29	0.48	0.26	0.18
	median	0.59	0.64	0.59	0.5
	max	1.01	0.77	0.85	1.1
stand-alone solutions found		99%	84.6%	95%	88%



(a)



(b)

Figure 4.11: Performance on B1. Distribution of solutions along the Pareto front found by each algorithm and the global Pareto-optimal front. (a) Pareto fronts with the best spread  $\sigma$ ; (b) Runs with the worst distribution of solutions. Because of low complexity of the problem, set coverage is good even in the low performing runs.

#### 4.4.2.2 Performance on B2: Topology Optimization of a Two-bar Truss

In this problem, we test whether the algorithms are able to locate multiple Pareto regions – inside and on the boundaries of the search space. Table 4.4 summarizes the percentage of runs (out of 1000) in which each of the regions was found, and the last column labelled *all regions* gives the number of runs in which the algorithm was able to locate all six regions. Illustration of the regions in the design space is given in Figure 4.5.

Table 4.4: Algorithm performance on B2: data shows the percentage of runs in which each of the disjoint Pareto-optimal regions *Reg1* – *Reg6* in the design space was located by each algorithm.

Algorithm	Reg1	Reg2	Reg3	Reg4	Reg5	Reg6	All regions
Random	98%	93.8%	100%	100%	99.6%	49.4%	45.7%
SPEA2	98.4%	87.4%	100%	100%	100%	45.1%	38.9%
NSGA-II	99.6%	79.5%	100%	100%	100%	80.1%	63.8%
MOLS	99.9%	87.0%	100%	100%	100%	83.9%	72.2%

In this landscape, the random search performs well: random sampling of the search space provides uniform coverage and reaches all regions in approximately half of the runs. Five regions are found in 95% of the runs. The median Pareto coverage by random search is calculated to be  $C = 0.25$ , which is lower than that of the NSGAII and SPEA2 by 0.1. Due to its local search step, MOLS has the best set coverage  $C$ . Being able to fine-tune the candidate solution, it approaches closer the Pareto front than the other algorithms. GD is best in the case of SPEA2, indicating that this algorithm is also able to find accurate Pareto solutions. The most uniform coverage of the Pareto front is achieved by NSGA-II, whose  $\sigma$ -value is twice lower than that of the other algorithms.

MOLS proves to be most effective in exploring the landscape: it finds all regions in 72% of the runs - more often than any other algorithm. In particular, it is better at finding solutions on the boundaries of the search space (*Reg1*, *Reg5*, *Reg6*). *Reg6* is especially hard to locate because it lies on the constraint boundary and includes only few solutions that are non-dominated in single objective, the mass of the truss. MOLS hits this region most often because the nonlinear constraint is handled effectively by the SQP algorithm. The NSGA-II crowding strategy is also successful in singling out this region of the search space: since the displacement is changing quickly, the sparsity of solutions in the objective space is high and NSGA-II keeps exploiting this area, creating multiple candidates. SPEA2’s distance-based strategy is not as effective: the algorithm fails to consistently preserve and

exploit promising solutions around *Reg6* because of the competing *Reg1* and *Reg5* that are similar in mass and displacement and are much easier to locate.

For each problem, we generate the plots of representative runs: for each algorithm, we show the run where all six regions were found. Among those, the run with the best set coverage  $C$  is chosen. Each subplot in Figure 4.12a shows the Pareto set obtained by each algorithm in comparison to the global Pareto set. Table 4.5 includes the set coverage  $C$ ,  $GD$  and spread for the plotted runs.

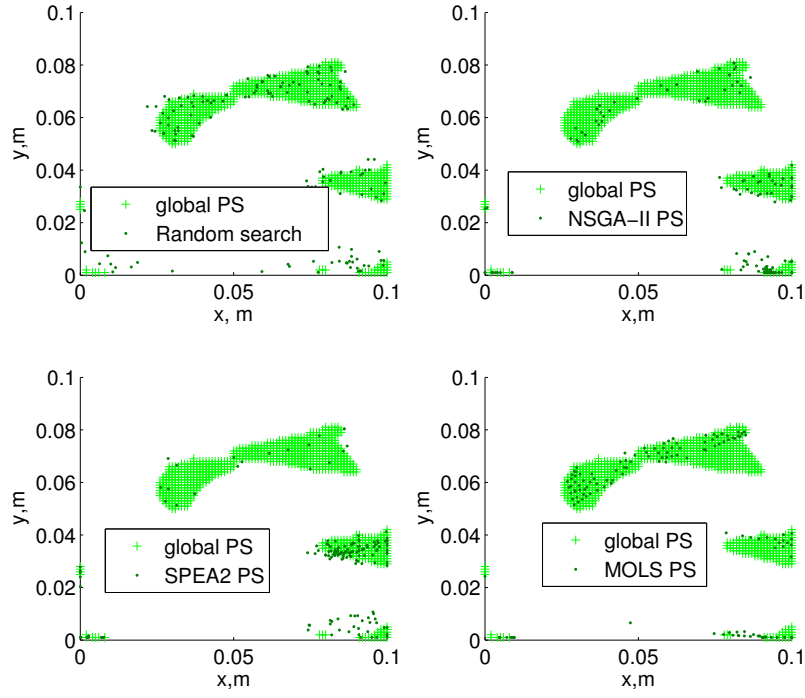
From Figure 4.12, NSGA-II and MOLS have preferred regions. For NSGA-II, multiple candidate solutions are concentrated in the corner region, while for MOLS wide regions (*Reg3* and *Reg4*) are overcrowded. In contrast, SPEA2 creates limited number of solutions in the broadest part of the Pareto set. All algorithms tend not to exploit the regions around the small values of  $x$  and  $y$  (*Reg1* and *Reg2*).

Though the design space metrics the results from NSGA-II, random search and MOLS look very similar and all these algorithms appear to identify the majority of Pareto solutions, the objective space metrics show significant differences (Table 4.5). At 0.21, the set coverage of NSGA-II is comparable to the set coverage by SPEA2 and random search – meaning that about 20% of NSGA-II solutions are dominated by the global Pareto points. Most of the dominated points are located around *Reg5* and *Reg6*, in the corner of the design space. Here, the EM objective is changing quickly as the function of design variables, and the distance from the closest Pareto values in the objective space varies significantly, resulting in poor set coverage and higher generational distance.

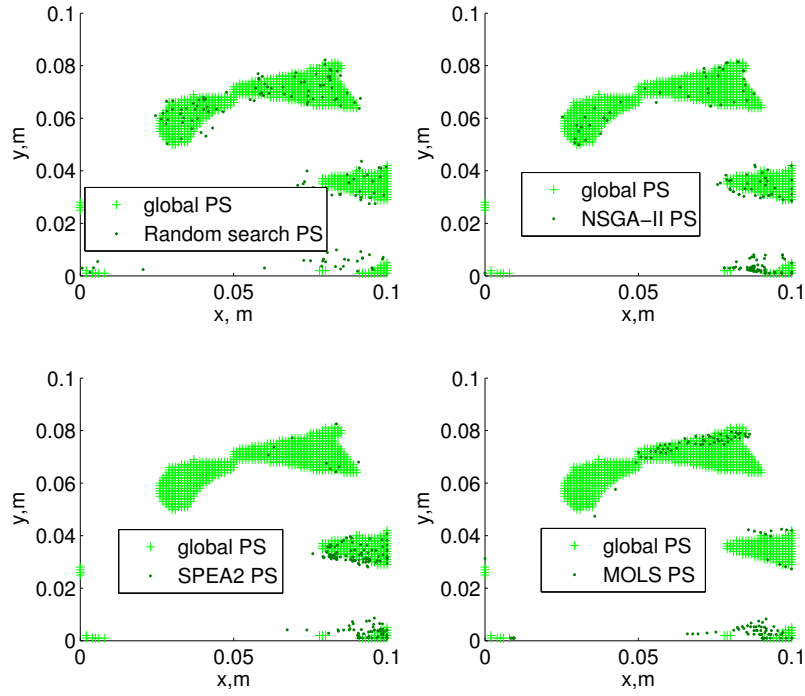
Table 4.5: Summary of performance metrics for the runs on B2 that had the best and worst set coverage  $C$ . Pareto solutions for these runs are plotted in Figure 4.12.

Algorithm	Higher performing runs			Lower performing runs		
	C	GD	Spread	C	GD	Spread
Random	0.23	$5.5 \times e^{-4}$	1.22	0.37	$1.9 \times e^{-3}$	1.0
SPEA2	0.26	$1.6 \times e^{-4}$	1.04	0.58	$7.3 \times e^{-4}$	0.83
NSGA-II	0.21	$2.9 \times e^{-4}$	0.52	0.72	$3.7 \times e^{-4}$	0.53
MOLS	0.05	$2.2 \times e^{-4}$	1.1	0.39	$3.2 \times e^{-4}$	0.95

The Pareto fronts obtained by NSGA-II and MOLS in the best runs are shown in Figure 4.13. Each plot represents trade-offs in each pair of objectives:  $f1$  is the displacement of the central node,  $f2$  is the mass of the truss and  $f3$  is the inverse of the realized gain of the truss-antenna. In the objective space, NSGA-II achieves a much better distribution of



(a) Runs with the best set coverage



(b) Runs with the worst set coverage

Figure 4.12: Performance on B2: the distribution of solutions in the design space for the a) highest performing and b) the lower performing runs for each of the algorithms.

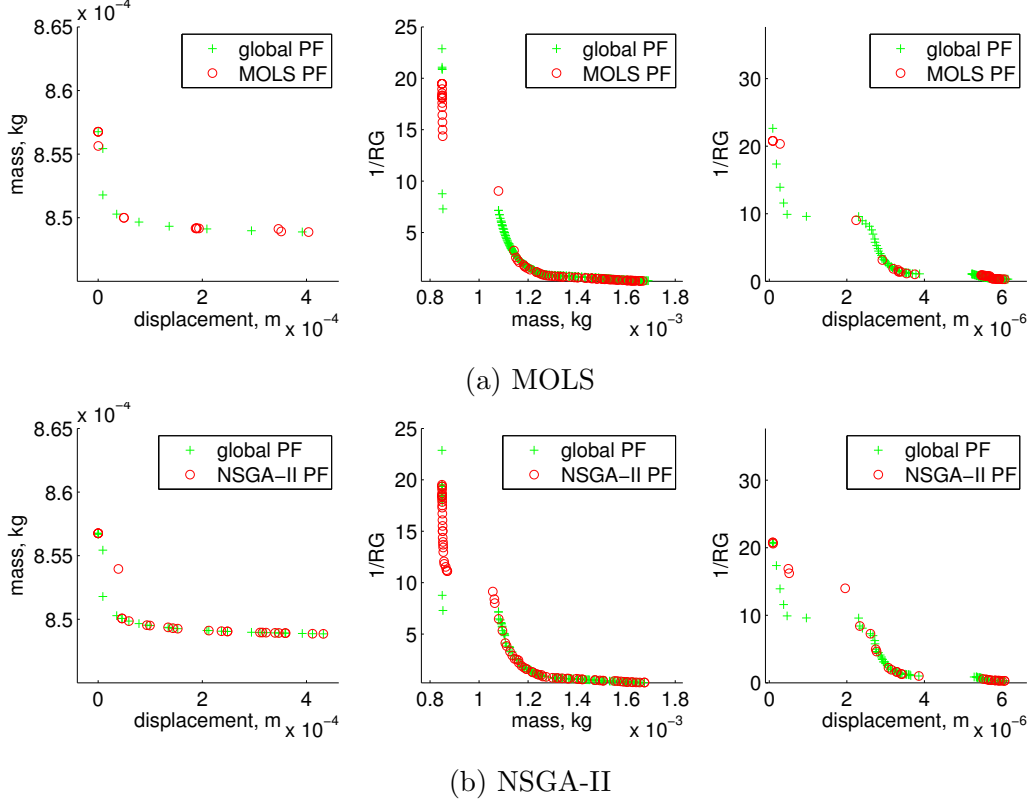


Figure 4.13: Performance on B2: Pareto front for the highest performing runs.

solutions along the Pareto front than MOLS and better approximates the overall shapes of the trade-off curves. MOLS fails to find the trade-offs in the mechanical objectives ( $f_1$  vs.  $f_2$ ), locating only the extreme values in  $f_1$  and  $f_2$ . Nevertheless, in this run, MOLS outperforms NSGA-II in terms of set coverage and generational distance because it keeps fine-tuning the solutions in the flat Pareto regions, while NSGA-II keeps exploiting regions with large fluctuations in the objective  $f_3$ .

For comparison, we also include the results of lower performing runs: for each algorithm, we select the run with the lowest number of covered regions. Among those, the run with the worst set coverage is selected (Figure 4.12b). Compared to the higher performing runs, there is not much difference in solution distribution in the design space for NSGA-II and the random search. One main problem is that in the lower performing runs these algorithms fail to locate *Reg2* and *Reg6* despite the large number of candidates around *Reg6*. MOLS over-exploits the two broad regions, and is unable to explore further. The corresponding Pareto fronts are shown in Figure 4.14.

Overall, the distance-based strategy of MOLS is at least as good as the objective dis-

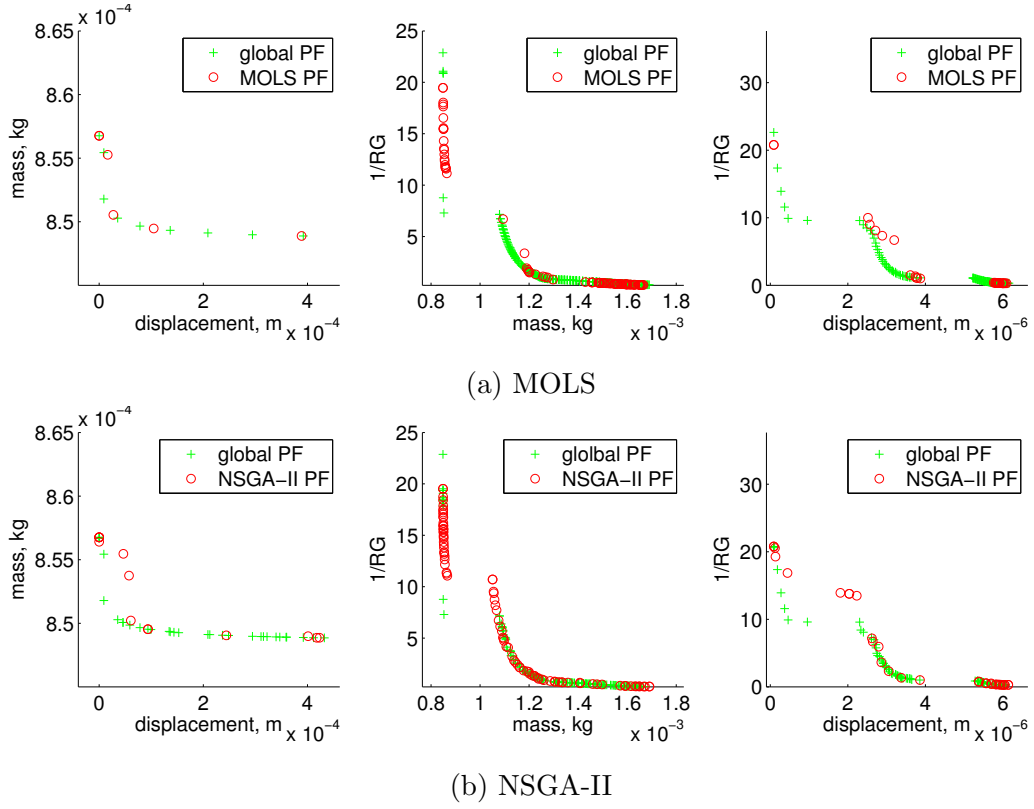


Figure 4.14: Performance on B2: Pareto front for the lower performing runs.

tance used by NSGA-II. The gradient-based optimization allows for better fine-tuning of the current candidate solutions and leads to the improvement in the set coverage and generational distance. Optimization in three objectives generates enough diversity in the population, such that all Pareto regions are located in most of the runs. On the other hand, more exploitation comes at the cost of the uniform exploration of the search space. In the objective space, MOEAs clearly reach a better distribution than MOLS.

#### 4.4.2.3 Performance on B3: Optimization of a Two-bar Truss

B3 is included in the set to test *i*) how well an algorithm’s performance scales with the number of dimensions and *ii*) how well an algorithm can deal with hard constraints. Some of the Pareto solutions lie on the constraints, causing discontinuities and non-convexity in the Pareto front. The harder optimization problem results in significant degradation in the performance of the random search.

The best found Pareto trade-offs, runs with the lowest  $C$ -value, are shown in Figure 4.15. The metrics summarized in Table 4.6 demonstrate that SPEA2 is able to obtain most diverse and accurate set of solutions. MOLS does not perform as well as the EAs and contains a large number of locally Pareto-optimal solutions in the final set, especially for the trade-offs between inverse of the realized gain  $f3$  and displacement  $f1$ .

Table 4.6: Metrics for the runs on B3 that had the best and worst set coverage  $C$ . The Pareto solutions for these runs are plotted in Figures 4.15 and 4.16.

Algorithm	Highest performing runs			Lower performing runs		
	C	GD	$\sigma$	C	GD	$\sigma$
Random	0.37	$1.13 \times e^{-4}$	0.8	0.68	$1.27 \times e^{-4}$	0.83
SPEA2	0.025	$5.5 \times e^{-5}$	0.8	0.32	$7.0 \times e^{-3}$	1.25
NSGA-II	0.035	$1.64 \times e^{-4}$	0.38	0.38	$7.5 \times e^{-5}$	0.65
MOLS	0.034	$9.8 \times e^{-5}$	1.1	0.5	$1.8 \times e^{-4}$	0.94

The plots illustrate the differences in how the algorithms traverse the search space. Though on average MOLS finds a less uniformly spread and accurate Pareto front, it tends to explore the regions underexploited by the MOEAs. MOLS finds a better approximation of the Pareto front between mass ( $f2$ ) and realized gain ( $f3$ ). Unlike the EAs, MOLS’ final set contains the optimal values in each objective (extreme points on the Pareto front); in the best-case performance, it is the only algorithm that is able to find the design with the

lowest EM objective. It maintains this property also in the worst-case runs, finding the outermost solutions among all algorithms (Figure 4.16).

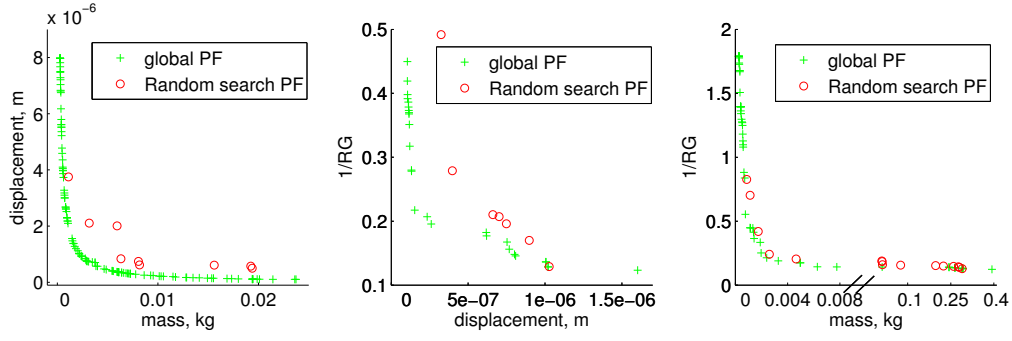
#### 4.4.2.4 Performance on B4: Topology Optimization of a Ten-bar Truss

B4 is an example of a multivariate, multi-objective problem with multiple constraints. The search space is vast, while the feasible truss topologies contribute only a small fraction of possible configurations. Random search performs very poorly in this type of landscape: random initialization produces a large number of statically indeterminate structures and in each run random search finds only a few non-dominated solutions.

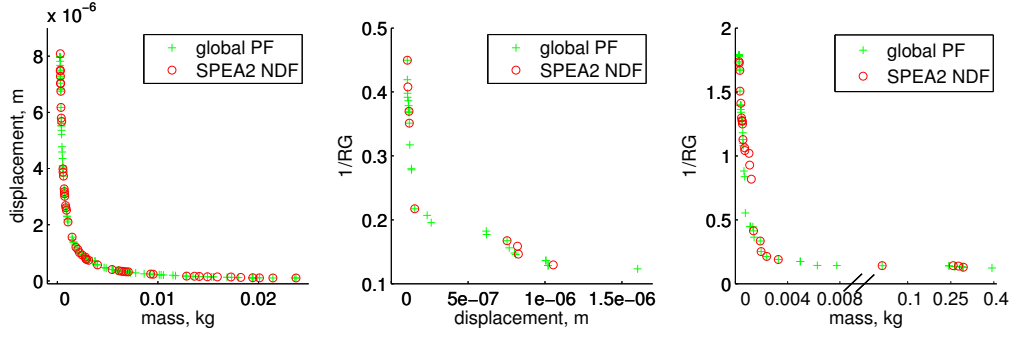
MOEAs do not use any special constraint handling techniques, while MOLS includes a special repair procedure that attempts to modify the topology to provide a feasible starting point for the gradient-based optimization algorithm. The algorithms' performance is illustrated with the trade-off surfaces corresponding to the runs with the best and worst distribution of solutions  $\sigma$  (Figures 4.18 and 4.17 and Table 4.7). We observe that MOEAs tend to explore regions with lower values of the EM objective and fail to find designs with the lowest mass. MOEAs also cannot locate the various topologies on constraint boundaries, while MOLS is more effective at this task due to the gradient-based constraint handling by SQP.

In contrast to MOEAs, MOLS finds many solutions along the middle ridge of the Pareto front including extreme values in compliance and mass. However, the algorithm has difficulties with identifying the best trade-offs between the mechanical objectives (the uppermost region in Figures 4.17 and 4.18). This can be explained by the MOLS' way of creating offspring by averaging the designs. In Figure 4.9a, the uppermost region in the objective space largely consists of designs with topology 2. Since this topology has a small number of bars, it cannot always be obtained by averaging the cross-sectional areas of the other feasible designs. The topology can be introduced primarily through a random mechanism, during initialization or mutation, making it hard for MOLS to find it.

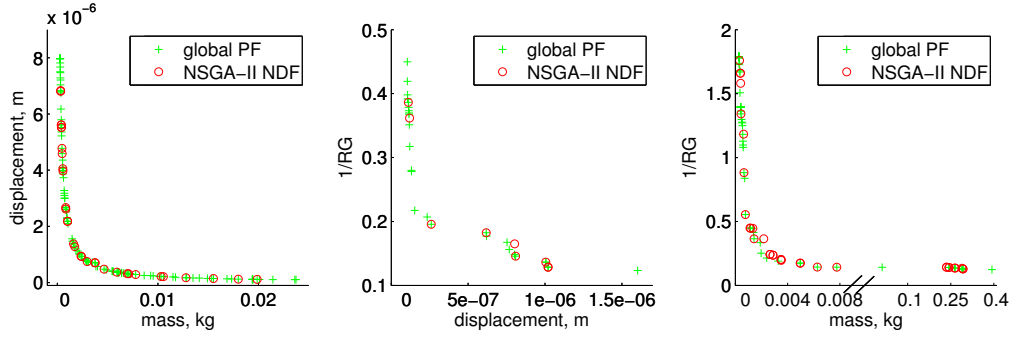
The distribution of Pareto topologies further highlights the differences between the algorithms' exploration strategies. Figure 4.19 shows the percent of experiments in which each Pareto-optimal topology was present in the final population of the algorithm. Topologies 7, 13, 17 and 19 appeared frequently in all populations. The topologies lack only one member in the second (farthest from the supports) section of the truss, resulting in small compliance and high mass. These heavy, most stable trusses are the easiest to locate as



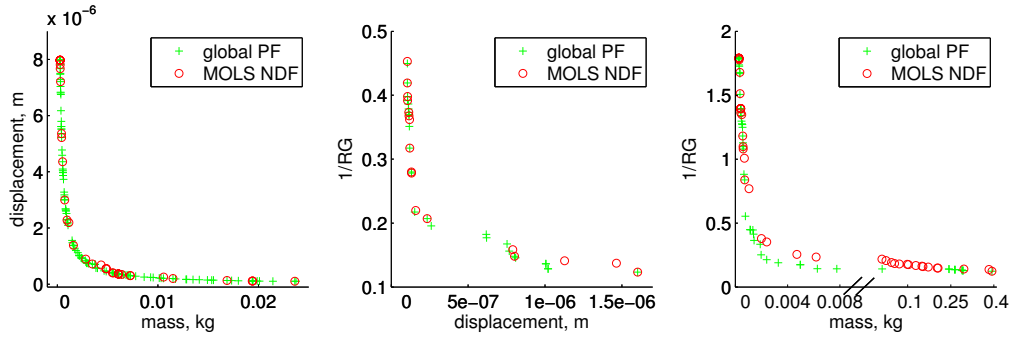
(a) Random Search



(b) SPEA2

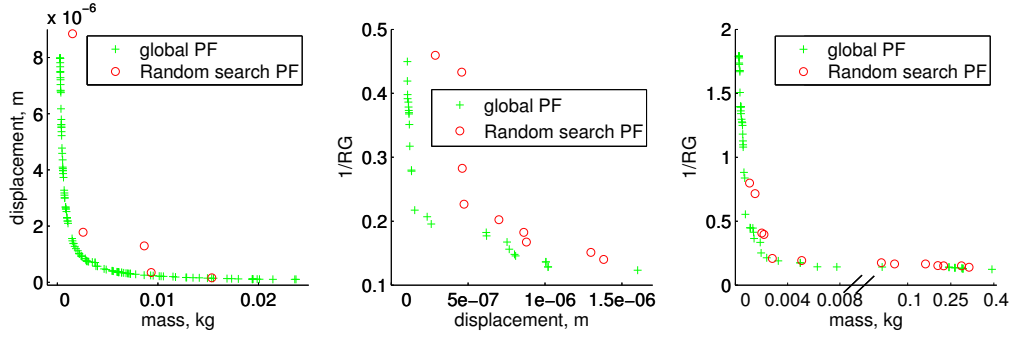


(c) NSGA-II

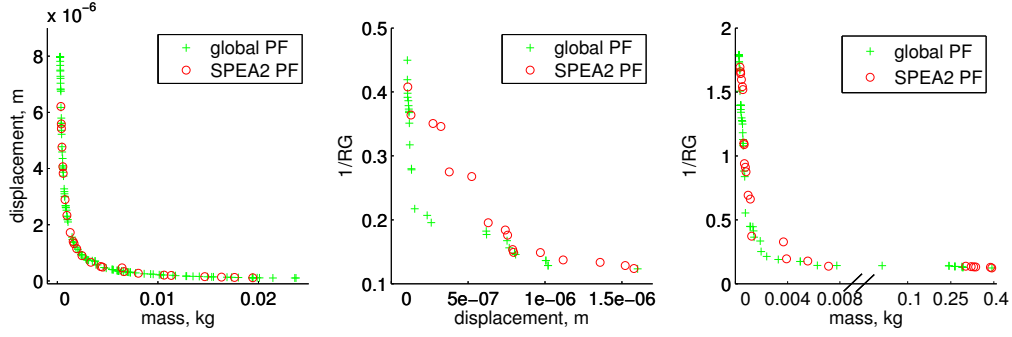


(d) MOLS

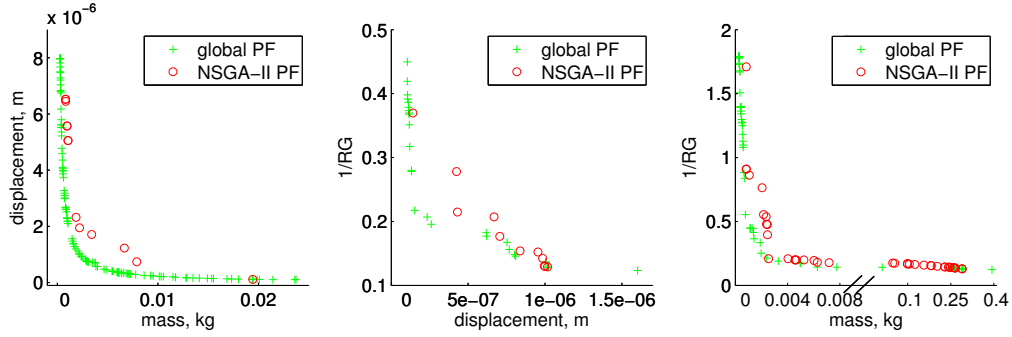
Figure 4.15: Performance on B3: Pareto front for the runs with the best set coverage.



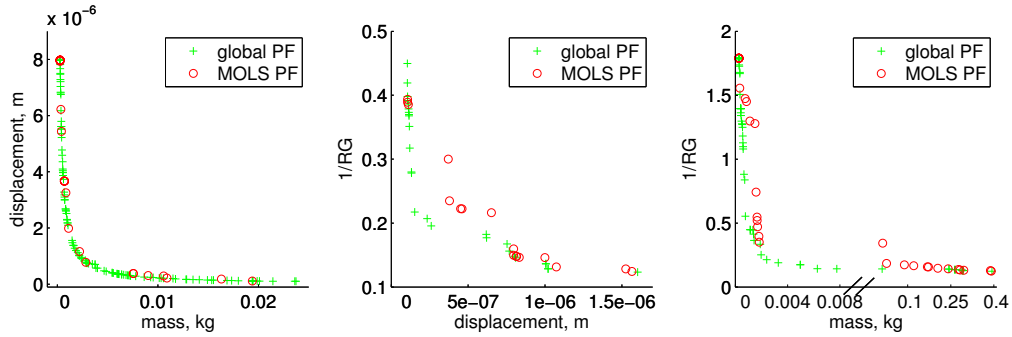
(a) Random Search



(b) SPEA2

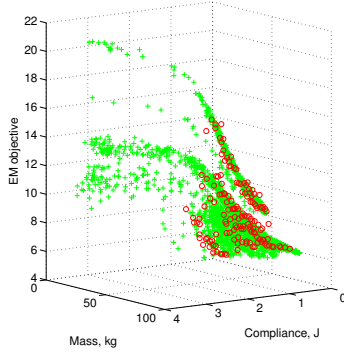


(c) NSGA-II

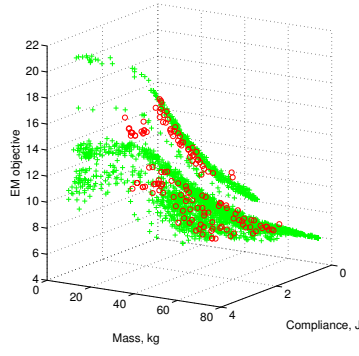


(d) MOLS

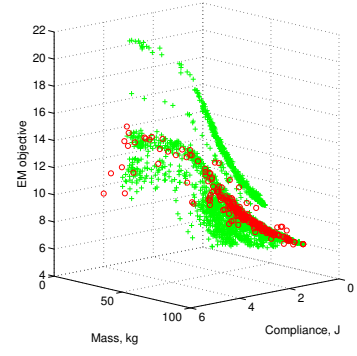
Figure 4.16: Performance on B3: Pareto front for the runs with the worst set coverage.



(a) SPEA2

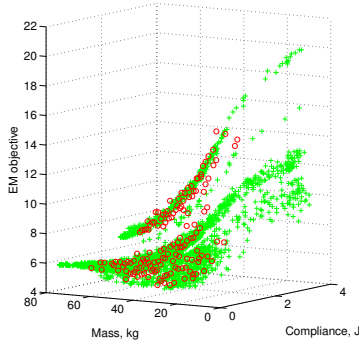


(b) NSGA-II

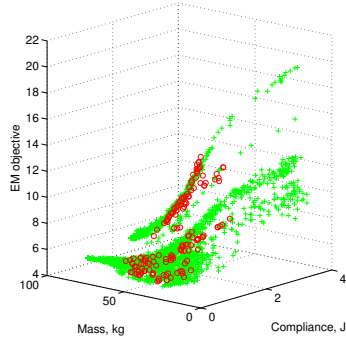


(c) MOLS

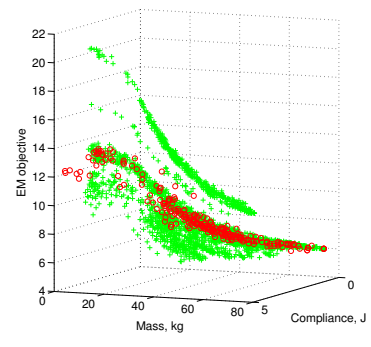
Figure 4.17: Performance on B4. Pareto surface for the runs with the lowest spread  $\sigma$ . Green points show the global Pareto solutions; red circles correspond to the front found by the algorithm.



(a) SPEA2



(b) NSGA-II



(c) MOLS

Figure 4.18: Performance on B4. Pareto surface for the runs with the worst spread  $\sigma$ . Green points show the global Pareto front; red circles correspond to the front found by the algorithm.

Table 4.7: Metrics for the runs on B4 that had the best and worst spread. The Pareto solutions for these runs are plotted in Figures 4.17 and 4.18.

Algorithm	Highest performing runs			Lower performing runs		
	C	GD	$\sigma$	C	GD	$\sigma$
Random	1	$9.2 \times e^{-2}$	0.61	1	$6.4 \times e^{-2}$	0.97
SPEA2	0.99	$2.1 \times e^{-2}$	0.67	0.92	$1.9 \times e^{-2}$	0.85
NSGA-II	0.97	$5.7 \times e^{-2}$	0.52	0.99	$7.6 \times e^{-2}$	0.88
MOLS	0.87	$1.75 \times e^{-2}$	0.74	0.99	$4.8 \times e^{-2}$	0.96

they can always be created from other topologies by the recombination operator, and all algorithms are likely to revisit these topologies multiple times during the run.

Because of the more effective recombination operator, MOEAs arrive at topologies 2 and 10 twice as often than MOLS. The designs 11 and 12 are also often absent from the MOLS' population. In the objective space they are non-dominated in the EM objective, suggesting that the randomized hill climber fails to obtain local minima in the EM domain. Including a more efficient local strategy can improve the performance in this respect.

Gravitating toward topologies with many members, MOLS usually terminates with a more diverse set of designs than MOEAs. It exploits the central region of the Pareto surface very well, locating multiple competing topologies with similar objective values, e.g. topologies 1, 8, 14 – 16, and 18.

To compare the performance of the algorithms we plot the distribution of the set coverage between each pair of algorithms on each benchmark problem. The results are summarized in Figure 4.20. The plots are arranged in a matrix, with each subplot corresponding to set coverage  $C(A, B)$ , i.e. the proportion of solutions of set  $B$  that are weakly dominated by  $A$ . In the plots, algorithm  $A$  is the column algorithm, e.g. a subplot in position (1, 2) shows the statistics for set coverage of random search by SPEA2. An algorithm's performance is better if it finds many non-dominated solutions and dominates many solutions found by the other algorithms, i.e., if it has larger  $C$  values in its column and smaller values in the row. The algorithms appear in the following order: random search, NSGA-II, SPEA2, and MOA with local search.

The plots suggest that MOLS finds better sets than other MOEAs on B1 and B2 but does not measure up to both on B3. With some improvements to constraint handling, MOLS performance is greatly improved on B4. MOLS performs slightly better than NSGA-II, since on average it dominates more solutions in the final NSGA-II's population than

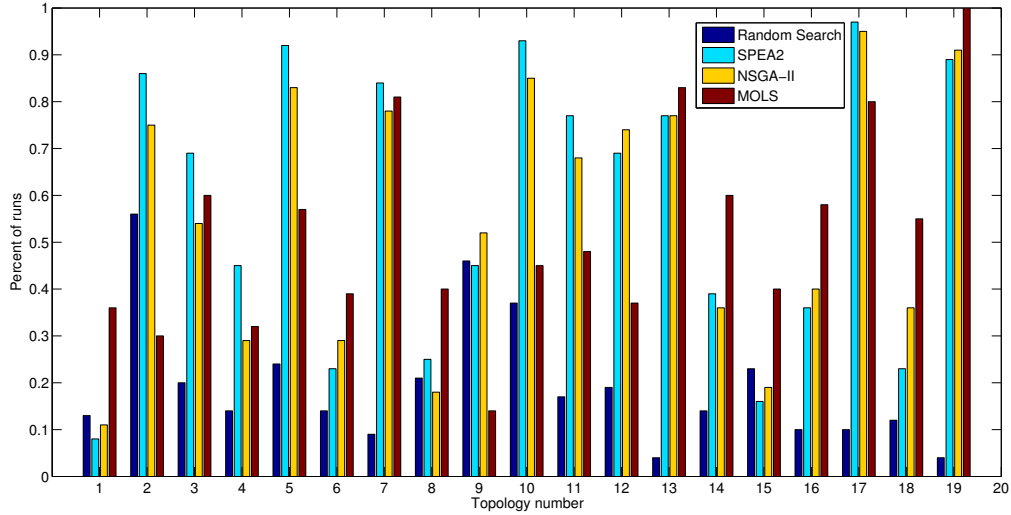


Figure 4.19: Performance on B4. Percent of runs in which each of the 19 Pareto-optimal topologies of a ten-bar truss was found. Each group of bars corresponds to a different topology. Each bar represents the result for a different algorithm. For the plots of topologies refer to Figure 4.9a.

vice versa. The mutual set coverage between MOLS and SPEA2 are comparable in most of the runs, suggesting that the two algorithms tend to exploit different areas of the objective space. On all four benchmarks, SPEA2 finds the most solutions that are not dominated by other algorithms' results.

Figure 4.21 summarizes the statistics of all metrics on the benchmarks. Each column of subplots represents a different problem; each row corresponds to a different metric ( $C$ ,  $GD$  and  $\sigma$ ), while the four box-plots within a subplot show the results for each algorithm. For all metrics, smaller values indicate better performance of the algorithm. B1 is the easiest problem on which all algorithms - except SPEA2 - reach zero set coverage in most of the runs. The fitness assignment of SPEA2 based on  $k$ th neighbor density estimation in the objective space fails to discriminate effectively against the sub-optimal regions in the search space. As a result, the algorithm keeps spending evaluations on exploration between the various regions rather than exploitation of the best-found candidates, preserving the sub-optimal solutions in the final archive. The  $GD$  is best for random search and MOLS, while the most uniform spread of solutions is obtained by the MOEAs. On B2, MOLS outperforms the other algorithms, showing better convergence to the global Pareto solutions (low  $C$  and  $GD$ ). However, the distribution of these solutions along the Pareto front is the worst among

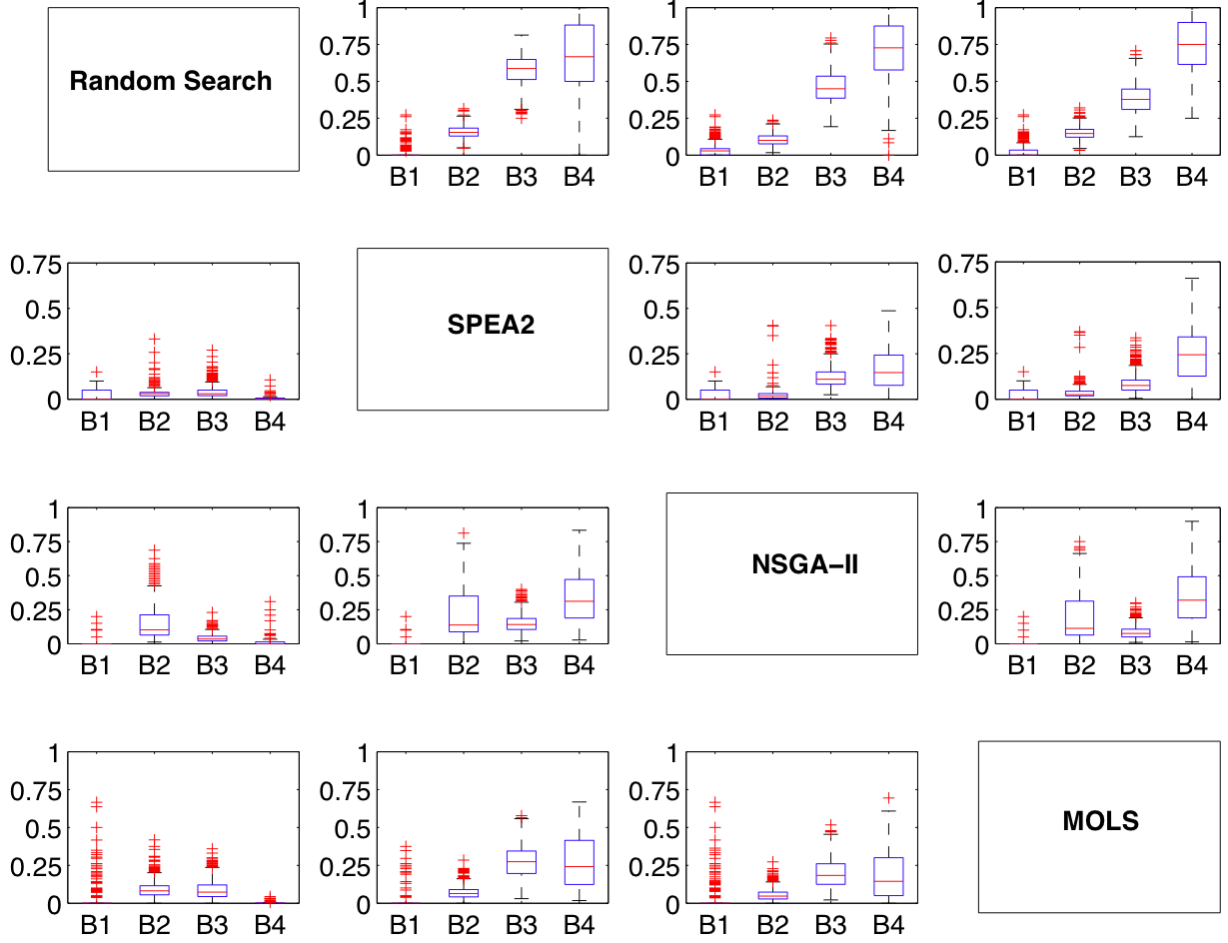


Figure 4.20: Comparison of algorithms' performance on the benchmarks  $B1$ - $B4$ . Each subplot shows set coverage  $C(A, B)$  where  $A$  is the column algorithm and  $B$  is the row algorithm. An algorithm's performance is better if it has larger  $C$  values in its column and smaller values in the row. Each of the boxes within the subplots corresponds to a different benchmark problem. The central line in the box shows the median of the metric, box edges show the 25% and 75% quantiles, and the whiskers extend to the extreme values. The red pluses describe the outliers.

the three algorithms. On B3, MOLS' strategy is not as effective, though it is much better than the random search, it loses to the MOEAs in all metrics. The changes in constraint handling implemented in B4 make MOLS more powerful such that it outperforms both MOEAs in set coverage and GD. The spread, however, remains high, indicating that MOLS better exploits certain areas of the Pareto front rather than explores along the front.

Among the algorithms, NSGA-II always finds the most diverse set of solutions as suggested by its low spread value in all benchmarks: this superior performance is credited to the algorithm's crowding-sort operator designed to explicitly increase the sparsity of solutions.

## 4.5 Summary

In this chapter, we have presented a number of simple problems that characterize the interactions between EM and mechanical properties of the structures and illustrate the types of fitness landscapes, encountered in the coupled optimization. The considered structural objectives are well behaved functions of the design variables; the EM objectives are more complex and non-convex. The resulting Pareto sets contain discontinuous islands of designs, spread over the entire search space. The constraints and periodicity of the EM functions might introduce champion solutions, that are hard to locate. The corresponding Pareto fronts are non-convex and include multiple regions with varying solution density.

Since very effective gradient-based methods exist in the field of structural optimization, we investigated how these methods can be combined with the population-based strategy of the EAs. We proposed a procedure that generates new candidate solutions by using the local search in each domain: in this way, the optimizers in each objective can be run separately and each domain can benefit from its most efficient techniques, algorithm parameters and solution representations.

We assessed the performance of the two most successful MOEAs and the proposed MOLS on the benchmark problems. The performance of the local search procedure is comparable and in some cases better than that of the MOEAs on simpler problems; on multivariate problems with stringent constraints, additional repair procedure is required to force the algorithm to explore feasible designs. Overall, MOLS finds a less uniform representation of the Pareto front, but unlike EAs it is better at locating and maintaining champion and extreme solutions.

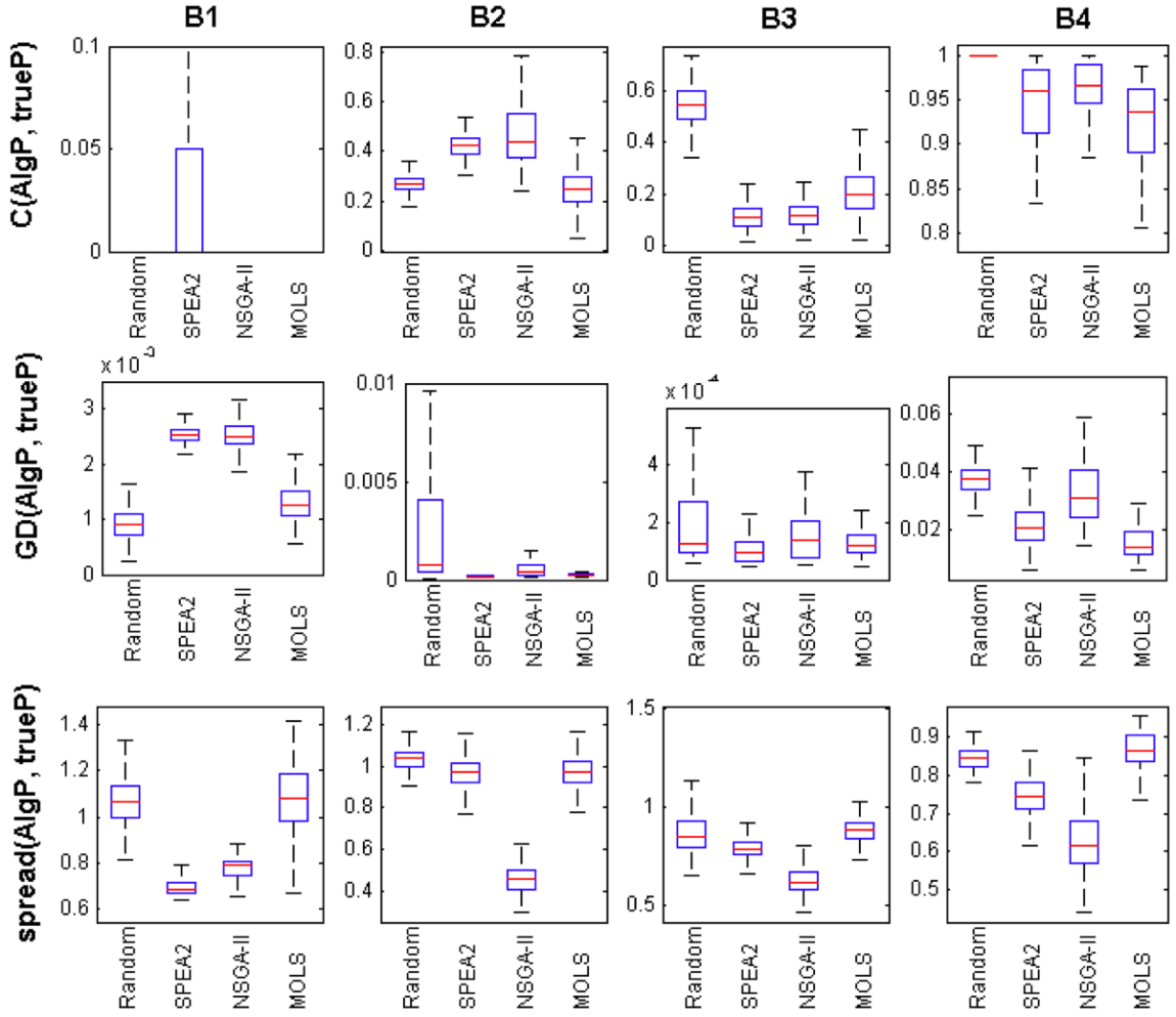


Figure 4.21: Comparison of algorithms' performance on the benchmarks  $B1$ - $B4$ . Each column of subplots represents a different problem; each row corresponds to a different metric ( $C$ ,  $\text{GD}$  and  $\text{spread } \sigma$ ), while the four box-plots within a subplot show the results for each algorithm. For all metrics, smaller values indicate better performance of the algorithm. The central line in the box shows the median of the metric, box edges show the 25% and 75% quantiles, and the whiskers extend to the extreme values.

## Chapter 5

# Multi-objective Optimization of a CubeSat

In this chapter, we apply the methods developed and tested in chapters 3 and 4 to the optimization of a CubeSat, a real-world problem in which mechanical and electromagnetic properties are critical to the mission success. CubeSat is a small satellite intended for scientific and educational purposes and has a prescribed shape, size and mass. CubeSats are deployed in space from a Poly-PicoSatellite Orbital Deployer (P-POD) which can carry up to three 1u CubeSats [52] and is sent to space on a rocket as a secondary payload (Figure 5.1b).

Our goal is to design a CubeSat antenna that utilizes the existing cubic structure to radiate. This allows for structure reuse and weight reduction, while freeing up mass for the payload. By modifying the CubeSat, we must make sure that it meets the mass and volume constraints and is still able to support loads during the launch which can reach up to  $20g$  along each cubical axis [71]. We want to understand the trade-offs between the structural integrity and electromagnetic performance that can be achieved with modifications of initial structure.

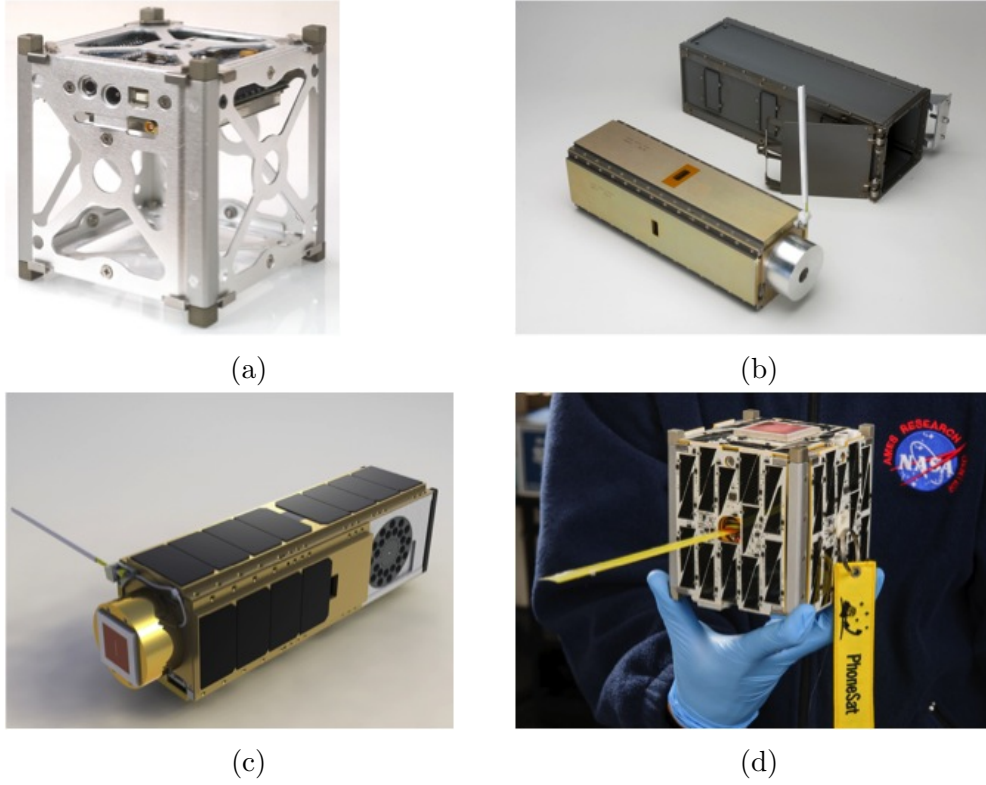


Figure 5.1: (a) CubeSat frame by Pumpkin Inc. [60] (b) Poly-PicoSatellite Orbital Deployer and a  $3u$  CubeSat [57] (c) O/OREOS Mission CubeSat [37] (d) PhoneSAT 2.5 [59].

## 5.1 Problem Definition

*Mechanical domain.* In the mechanical domain, we can determine several requirements for the CubeSat structure. The geometry of the CubeSat is prescribed: it should be  $100 \pm 0.1$  mm wide and  $113.5 \pm 0.1$  mm tall. Objects within the external mounting can extend up to 6.5 mm from the CubeSat surface. The total mass of a  $1u$  CubeSat - including the payload - should not exceed 1.33 kg [57]. For heavy payloads, it is desirable to reduce the mass of the bearing structure, and this requirement is included in our problem formulation as the volume constraint.

Main mechanical hazards can be encountered by the CubeSat during its transport to orbit: the structure is subjected to high acoustic pressure,  $g$ -force and vibrations. Since the size of the cube is small and its mechanical eigenfrequencies are much higher than the

specified acceptance levels, the dynamics of the experienced loads can be ignored and we can consider a static problem. The direction and magnitude of actual loads is a function of the launch vehicle: for our purposes, we shall assume that a 1u CubeSat inserted into P-POD experiences quasi-static forces along its vertical axis (Figure 5.2a).

In the mechanical domain, we seek a structure with the prescribed shape and volume that can support forces along its longest dimension, which can be formulated as a classical topology optimization problem and solved using mathematical programming methods.

The goal of topology optimization is to determine optimal material distribution within a specified volume for the known load and support conditions. The classical approach seeks to find an assignment of voids and solids in the reference domain so as to minimize the work (compliance) done by the external forces to deform the structure [47]. Bendsoe removed the discrete nature of the problem by expressing the objectives and constraints in terms of a continuous design variable, which can be interpreted as a density of material in a given point [5]. The Young's modulus of the material element  $E_i$  is interpolated between solid and void using a power law which penalizes the intermediate density points and steers the optimization procedure toward 0-1 designs. This penalization procedure is usually referred to as the Solid Isotropic Material with Penalization (SIMP) method [65]. In SIMP, at each iteration  $E_i$  is updated according to:

$$E_i(x_i) = E_{min} + x_i^p(E_0 - E_{min}), \quad x_i \in [0, 1]$$

where  $x_i$  is the normalized density of the  $i^{\text{th}}$  finite element and  $p$  is a penalization parameter greater than 1. The compliance problem in continuous formulation is

$$\begin{aligned} & \underset{\tilde{\mathbf{x}}}{\text{minimize}} && f = \mathbf{u}(\tilde{\mathbf{x}})^T \mathbf{F} \\ & \text{subject to} && V(\tilde{\mathbf{x}}) = \tilde{\mathbf{x}}^T \mathbf{v} - v \leq 0 \\ & && \mathbf{x} \in X, X = \{\mathbf{x} \in R^n : \mathbf{0} \leq \mathbf{x} \leq \mathbf{1}\} \end{aligned}$$

where  $\tilde{\mathbf{x}}$  is an  $n \times 1$  vector of filtered element densities that can vary between 0 and 1,  $\mathbf{u}$  is the vector of displacements in each degree of freedom,  $\mathbf{F}$  is the vector of loads, and  $v$  is the volume fraction.  $\mathbf{v}$  is a vector of elements' volumes. It is taken to be a unit vector when the reference domain is uniformly discretized.

The distinction between the filtered densities  $\tilde{\mathbf{x}}$  (referred to as physical densities) and regular densities  $\mathbf{x}$  should be emphasized. The use of a filter is an important regularization technique that mitigates numerical difficulties during optimization, such as checkerboard patterns, mesh dependency and local optima [5]. The filter has an effect of smoothing the densities over the neighboring elements with the neighborhood including all elements within the specified distance of the given element.

*Electromagnetic domain.* Most of the CubeSats include at least two antennas: an S-band is used as a primary space to ground communication link for telemetry and command transmission; a UHF beacon is included to broadcast satellite's position to a wide ham radio network, which allows to locate the CubeSat after its separation from the launch vehicle and track its position away from the ground station. On a number of CubeSat missions (e.g., OREOS , PhoneSAT shown in Figure 5.1c and 5.1d), a nadir-pointing S-band patch antenna has been successfully deployed: this directive antenna does not require any deployment mechanism but provides a relatively low beamwidth and might require attitude slew to increase the visibility time during the satellite's pass over the ground station. In the UHF band, monopole antennas (tape measure antennas) that can provide a wide coverage are commonly utilized. The placement of the antennas on the satellite must be considered to avoid shadowing by its metallic structure and to achieve the radiation performance conducive to mission goals.

As our test case, we consider a common situation in which one face of a CubeSAT is known to point toward Earth. The CubeSat antenna must produce a directional pattern with most of the power transmitted in the direction of the ground station. To match

the performance of a commercial patch antenna(AstroDev patch), it should achieve  $80^\circ$  Half Power Beamwidth (HPBW) and 5 dB gain in the boresight direction. The operating requirements are formalized as follows:

**Frequency:** 2215.5 MHz

**Input impedance :**  $50 \Omega$

**Gain pattern :** maximum possible gain toward ground and negligible radiation in other directions.

$$G(\theta, \phi) \begin{cases} \geq 3 & 0^\circ \leq \theta \leq 40^\circ, \quad 0^\circ \leq \phi \leq 360^\circ \\ = 0 & 90^\circ \leq \theta \leq 180^\circ, \quad 0^\circ \leq \phi \leq 360^\circ \end{cases}$$

The EM objective to be minimized is defined as the product of two components: (i) VSWR, which assures antenna's matching to 50 Ohms and (ii) error EG, which sums up the deviations of the gain values from the desired pattern. The definition of the *EG* follows the same principle as [50]. The function  $gain(i, j)$  is defined to allow for maximization of the gain in the boresight direction. There is no pressure for the algorithm to increase the gain beyond 8 dBi (equivalently a factor of 6). The second summation in the EG expression is added to penalize the design for radiation in the remaining directions.

$$gain_{ij} = gain \quad \text{at} \quad \theta = 5^\circ i, \quad \phi = 5^\circ j$$

$$gain(i, j) = \begin{cases} 0 & \text{if } gain_{ij} > 6 \\ 6 - gain_{ij} & \text{if } gain_{ij} \leq 6 \end{cases}$$

$$EG = \sum_{i=0}^{i=8} \sum_{j=0}^{j=72} gain(i, j) + \sum_{i=18}^{i=36} \sum_{j=0}^{j=72} |G(\theta_i, \phi_j)|$$

*Multi-objective optimization problem.* Combining the structural and EM SOPs, the MOP is defined as:

$$\begin{aligned}
& \underset{\tilde{\mathbf{x}}}{\text{minimize}} && f_1 = \mathbf{u}(\tilde{\mathbf{x}})^T \mathbf{F} \\
& && f_2 = \text{EG}(\tilde{\mathbf{x}}) \cdot VSWR(\tilde{\mathbf{x}}) \\
& \text{subject to} && V(\tilde{\mathbf{x}}) = \tilde{\mathbf{x}}^T \mathbf{v} - v \leq 0 \\
& && \mathbf{x} \in [0, 1]^n
\end{aligned}$$

## 5.2 Implementation

The MOP is solved using MOLS, which was presented in section 4.3.

In the mechanical domain, the 169-line MATLAB program by Kai Liu and Andres Tovar [47] serves as the local optimizer. The code takes a structure subdivided into finite cubic elements, location of supports and loading, and volume constraint as inputs and applies the regularized SIMP method to minimize the compliance of the structure.

The reference domain for optimization is a box subdivided into 12x12x14 cubic elements (Figure 5.2a). The faces of the cube and the areas extending between the stand-offs are modified during optimization. The rest volume is designated as passive areas that have fixed density throughout the optimization run. The inside volume is assigned zero density. CubeSat edges and stand-off legs in the corners have a fixed density of 1, contributing about 5% of the total volume.

The search space in the mechanical domain is delineated in Table 5.1: the structures are shown in the order of increasing compliance. Initial CubeSat frame has the lowest volume fraction and the highest compliance, while the full structure (hollow inside) with the lowest compliance and highest volume represents the other extreme of the structural universe.

In the EM domain, FEM structure is represented by a wire mesh (Figure 5.2b). To reduce the computational time, the thickness of the CubeSat’s walls is ignored and finite elements on the cubic faces are replaced by a planar wire mesh. Evaluation of the CubeSat’s

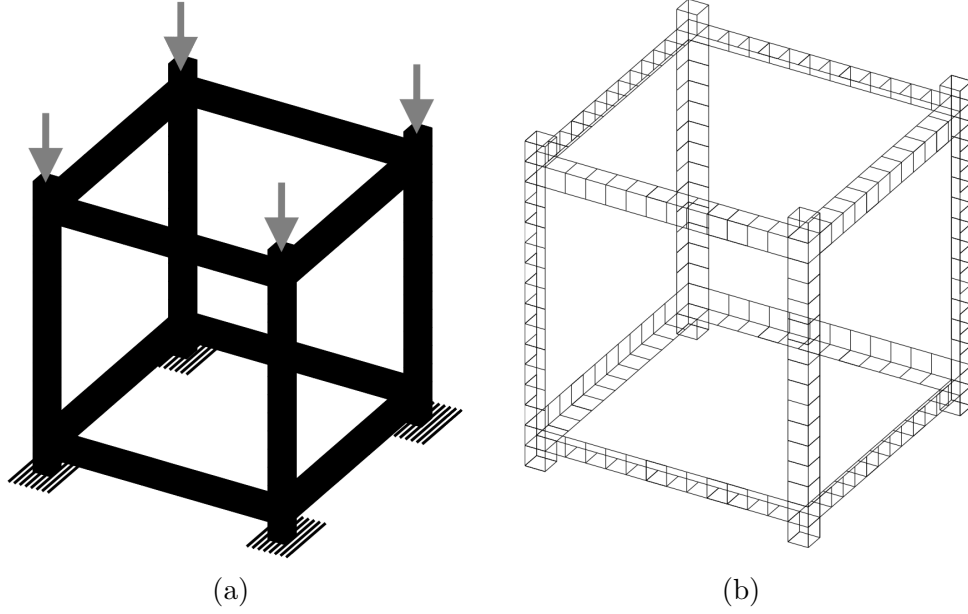


Figure 5.2: (a) Definition of the structural problem: 1u cube fixed at the bottom nodes bears a load of equal magnitude at the top corner nodes; (b) Wire mesh model of the structure used to evaluate EM fitness.

radiating properties is performed in NEC2C: after a feasible feed position is determined from TCM analysis of the structure, full EM simulation is run to determine the VSWR and gain of the antenna.

Local search operates on the same continuous vector of design variables  $\tilde{x}$  as the structural optimizer. Unlike the mechanical domain, intermediate densities do not bear any physical meaning that could be directly translated into the calculation of the EM objective: to evaluate EM fitness, the candidates must be interpreted as pure 0/1 designs where elements with densities above 0.5 are included as solids and elements with densities below 0.5 - as voids. However, preserving the density information is important to algorithm's performance : filtering the grayscale designs (rather than pure black and white designs) on density creates connected structures without floating elements, helps maintain diversity in the population and propagate the mechanical properties of the structure.

We include the intermediate densities in our design update scheme in the local search step. The TCM analysis estimates the power that could be radiated by the antenna if it

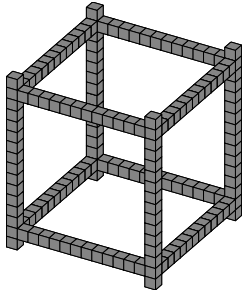
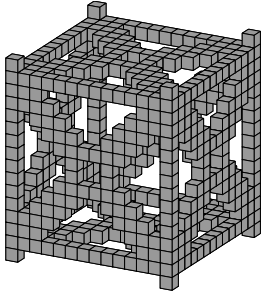
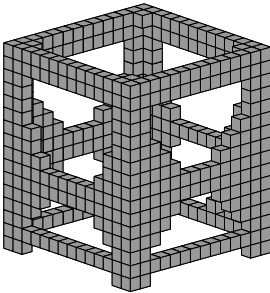
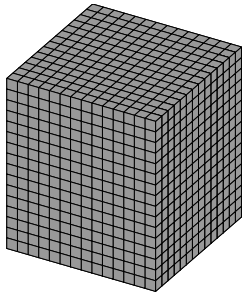
Structure	Compliance	Volume fraction
	$2.76 \times e + 4$	6.75%
	$1.75 \times e + 4$	21%
	$1.38 \times e + 4$	25%
	$1.18 \times e + 4$	50%

Table 5.1: CubeSat structures representative of the search space in the mechanical domain. The goal is to minimize compliance under the specified volume constraint. Compliance represents a generalized measure of the structural deformation under applied loads. Volume fraction is the percentage of the volume of the cube occupied by the solid material.

was excited at a certain wire segment. The segments with the lowest power are likely to be less significant for the antenna’s performance and can be penalized, while the segments with higher power or current should be preserved and enhanced. Following this intuition, we assign zero density to 5% of elements in the design that have the lowest power, the density of 1 to 5% top segments and the density of 0.5 with small Gaussian perturbation to the remaining segments. Though the relation between the density of material and current distribution is not as straightforward as in the mechanical domain, this heuristic rule proves to be a much better strategy than the random update.

The update rule defines the neighborhood of a candidate solution in the greedy hill climber (GHC) that performs local EM optimization. At each iteration, GHC evaluates the neighbors of the current solution and adopts a new candidate as the new solution only if the candidate has a better fitness.

### 5.3 Results

The size of the search space in this problem is  $2^{888}$ , including infeasible designs with disconnected elements and designs violating the volume constraint. The search space is extremely vast and is further increased by the continuous formulation of the problem. Since on average EM evaluation of a candidate takes three times longer than its mechanical evaluation, the runtime of the algorithm is determined by the number of calls to the EM simulator. After 25,000 evaluations, MOLS produced fourteen trade-off points that are shown in Figure 5.3. The trade-off curve is very steep and contains multiple designs with a good mechanical score. Non-dominated solutions with low compliance values are small variations of the same topology (Design 3 in Figure 5.4). The pre-dominance of this design suggests that structural fitness landscape has a large basin of attraction with the local minimum at  $1.359e + 4$ . Algorithm exploits the area in the vicinity of this design effectively, finding a spectrum of solutions of varying EM quality.

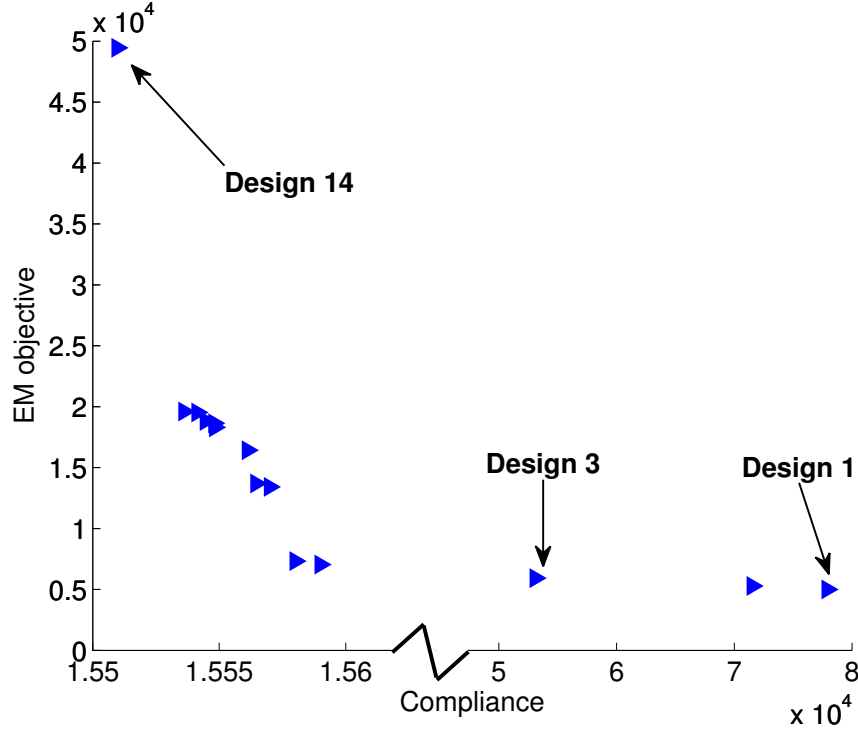


Figure 5.3: CubeSat Problem: Non-dominated solutions found by MOLS. Note the change of the scale on the  $x$ -axis. Designs 1, 3 and 14 are discussed in more detail in this section. Designs 14 and 1 are chosen as the designs on the boundaries of the Pareto front. Design 3 has the radiation pattern best matching the specifications.

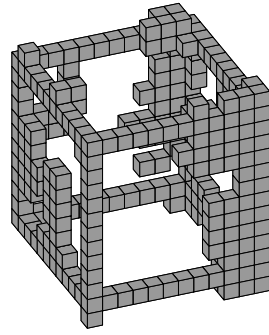
The EM problem proves to be much harder. The solutions not dominated in the EM objective show no resemblance to each other. Overall, they occupy much smaller volume than the mechanically optimized structures and include small extensions of the initial support frame (Figure 5.4a–5.4d). Similar positions of the feeds (on the CubeSat edges along  $y$ -direction, connecting the edge and a small metallic extension) point to the similar mechanism of the radiation by the structures. The smaller elements can be viewed as excitation probes used to couple power into the radiating eigenmodes of the initial CubeSat frame.

Fifty percent of the tradeoff designs have VSWRs below 3, meaning that at most 25% of the supplied power is reflected back to the transmitter without additional matching

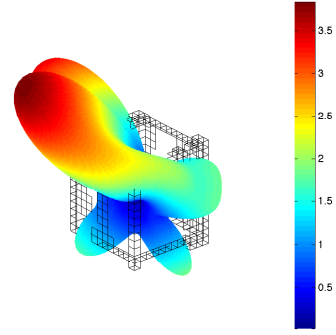
circuitry. The best solutions in the EM objective have a nearly perfect matching with VSWRs of 1.02 and 1.01. In terms of ER, Design 3 produces the best radiation pattern: it is able to match the gain specification in certain directions providing a beam with 5 dB gain at  $45^\circ$  from  $z$ -axis and HPBW  $80^\circ$ . However, the overall performance is not completely satisfactory for our goals. The total radiated power is split between two beams: the main beam does not point perpendicularly to the face of the cube, and significant amount of power is “lost” to the back-lobe with a 2 dB gain and HPBW of  $40^\circ$ .

The results suggest that it is hard to achieve a uni-directional high-gain antenna with this structure and given volume constraint. From TCM prospective, the difficulty of this task is caused by the multiple radiating modes that exist in the band of interest. Every edge of a CubeSAT is approximately half a wavelength long, resulting in multiple independent resonant paths for the current on the structure. As several orthogonal modes are excited at any feasible feed position, a multi-lobe pattern is produced. One feed is not sufficient to suppress the undesired modes. Changing the modes and their combinations by modifying the structure is possible, e.g., main radiation beams produced by the best EM designs (Figure 5.4b and 5.4d) is clearly a merge of several lobes. However, in this problem structural changes are restricted by the requirement to maintain the frame: since no parts of the cube’s frame can be removed, the resonant paths along the edges are preserved as well.

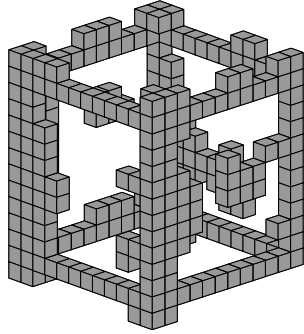
We know from experiments in Chapter 3 that cubic structure can produce a uni-directional radiation pattern, if only one face of the cube is chosen for optimization, while the other faces are preserved and act as a ground plane. However, in the current problem formulation such configuration violates the volume constraint. Thickness of the CubeSat’s walls is currently defined by the size of the mesh element ( $8 \times 8 \times 8 \text{ mm}^3$ ). If optimization is run on a finer meshed cubic structure, the algorithm will obtain a better set of non-dominated solutions with desired radiation characteristics but higher compliance values.



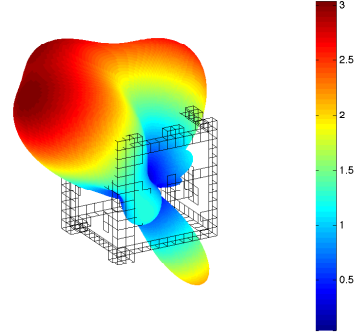
(a)



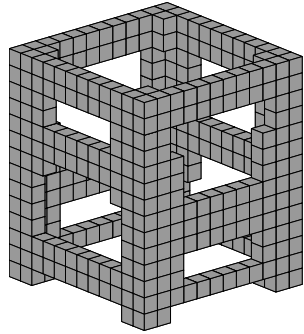
(b)



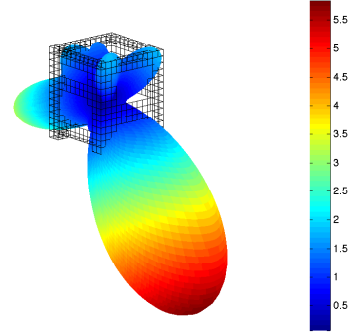
(c)



(d)



(e)



(f)

Figure 5.4: CubeSat antennas found by MOLS. Performance metrics of the designs are summarized in Table 5.2. (a) Design 1 with the best EM score; (b) Radiation pattern of Design 1; (c) Design 3 with the radiation pattern best matching the specifications; (d) Radiation pattern of Design 3; (e) Design 14, the best design in terms of compliance; (f) Radiation pattern of Design 14.

Table 5.2 summarizes VSWR, ER, and compliance values for the found non-dominated solutions in the order of increasing EM objective (left-to-right order in Figure 5.3). Some discrepancies between the compliance values in the plot and the table occur because compliance and volume fractions in the table have been recalculated for full designs, i.e., finite elements (FEs) with intermediate densities have been replaced with voids for FEs with  $\rho < 0.5$  or solids ( $\rho \geq 0.5$ ). The compliance score of the best designs is improved by increasing the density of the FEs, while the compliances of the worst structural designs are depressed.

Table 5.2: Performance scores of the structural CubeSat antennas found by MOLS.

Design	Volume fraction	Compliance	VSWR	ER
1	0.131	3.2e+12	1.02	4.9e+03
2	0.138	2.1e+12	1.01	5.2e+03
3	0.132	1.2e+05	1.35	4.4e+03
4	0.20	1.356e+04	1.3	5.5e+03
5	0.20	1.355e+04	1.3	5.6e+03
6	0.197	1.366e+04	2.5	5.3e+03
7	0.197	1.3671e+04	2.6	5.28e+03
8	0.198	1.366e+04	3.1	5.36e+03
9	0.198	1.365e+04	3.4	5.39e+03
10	0.199	1.361e+04	3.4	5.45e+03
11	0.199	1.363e+04	3.5	5.43e+03
12	0.198	1.364e+04	3.6	5.44e+03
13	0.199	1.3629e+04	3.6	5.42e+03
14	0.198	1.3601e+04	9.2	5.36e+03

## 5.4 Summary

In this chapter, we applied MOLS to a real-world coupled optimization problem, integration of an antenna on a CubeSat structure. In a high-dimensional search space, MOLS identified a number of tradeoff designs, that balance structural resistance to deformation and its performance as an S-band antenna. In the mechanical domain, a single locally optimal

topology was obtained: small variations on this structure contributed the majority of non-dominated solutions. In the EM domain, the goal of matching the antenna to  $50\ \Omega$  was met easily, unlike the radiation objective. The results suggest that the CubeSat structure is capable of generating multi-lobe patterns but is less suitable for uni- or omni-directional radiation in S-band under the given volume constraints.

# Chapter 6

## Conclusions and Future Work

### 6.1 Multi-objective optimization with Local Search

Computer-aided simulation tools have enabled engineers to design highly complex systems while taking into consideration constraints across multiple physical domains (e.g., mechanical, electronic, thermal, etc.). With the current focus on improving the simulation techniques, little attention has been paid to developing CAD tools for multi-physics optimization. While most CAD tools consider only a single phenomenon during optimization, MOLS algorithm presented in this work allows for effective integration of optimization techniques from two physical domains. It is straightforward to extend MOLS to an arbitrary number of domains and objectives assuming the domains are coupled statically, i.e. through design variables only.

MOLS performance is comparable to the performance of the leading MOEAs. Unlike MOEAs, MOLS does not rely on specialized fitness assignment in its search for Pareto trade-offs and determines the promising areas of the search space by considering the neighborhood of the solution in the design space rather than in the objective space. This mode of operation shifts the focus from the uniform coverage of Pareto objectives to attaining a more diverse set of engineering designs.

*Adaptation/self-adaptation of algorithmic parameters.* However, like MOEAs, MOLS' performance is dependent on the choice of parameters. While for smaller problems, it is possible to use preliminary tests or a meta-procedure to optimize the parameters before solving the MOP, the computational cost makes any preliminary testing for larger problems prohibitive. This issue can be alleviated by incorporating feedback from the search procedure and adapting the parameters during the run based on the search progress. One of the most important MOLS' parameters to adapt would be the number of steps taken by the local search in each domain: in our implementation, the number of evaluations at each iteration is reduced according to the power law. However, it should be beneficial to apply a self-adaptive strategy that would adjust the number of LS steps in proportion to the number of non-dominated candidates in each domain. Another parameter which governs the relation between the local and global search is the number of candidate solutions passed to the local search vs. the number of new solutions directly included in the population for dominance sorting.

*Parallelization. Distributed computation for MOO.* Parallelization and distribution of computation is necessary to alleviate the tremendous computational costs associated with solving large-scale multi-physics problems. MOLS lends itself well to parallelization since local search in each domain can be run independently. Further research should better inform the assignment of the computation to the parallel nodes and should clarify how the disproportion of LS in separate domains affects diversity in the population, what metrics best characterize the complexity of the landscape in each domain and how to determine the right balance between searches in landscapes of different complexity and non-linearity. We envision an adaptive computational process that measures the runtime of fitness evaluation in each domain and decides on the suitable distribution of computational resources. The state of the search could be also described by the rate of growth/change of the Pareto set, percentage of successful steps in LS, etc. For example, in the coupled problems in this work,

optimization in the mechanical domain is performed much faster and more effectively than EM optimization which is reflected in the number of LS evaluations taken to convergence and in the number of non-improving solutions tested by the LS algorithm in each domain. In this case, it would make sense to perform local optimization of more individuals in the EM domain, reducing LS in the mechanical domain.

Another step towards parallelizing MOLS should be desynchronization of the optimization procedure. In the current implementation, local searches are run sequentially and the number of individuals optimized in each domain is the same; though the number of LS steps is adjusted independently in each domain, there is no attempt at balancing out the computation between the domain optimizers. After local search step is complete, all current solutions are evaluated in both domains. Pareto sorting and triangularization is run on the current population at each iteration of the algorithm. In a distributed version, the non-dominated population can be updated asynchronously with the locally optimized candidates. Pareto sort and triangularization can be run as needed to generate new candidate solutions.

*Constraint handling.* In most of the coupled problems in this work, mechanical constraints became active for a small portion of all solutions in the search space. As a result, constraints did not have to be considered during local optimization in the EM domain. This approach allows for full decoupling of the domains but degrades algorithm’s performance in problems with more complex constraint functions, in which case such decomposition may cause the algorithm to waste valuable resources on local search in the infeasible area. Degradation of MOLS’ performance on *B3* (compared to MOEAs) highlighted the need for better constraint handling across the domains. On *B4*, for example, in which the requirement of statical determinacy of the structure made a large portion of the search space infeasible, a special repair procedure had to be introduced to improve MOLS’ performance. With the goal of decoupling the optimization in various domains as much as possible, better

understanding and characterization of domain interactions on the constraint boundaries is required.

Some classical and evolutionary approaches to constraint handling could be applied in MOLS: explicitly solving the feasibility problem for each design before running optimization is a good strategy (implemented in B4) though it precludes full decoupling of the domains; design representation can be used to exclude infeasible designs from consideration, for example by prohibiting certain changes or imposing suitable box constraints on the design variables in the LS step; reformulating the problem and including the constraint as an additional objective does not prevent the algorithm from exploration of the infeasible parts of the search space.

*Incorporating surface response models.* As computational time is the primary roadblock in solving any multi-physics MOP, incorporation of surface models is yet another way to alleviate the costs and preserve the most information about the visited regions of the search space. Evaluated designs and their fitness scores can be stored in memory, and as the search proceeds and more designs are evaluated in each objective, the models can provide more accurate predictions about the most promising search directions. Currently, the algorithm stores the locally optimal designs and their EM scores to avoid reevaluating duplicates.

## 6.2 Local search in the EM domain

In this work, we have assumed that effective local search (LS) algorithms exist in each of the considered domains. However, this assumption has proved too strong in multi-variate SOPs in the EM domain. Due to the computational cost of EM evaluations, gradient-based techniques are not always feasible. There is a need for robust LS algorithms that can consistently lead to improvement in the EM objective by exploring the nearest neighborhood of the current candidate solution. In the tests that we performed on electrically small plates, removing the material around the segments with the highest currents created designs with

a more pronounced radiating mode. A way of fine-tuning the designs (that we investigated briefly) was the gradual change of the trace thickness (for planar antennas) or of wire radii (wire antennas) based on the eigencurrents and power values. In the CubeSAT problem we implemented an update rule based on TCM that removed a fraction of the segments with the smallest currents, while assigned more weight to the segments with higher currents. Though these procedures lead to improvement in the fitness function more often than a random step, further research into heuristic rules and neighborhood definitions is required to make LS more effective.

This also ties into the application of TCM to feed placement. Currently, the procedure identifies the position of the coaxial feed for the segments present in the structure. It is desirable to derive information from TCM that would also suggest ways of coupling energy through capacitive or inductive elements. Since in our approach we consider these elements as part of the structure (rather than separate probes), we could develop TCM-based rules for adding material to the current antenna to ensure better matching, radiation efficiency, etc. Some researchers have suggested using the near-fields of the radiating modes to determine the promising feed areas. Incorporating this procedure into the automated optimization algorithm is another way of extending the present research.

## 6.3 TCM

*EM optimization based on TCM.* We have conducted extensive study of the objectives defined in TCM terms and have shown that power estimates from TCM can effectively guide EM optimization toward designs with better radiating properties. TCM uses a single objective to help the algorithm identify the most promising areas of the design space. It further improves the search by suggesting the feasible feed positions. However, our current approach seeks to improve VSWR and the radiation efficiency of an antenna and cannot score designs in terms of polarization or radiation pattern. The procedure also

does not utilize the full power of the TCM decomposition, as the various eigenmodes are aggregated into a single fitness score. One obvious continuation of this work is to derive the objectives for radiation patterns and polarization based on TCM and test if they give any computational advantage or allow for more effective search than the full EM optimization. Another research direction could seek to combine TCM and primary EM objectives for single-objective optimization. TCM computation could guide the exploration in the initial stages of the search, while full EM simulation could be used to exploit the promising solution areas.

*Application to dielectric bodies.* Another area we have not considered in this work is application of TCM to the optimization of dielectric bodies, e.g. microstrip antennas. In the presence of dielectric losses, the eigencurrents and their corresponding patterns are no longer  $R$ -orthogonal to each other. The power component of each eigenmode includes the radiated as well as the dissipated power, and distinguishing between these components is essential to determining the radiation efficiency of an antenna.

*MIMO applications.* TCM is promising for automated design of MIMO antennas, since it describes antenna performance in terms of orthogonal current modes. MIMO applications are plentiful and one of the most challenging is associated with antenna design for small sensor nodes and mobile terminals. For the frequency-agnostic operation, instead of using a wide-band antenna and applying a filter to tune to the desired frequency (WiFi, GSM, 3G, GPS, etc.), we could envision an antenna with multiple feeds (capacitive or inductive coupling elements) that would sense signals at different bands. The objective is then to minimize the coupling between the radiating modes at various power supplies while maintaining acceptable matching and radiation properties. When formulated as MOP, it could provide valuable insight into the trade-offs between the performance in the bands of interest.

Our TCM-based placement algorithm could be extended for solving this problem. Real

power associated with each of the modes at the given feed can be used as a measure of inter-mode coupling. Within a discretized structure, the segments that have the largest disparity between the powers of the radiating modes would suggest the lowest coupling.

## 6.4 Conclusion

This research investigated stochastic optimization algorithms that can be used in a multi-physics design automation tool. It is the first work to develop and extensively test techniques for coupled optimization of integrated electromagnetic and mechanical systems. We took an unconventional design approach, in which an arbitrary metallic structure or its components can be modified to act as efficient radiators. Leaning on the theory of characteristic modes, we modified the search in the EM domain for easy integration with the structural optimization methods. We derived TCM-based fitness objectives to predict the potential of the structure to radiate and guide the exploration of the search space.

The algorithms presented in this work allow for effective integration of antennas with the mechanical structure and enable structure reuse, as validated on a number of small benchmark problems and real-world applications. Setting up and solving a multi-physics problem is a time consuming and resource intensive process that requires expertise in all domains under consideration. Relying on the efficient domain-specific methods relaxes this requirement and allows for straightforward set-up of the optimization procedure across multiple physical disciplines. While this research has focused on coupled optimization across electromagnetic and mechanical domains, the presented multi-objective algorithm with local search can be applied more generally: effectively combining domain-specific methods and representations, MOLS can be extended to solve a multi-physics optimization problem with a large number of disciplines and objectives.

# Bibliography

- [1] Jacob J. Adams. *Characteristic Modes for Impedance Matching and Broadbanding of Electrically Small Antennas*. PhD thesis, University of Illinois at Urbana-Champaign, 2011. 2.1
- [2] ANSYS, Inc. Multiphysics solutions features, 2014. URL <http://www.ansys.com/Products/Simulation+Technology/Multiphysics/Features>. Accessed 11-November-2014. 1.2.4
- [3] Brian A. Austin and Kevin P. Murray. The application of characteristic-mode techniques to vehicle-mounted NVIS antennas. *IEEE Antennas and Propagation Magazine*, 40(1):7–21, 1998. 2.1
- [4] Martin P. Bendsøe, Aharon Ben-Tal, and Jochem Zowe. Optimization Methods for Truss Geometry and Topology Design. *Structural optimization*, 7(3):141–159, 1994. 4.1, 4.2.5
- [5] Martin Philip Bendsøe. Optimal Shape Design as a Material Distribution Problem. *Structural Optimization*, 1(4):193–202, 1989. 1.2.2, 4.1, 5.1
- [6] Martin Philip Bendsoe. *Topology Optimization: theory, methods and applications*. Springer, 2003. 1.2.2, 4.1
- [7] Stephen Boyd and Lieven Vandenbergh. *Convex Optimization*. Cambridge university press, 2009. 2.3.1
- [8] G.J. Burke and A.J. Poggio. Numerical Electromagnetics Code (NEC) Method of Moments. Part iii: User’s guide. *NOSC technical document*, 116, 1981. 2.1, 4.3.1
- [9] Heyward Burnette. New Antennas Conform to Air Vehicles, Not Status Quo, 2010. URL <http://www.wpafb.af.mil/news/story.asp?id=123226369>. Accessed 11-November-2014. 1.2.1
- [10] Marta Cabedo Fabres. Systematic design of antennas using the theory of characteristic modes. 2008. 2.1, 3.1, 3.2.2
- [11] Paul J. Callus. Conformal load-bearing antenna structure for Australian Defence Force aircraft. 2007. 1.2.1
- [12] Olcay Ersel Canyurt and Prabhat Hajela. Cellular Genetic Algorithm technique for the Multicriterion Design Optimization. *Structural and Multidisciplinary Optimization*, 40(1-6):201–214, 2010. 4.2.3
- [13] Y. Cengiz and H. Tokat. Linear antenna array design with use of genetic, memetic

- and tabu search optimization algorithms. *Progress In Electromagnetics Research*, 1: 63–72, 2008. ISSN 1937-8718. 2.2, 4.1
- [14] Richard L. Chaney, Douglas R. Hackler, Dale G. Wilson, and Brian N. Meek. Advanced conformal load-bearing antenna structures. 1.2.1
  - [15] Yikai Chen and C. Wang. Electrically small UAV antenna design using characteristic modes. 2014. 2.1
  - [16] Yikai Chen and Chao-Fu Wang. Shipboard NVIS radiation system design using the theory of characteristic modes. In *2014 IEEE Antennas and Propagation Society International Symposium (APSURSI)*, pages 852–853. IEEE, 2014. 1.2.1, 2.1
  - [17] P.J.B. Clarricoats, Z. Hai, R.C. Brown, G.T. Poulton, and G.E. Crone. A Reconfigurable Mesh Reflector Antenna. In *Sixth International Conference on Antennas and Propagation (Conf. Publ. No. 301), 1989. ICAP 89.*, pages 112–116. IET, 1989. 1.2.1
  - [18] C.A. Coello and Alan D. Christiansen. Multiobjective Optimization of Trusses using Genetic Algorithms. *Computers & Structures*, 75(6):647–660, 2000. 4.2.3
  - [19] COMSOL, Inc. Mems module, 2014. URL <http://www.comsol.com/support/releasenotes/4.2a/mems/>. Accessed 11-November-2014. 1.2.4
  - [20] Jerome J. Connor and Susan Faraji. *Fundamentals of Structural Engineering*. Springer, 2012. 4.2.1
  - [21] Kalyanmoy Deb. *Multi-objective Optimization using Evolutionary Algorithms*, volume 16. John Wiley & Sons, 2001. 2.3.1, 2.3.2, 2.3.4, 2.3.5, 4.2.5
  - [22] Kalyanmoy Deb and Surendra Gulati. Design of Truss-structures for Minimum Weight using Genetic Algorithms. *Finite elements in analysis and design*, 37(5):447–465, 2001. 4.2.3, 4.2.5, 4.4.1
  - [23] Kalyanmoy Deb, Amrit Pratap, Sameer Agarwal, and TAMT Meyarivan. A fast and elitist multiobjective genetic algorithm: NSGA-ii. *IEEE Transactions on Evolutionary Computation*, 6(2):182–197, 2002. 2.3.2
  - [24] Baoyan Duan and Meng Wang. Multidisciplinary Optimization of Microwave antennas. 2013. 1.2.1
  - [25] A.E. Eiben and J.E. Smith. *Introduction to evolutionary computing*. Springer Verlag, 2003. 2.2
  - [26] Hans A. Eschenauer and Niels Olhoff. Topology Optimization of Continuum Structures: A Review\*. *Applied Mechanics Reviews*, 54(4):331–390, 2001. 1.2.2
  - [27] Nikolaus Fichtner, Uwe Siart, and Peter Russer. Antenna bandwidth Optimization using Transmission Line Matrix Modeling and Genetic Algorithms. In *International Symposium on Signals, Systems and Electronics, 2007. ISSSE'07.*, pages 79–82. IEEE, 2007. 1.2.3
  - [28] Robert John Garbacz and R. Turpin. A generalized expansion for radiated and scattered fields. *IEEE Transactions on Antennas and Propagation*, 19(3):348–358, 1971. 2.1

- [29] Yacov Y. Haimes, L.S. Ladson, and David A. Wismer. Bicriterion formulation of problems of integrated system identification and system optimization, 1971. 2.3.1
- [30] Prabhat Hajela and E. Lee. Genetic Algorithms in truss topological optimization. *International Journal of Solids and Structures*, 32(22):3341–3357, 1995. 4.2.3
- [31] Ken Harada, Jun Sakuma, and Shigenobu Kobayashi. Local Search for Multiobjective Function Optimization: Pareto Descent Method. In *Proceedings of the 8th annual conference on Genetic and evolutionary computation*, pages 659–666. ACM, 2006. 2.3.3
- [32] R. Harrington and J. Mautz. Theory of characteristic modes for conducting bodies. *IEEE Transactions on Antennas and Propagation*, 19(5):622–628, 1971. 2.1, 3.1
- [33] Roger F. Harrington, J.R. Mautz, and Yu Chang. Characteristic modes for dielectric and magnetic bodies. *IEEE Transactions on Antennas and Propagation*, 20(2):194–198, 1972. 2.1
- [34] Hisao Ishibuchi and Tadahiko Murata. A Multi-objective Genetic Local Search Algorithm and its Application to Flowshop Scheduling. *IEEE Transactions on Systems, Man, and Cybernetics, Part C: Applications and Reviews*, 28(3):392–403, 1998. 2.3.3
- [35] Shahrzad Jalali Mazlouman, Alireza Mahanfar, Carlo Menon, and Rodney G. Vaughan. Reconfigurable axial-mode helix antennas using shape memory alloys. *IEEE Transactions on Antennas and Propagation*, 59(4):1070–1077, 2011. 1.2.1
- [36] Andrzej Jaszkiewicz. On the Performance of Multiple-objective Genetic Local Search on the 0/1 Knapsack problem-a Comparative Experiment. *IEEE Transactions on Evolutionary Computation*, 6(4):402–412, 2002. 2.3.3
- [37] Karen Jenvey. Small satellite missions, 2011. URL [http://www.nasa.gov/mission\\_pages/smallsats/ooreos/main/](http://www.nasa.gov/mission_pages/smallsats/ooreos/main/). accessed 11-November-2014. 5.1
- [38] J. Michael Johnson and Yahya Rahmat-Samii. Genetic Algorithms and Method of moments (GA/MOM) for the Design of Integrated Antennas. *IEEE Transactions on Antennas and Propagation*, 47(10):1606–1614, 1999. 1.2.3, 3.3.5, 4.1
- [39] D. Karaboga, K. Guney, and A. Akdagli. Antenna array pattern nulling by controlling both amplitude and phase using modified touring ant colony Optimization Algorithm. *International journal of electronics*, 91(4):241–251, 2004. ISSN 0020-7217. 2.2, 4.1
- [40] David E. Keyes, Lois C. McInnes, Carol Woodward, William Gropp, Eric Myra, Michael Pernice, John Bell, Jed Brown, Alain Clo, Jeffrey Connors, et al. Multiphysics simulations: Challenges and opportunities. *International Journal of High Performance Computing Applications*, 27(1):4–83, 2013. 1.2.4
- [41] M.M. Khodier and C.G. Christodoulou. Linear array geometry synthesis with minimum sidelobe level and null control using particle swarm Optimization. *IEEE Transactions on Antennas and Propagation*, 53(8):2674–2679, 2005. ISSN 0018-926X. 2.2, 4.1
- [42] V. Lakafosis, X. Yi, T. Le, E. Gebara, Y. Wang, and M.M. Tentzeris. Wireless sensing with smart skins. In *2011 IEEE Sensors*, pages 623–626. IEEE, 2011. 1.2.1
- [43] Adriana Lara, Gustavo Sanchez, Carlos A. Coello Coello, and Oliver Schutze. HCS:

- A New Local Search Strategy for Memetic Multi-objective Evolutionary Algorithms. *IEEE Transactions on Evolutionary Computation*, 14(1):112–132, 2010. 2.3.3
- [44] Hui Li, Yi Tan, Buon Kiong Lau, Zhinong Ying, and Sailing He. Characteristic mode based tradeoff analysis of antenna-chassis interactions for multiple antenna terminals. *IEEE Transactions on Antennas and Propagation*, 60(2):490–502, 2012. 2.1
  - [45] Hui Li, Zachary Miers, and Buon Kiong Lau. Generating multiple characteristic modes below 1 GHz in small terminals for MIMO antenna design. In *IEEE International Symposium on Antennas and Propagation*, 2013. 2.1
  - [46] J.S. Liu and L. Hollaway. Integrated Structure-electromagnetic Optimization of Large Reflector Antenna Systems. *Structural Optimization*, 16(1):29–36, 1998. 1.2.1
  - [47] Kai Liu and Andrés Tovar. An efficient 3D topology Optimization code written in Matlab. 5.1, 5.2
  - [48] Leonardo Lizzi, Federico Viani, Renzo Azaro, and Andrea Massa. A PSO-driven spline-based shaping approach for ultrawideband (UWB) antenna synthesis. *IEEE Transactions on Antennas and Propagation*, 56(8):2613–2621, 2008. 1.2.3
  - [49] J. Lohn, G. Hornby, and D. Linden. Tools for Automated Antenna Design and Optimization. *Journal of Aerospace Computing, Information, and Communication*, 4(5):853–864, 2007. 2.2, 4.1
  - [50] Jason D. Lohn, Derek S. Linden, Gregory S. Hornby, William F. Kraus, and Adaan Rodriguez-Arroyo. Evolutionary design of an X-band antenna for NASA’s space technology 5 mission. In *Evolvable Hardware, NASA/DoD Conference on*, pages 155–155. IEEE Computer Society, 2003. 5.1
  - [51] A. Mahanfar, C. Menon, and R.G. Vaughan. Smart antennas using electro-active polymers for deformable parasitic elements. *Electronics Letters*, 44(19):1113–1114, 2008. 1.2.1
  - [52] Erin Mahoney. Human exploration and operations: CubeSat launch initiative, 2014. URL [http://www.nasa.gov/directorates/heo/home/CubeSats\\_initiative.html#.VGJnxIe1zys](http://www.nasa.gov/directorates/heo/home/CubeSats_initiative.html#.VGJnxIe1zys). Accessed 11-November-2014. 5
  - [53] J.C.G. Matthews and G. Pettitt. Development of flexible, wearable antennas. In *3rd European Conference on Antennas and Propagation, 2009. EuCAP 2009.*, pages 273–277. IEEE, 2009. 1.2.1
  - [54] Zachary Miers, Hui Li, and Buon Kiong Lau. Design of bandwidth enhanced and multiband MIMO antennas using characteristic modes. 2014. 2.1
  - [55] Kaisa Miettinen. *Nonlinear multiobjective Optimization*, volume 12. Springer, 1999. 2.3.1
  - [56] A.D. Monk and P.J.B. Clarricoats. Reconfigurable reflector antenna producing pattern nulls. *IEE Proceedings-Microwaves, Antennas and Propagation*, 142(2):121–128, 1995. 1.2.1
  - [57] I. Nason, M. Creedon, and J. Puig-Suari. CubeSat design specifications document. *Revision V*, pages 1–6, 2001. 5.1, 5.1

- [58] E.H. Newman. Small antenna location synthesis using characteristic modes. *IEEE Transactions on Antennas and Propagation*, 27:530, 1979. 2.1
- [59] PhoneSat HAM community. Phonesat: Nasa ames' smartphone nanosatellite, 2014. URL <http://www.phonesat.org/>. accessed 11-November-2014. 5.1
- [60] Pumpkin Inc. Begin your CubeSat Mission with the CubeSat kit-TM, 2013. URL <http://www.cubesatkit.com/>. Accessed 11-November-2014. 5.1
- [61] Hossein Rahami. Matrix structural analysis, 2010. URL <http://www.mathworks.com/matlabcentral/fileexchange/27012-matrix-structural-analysis>. accessed 26-October-2014. 4.3.1
- [62] Jussi Rahola, Danie Ludick, and Peter Futter. Characteristic modes and antenna bandwidth. In *2014 IEEE Antennas and Propagation Society International Symposium (APSURSI)*, pages 1415–1416. IEEE, 2014. 2.1
- [63] Bryan Dennis Raines. *Systematic Design of Multiple Antenna Systems Using Characteristic Modes*. PhD thesis, Ohio State University, 2011. 2.1, 3.2
- [64] N. Rais, Ping Jack Soh, Malek Fareq, Ahmad Sahadah, Mohd Hashim Nur Baya, and P.S. Hall. A review of wearable antenna. 2009. 1.2.1
- [65] G.I.N. Rozvany, M. Zhou, and T. Birker. Generalized shape Optimization without Homogenization. *Structural Optimization*, 4(3-4):250–252, 1992. 5.1
- [66] Abraham Rubinstein, Farhad Rachidi, and Marcos Rubinstein. On wire-grid representation of solid metallic surfaces. *IEEE Transactions on Electromagnetic Compatibility*, 47(1):192–195, 2005. 3.2.2
- [67] John Ruze. Antenna Tolerance Theory – a Review. In *IEEE Proceedings*, volume 54, pages 633–642, 1966. 1.2.1
- [68] S. Sankaralingam and Bhaskar Gupta. Development of textile antennas for body wearable applications and investigations on their performance under bent conditions. *Progress In Electromagnetics Research*, 22:53–71, 2010. 1.2.1
- [69] Karthik Sindhya, Kalyanmoy Deb, and Kaisa Miettinen. A Local Search based Evolutionary Multi-objective Optimization Approach for Fast and Accurate Convergence. In *Parallel Problem Solving from Nature-PPSN X*, pages 815–824. Springer, 2008. 2.3.3
- [70] Karthik Sindhya, Ankur Sinha, Kalyanmoy Deb, and Kaisa Miettinen. Local Search based Evolutionary multi-objective Optimization Algorithm for constrained and unconstrained problems. In *IEEE Congress on Evolutionary Computation, 2009. CEC'09.*, pages 2919–2926. IEEE, 2009. 2.3.3
- [71] Spaceflight, Inc. Secondary payload user's guide, March 2013. URL <http://spaceflightservices.com/wp-content/uploads/2013/05/SF-2100-PUG-00001-Spaceflight-SPUG-Rev-D.pdf>. Accessed 11-November-2014. 5
- [72] Charles Spearman. The proof and measurement of association between two things. *The American journal of psychology*, 15(1):72–101, 1904. 3.3.2

- [73] T. Stützle and H. Hoos. *Stochastic Local Search: Foundations and Applications*. Morgan Kaufmann, 2005. 2.2
- [74] K. Svanberg. On the Convexity and Concavity of Compliances. *Structural and Multidisciplinary Optimization*, 7(1):42–46, 1994. 4.1, 4.2.5
- [75] The Mathworks Inc. Constrained Nonlinear Optimization Algorithms, 2014. URL <http://www.mathworks.com/help/optim/ug/constrained-nonlinear-optimization-algorithms.html>. Accessed 26-October-2014. 4.3.1
- [76] Santosh Tiwari, Georges Fadel, Patrick Koch, and Kalyanmoy Deb. Performance Assessment of the Hybrid Archive-based Micro Genetic Algorithm (AMGA) on the CEC09 Test Problems. In *IEEE Congress on Evolutionary Computation, 2009. CEC'09.*, pages 1935–1942. IEEE, 2009. 2.3.3
- [77] X.L. Travassos, D.A.G. Vieira, and A.C. Lisboa. Antenna Optimization using Multiobjective Algorithms. *ISRN Communications and Networking*, 2012:4, 2012. 1.2.3
- [78] D. Veldhuizen and G. Lamont. Multiobjective evolutionary algorithms: Analyzing the state-of-the-art. *Evolutionary computation*, 8(2):125–147, 2000. 2.3.5
- [79] C.S. Wang and B.Y. Duan. Electromechanical coupling model of electronic equipment and its applications. In *2010 International Conference on Mechatronics and Automation (ICMA)*, pages 997–1003. IEEE, 2010. 1.2.1
- [80] Y. Mike Xie and Grant P. Steven. *Basic Evolutionary Structural Optimization*. Springer, 1997. 1.2.2
- [81] Chisang You, Daniela Staiculescu, Lara Martin, and Manos M. Tentzeris. A novel hybrid electrical/mechanical Optimization technique using time-domain modeling, finite element method and statistical tools for co-design and Optimization of RF-integrated mechanical structures. *International Journal of Numerical Modelling: Electronic Networks, Devices and Fields*, 21(1-2):91–101, 2008. 1.2.1
- [82] Qingfu Zhang and Hui Li. MOEA/D: A Multiobjective Evolutionary Algorithm based on Decomposition. *IEEE Transactions on Evolutionary Computation*, 11(6):712–731, 2007. 2.3.3
- [83] Eckart Zitzler. *Evolutionary Algorithms for multiobjective Optimization: Methods and applications*, volume 63. Shaker Ithaca, 1999. 2.3.5
- [84] Eckart Zitzler, Marco Laumanns, Lothar Thiele, Eckart Zitzler, Eckart Zitzler, Lothar Thiele, and Lothar Thiele. SPEA2: Improving the strength Pareto evolutionary Algorithm, 2001. 2.3.2